Electromechanical Large Scale Computational Models of the Ventricular Myocardium

PhD Thesis by
Ruth Arís Sánchez

Thesis Director:
Mariano Vázquez

Cover Design:
Guillermo Marín

Submitted to
Universitat Politècnica de Catalunya

Barcelona, September 2014

Abstract

A cardiac computational model is a relevant tool that can give biomedical researchers an additional source of information to understand how the heart works. Numerical models can help to interpret experimental data and provide information about cardiac mechanisms that can not be determined accurately by classical clinical devices. In this thesis, High Performance Computing (HPC) techniques are used to build a cardiac computational tool, which is capable of running in parallel in thousands of processors, allowing high fidelity simulations on fine meshes. To simulate the pumping heart, an explicit coupling scheme between the three-dimensional electrophysiological equations and the solid mechanics formulation is used, solving the governing equations with finite element methods. Also, data assimilation techniques are implemented for the effective estimation of some relevant electrophysiological parameters, which is a crucial step towards the patient-sensitive cardiac model. The data assimilation techniques are assessed on synthetic data generated by the model. Finally, the computational code is applied to simulate real physical problems. The electromechanical propagation in a rabbit geometry is studied to test the sensitivity of the framework to input variations. Particularly, the computational tool is used to evaluate the influence of the fiber field in the contraction of the tissue.

To develop a cardiac simulation useful for clinical purposes, the integrative model requires combining computational mechanics and image processing techniques via data assimilation methods. Coupled with the most advanced image processing analysis, the framework can be the base of theoretical studies into the mechanisms of cardiac pathologies. It can help surgery planning and cardiac modeling, such as the prediction of the impact of pharmacological compounds on the heart's rhythm or to improve the knowledge of drug study, giving medical researchers additional hints to understand the heart. This realization is only possible in a multidisciplinary team, where specialized groups join forces in their respective disciplines: cardiologists, image researchers,

bioengineers and computational scientists. The present cardiac computational model is one further step towards the creation of a virtual lab.

Resum

Els models computacionals del cor són una eina important que pot donar als investigadors biomèdics una font addicional d'informació per entendre el funcionament del miocardi. Els models numèrics poden ajudar a interpretar dades experimentals i proporcionar informació complementària sobre mecanismes cardíacs que no poden ser determinats amb precisió mitjançant dispositius clínics clàssics. En aquesta tesi, s'apliquen tècniques de computació a gran escala per construir una eina computacional capaç d'executar-se en paral·lel en milers de processadors, permetent simulacions d'alta fidelitat en malles fines. Per simular el bombeig del cor, s'utilitza un esquema d'acoblament explícit entre les equacions electrofisiològiques en tres dimensions i la formulació en mecànica de sòlids. Per trobar la solució numèrica, s'utilitza el mètode d'elements finits. A més, s'implementen tècniques en assimilació de dades per a l'estimació efectiva dels paràmetres electrofisiològics i mecànics rellevants que apareixen a les equacions, la qual cosa és un pas crucial cap a un model cardíac sensible a cada pacient. El codi computacional s'aplica per simular problemes físics reals. S'estudia la propagació electromecànica en una geometria de conill, on es prova la sensibilitat del model a les variacions d'entrada. En particular, l'eina de càlcul s'utilitza per avaluar la influència del camp de fibres cardíaques en la contracció del teixit.

Per desenvolupar una simulació cardíaca útil per a fins clínics, el model requereix la integració i combinació de la mecànica computacional i les tècniques de processament d'imatge més recents. El model resultant pot ser la base d'estudis teòrics sobre mecanismes de patologies, oferint als investigadors i cardiòlegs pistes addicionals per comprendre el funcionament del cor. Pot ajudar a la planificació de cirurgia i modelització, com és la predicció dels efectes de compostos farmacològics en el ritme cardíac o l'estudi de l'efecte de medicaments. Aquest projecte només és possible en un equip multidisciplinar, on grups especialitzats uneixen les seves forces en les respectives disciplines: cardiòlegs, investigadors imatge, bioenginyers i científics de la computació.

El present model computacional del cor és un pas més cap a la creació d'un laboratori cardíac virtual.

Glossary

CCM   Cardiac Computational Modeling

DT-MRI   Diffusion Tensor Magnetic Resonance Imaging

EF   Ejection Fraction

EM   Electromechanics

EnKF   Ensemble Kalman Filter

FD   Finite Diferences

FEM   Finite Element Method

FHN   FitzHugh-Nagumo

FK   Fenton-Karma

HPC   High Performance Computing

LV   Left Ventricle

MRI   Magnetic Resonance Imaging

ODE   Ordinary Diferential Equation

PDE   Partial Diferential Equation

PMJ   Purkinje Myocardium Junction

ST1   Linear interpolation of rule-based fiber field

ST3   Cubic interpolation of rule-based fiber field

Table of contents

Chapter 1

Introduction

*No man-made structure is designed like a
heart. Considering the highly sophisticated
engineering evidenced in the heart, it is not
surprising that our understanding of it comes
so slowly.*

Daniel D. Streeter
*Gross morphology and fiber geometry in the
heart.* Handbook of Physiology, 1979

1.1 Motivation

Cardiac computational biomechanics studies the use of computers to simulate the
heart, converting mathematical models to a code. Different approaches have been
used to model the dynamical behavior of biological systems, including mathematical
descriptions based on differential equations or cellular automata, which provide a model
of the activity of the organ, such as electrophysiology, mechanics or blood flow. In the
forefront of cardiac research, the knowledge of the morphology and the functional
processes of the heart has a vital interest due to their potential application to the
cardiovascular clinics. Experimental studies involving the *in-vivo* human heart are
possible and often available, but they are expensive and very limited. Therefore, well-
defined numerical modeling is emerging as a powerful tool that can help to interpret
experimental data, allowing the knowledge of phenomena not detectable by classical
clinical devices. Simulation can be the base of theoretical studies into the mechanisms

of cardiac pathologies, can provide diagnosis values (Chabiniok et al., 2012) or can be used to assist in therapy planning (Sermesant et al., 2012).

The framework proposed in this thesis aims to create a finite element model of excitation-contraction coupling of the heart based on cardiac data, using the latest advances in image processing and image acquisition. The model is one further step towards the creation of simulations with high precision, which could help to interpret clinical data. The framework could be integrated into medical analysis laboratories where several simulations would be performed on the patient's data. The results would be delivered to the doctor, who could take decisions on subsequent steps in the treatment: surgery, pacemakers, drugs, stents, etc.

Nowadays, this tendency can be observed in pharmaceutical companies, which already have specialized teams dedicated to mixed simulation and experimental techniques. They are interested in the prediction of the impact of pharmacological compounds on the heart's rhythm, using computer models, to improve the knowledge of drug study (Staab et al., 2013; Novartis, Novartis). The high performance computational (HPC) simulation tool should lead to a significantly reduction of animal experiments. This also would represent direct savings and reduction in product development for companies.

Creating a simulation of a physiological or pathophysiological process requires knowledge of the process itself. This realization is only possible in a multidisciplinary team, where specialized groups join forces in their respective disciplines. The present work involves medical doctors from several hospitals, image researchers, bioengineers and computational scientists, many of them with the skills extending beyond their core subject of research. This thesis presents the contribution in the project from the Computational Mechanics scientist's point of view. From this perspective, the issue of understanding how the heart works is amazingly appealing. The development of a HPC-based model of the pumping heart is presented and used to test cardiac properties. The aim is to help researchers and cardiologists to get a deeper insight of the system, and to speed-up our understanding, that "comes so slowly" (Streeter et al., 1969). With this objective, a computational code has been created to represent a new use of HPC resources in biomechanics.

Most of the criticism received in simulations of biological systems comes from the lack of better physiological models to represent real behavior. For these highly coupled and multi-scale systems, a better model means a more computationally expensive one to setup, calibrate and perform the data assimilation. Therefore, a simulation tool

that combines programming flexibility with efficient use of HPC opens a new research perspective.

1.2 Cardiac computational modeling

Cardiac modeling is a complex problem. The maturity of the models of electrical propagation in the heart is still not comparable with the one achieved in other engineering fields. Several causes can explain this difference:

- The heart muscle is a structure composed of cells, whose properties are non-linear, inhomogeneous, time-dependent and anisotropic.

- The biological processes are still partly understood. Direct observations of electromechanical (EM) propagation in the heart tissue is not trivial, and the experimental techniques have strong limitations.

- Experimental validation is still inaccurate and difficult to obtain, when compared to more traditional engineering problems on cars, planes or pumps.

- The problem is extremely multi-disciplinary. To obtain anatomical information and develop the model, the team involves cardiologists, radiologists, image researchers, bioengineers and computational scientists, with all kinds of communication problems among the players.

As a consequence, each observed behavior can have different interpretations according to antagonistic theories, creating strong controversies. One of the most representative is the answer to the simple question on how the heart pumps, even in a qualitative general answer. Pumping action is determined by the way the heart tissue contracts, which is in turn determined by the muscular tissue, which is in turn determined by the myocites orientation and distribution. For many years, the ventricular myocardium was described as a continuum in which myocite fibers orientation varied smoothly from the external side of ventricular wall (epicardium) to the internal side (endocardium). The defenders of this idea interpreted a large amount of experimental evidence as backing it, although one key issue remained obscure: How does a heart with this morphology contract to achieve the pumping rate observed? A second idea was left aside by the defenders of the first one, considered by them as incorrect. It states that the cardiac ventricular tissue is configured as a helical band with two spiral turns (Fig. 1.1). This theory was
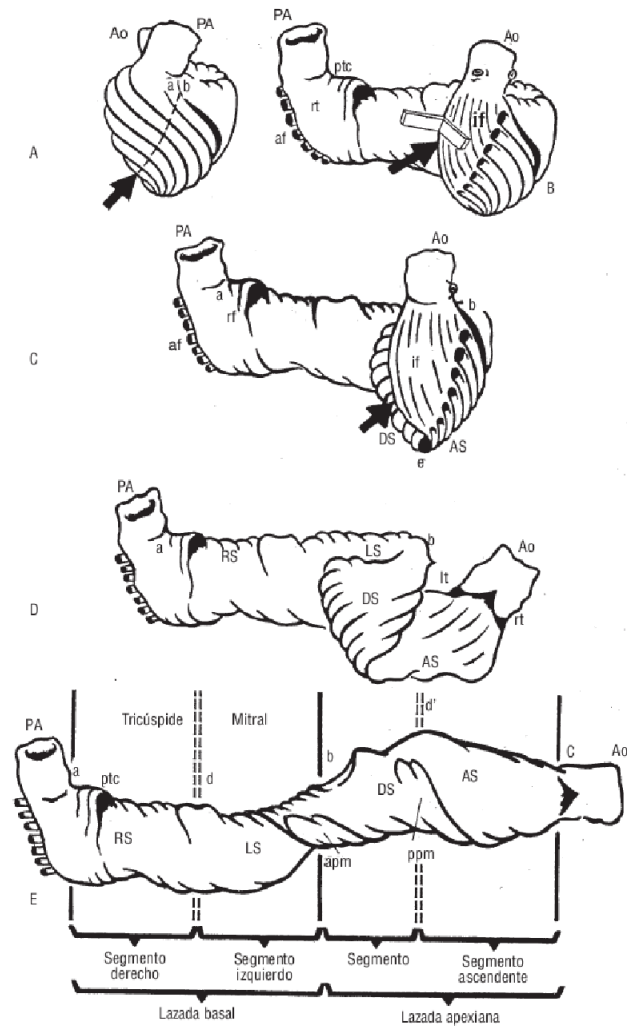
Figure 1.1: Ventricular myocardial band, Torrent Guasp drawing.

developed by Torrent-Guasp et al. (2005). Nowadays this controversial theory is still questioned under differing views.

Under the Computational Mechanics scientist's point of view, we cannot support any theory, but the development of a "computational heart" could help to study and assess controversial theories as the helical band.

Numerical model.   Heart simulation is a multi-scale problem. Many scales are strongly coupled, from cell descriptions of cardiac mechanisms to anatomical models of the organ. As stated by Legrice et al. (2001) the simulation scales covers eight orders of magnitude, "from the geometry of the cardiac chambers down to descriptions of ion channel or T-tubule density and distribution" which are tightly linked. At the

cell level, EM simulations are based on electrophysiological equations coupled with protein interaction models. Cellular models describe ionic currents and dynamics of the microscopic structures with a high degree of detail. They have been used to describe cellular properties as well as the influence of pharmaceuticals, neurotransmitters and mechanics. Despite all their advantages, it is impracticable to derive a whole heart by modeling every single cell (McCulloch and Huber, 2002).

At organ level, the reaction-diffusion equations describe the spread of the electrical impulse through the myocardium as a continuum. The excitation and electrical propagation process in cardiac tissue is coupled with the mechanical contraction, typically modeled with finite deformation elasticity theory, based on general conservation principles of space, mass and momentum. The present work focuses on the EM simulation of the heart at the continuum level. The code, Alya, is written in parallel, capable of running efficiently in thousands of processors. The starting point is the set of physical models that describe the constitutive parts of the problem. Then, numerical methods are developed to solve the group of non-linear partial differential equations (PDE) that governs the system. In this work, the Finite Element Method (FEM) is used to find the numerical solutions, rendering PDEs into an approximating system of ordinary differential equations (ODE). The FEM includes the 3D geometry, the fiber architecture, electrophysiology, finite strains, non-lineal properties and other features in the analysis. The complete problem can be divided into three parts: the electrical propagation, the mechanical deformation and the blood flowing in and out of the heart. This thesis attacks the first two topics and how they are linked together. The electrical propagation is modeled through non-linear equations representing an excitable media. The deformation is studied as a dynamic large-strain solid mechanics model with an appropriate Ogden-like material. The resultant HPC-based simulation tool provides the coupled EM propagation in cardiac geometries.

Cardiac imaging. To solve numerically electrical and mechanical components, the following anatomical components are used in this work:

- The geometry of the ventricular chambers.

- The definition of the fiber micro-structure.

The development of imaging techniques has facilitated the acquisition of accurate anatomical data required for the cardiac computational modeling (CCM). Nowadays, magnetic resonance imaging (MRI) is the reference modality for extracting the
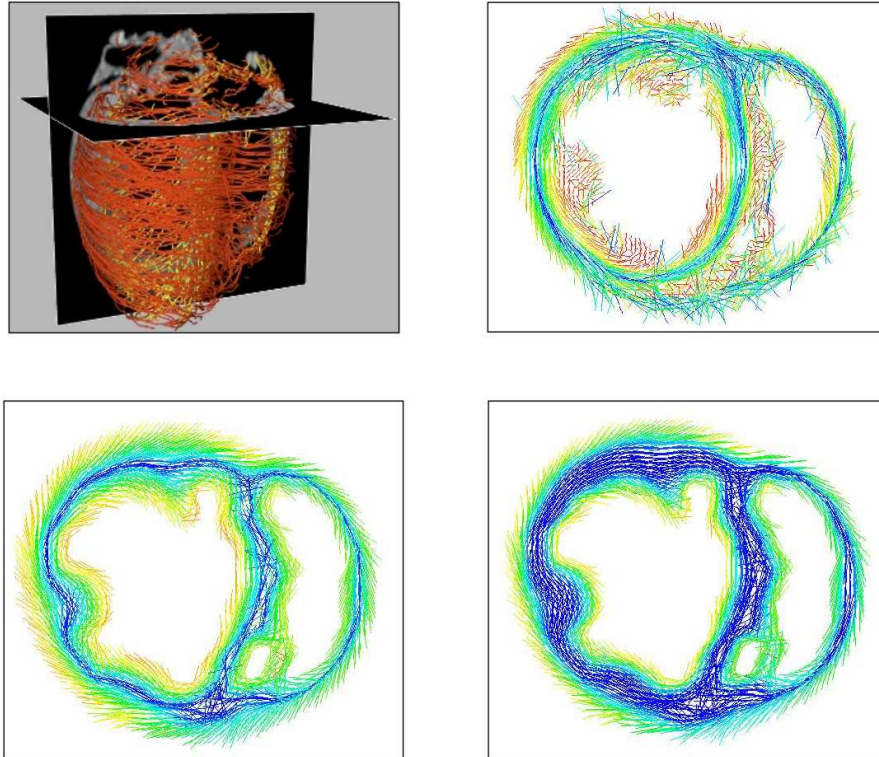
Figure 1.2: Section of the ventricles. Comparison of mathematical model of the fibers (linear and cubic) and experimental DT-MRI in a short cut of the ventricles. Colours represent the angle of the fiber field (from $-60°$ on the epicardium to $0°$ at mid-wall to $+60°$).

geometry of the ventricles. MRI is a noninvasive technique that enables accurate descriptions using strong magnetic fields and radiowaves.

Regarding the definition of the micro-structure, the orientation of muscle fibers can also be obtained using image techniques. Diffusion tensor MRI (also known as DT-MRI) has allowed the depiction of preferred orientation in the tissue (Basser et al., 1994). It has been shown that the main eigenvectors of tensors as acquired with DT-MRI correlate with the direction of the elongated myocytes in the ventricles (Scollan et al., 1998). However, most results are *ex-vivo* and can not be related to patient-specific studies directly. Nowadays, a challenging work to obtain results *in-vivo* is being developed in acquisition and image processing (Harmer et al., 2013; Toussaint et al., 2013; Nagler et al., 2013).

Unfortunately, cardiac images of geometry and fiber field are not always available. In those cases, mathematical descriptions are used to define the anatomy, assuming the error that the approximation involves. Figure 1.2 shows three possible orientations of the cardiac fiber field. Linear and cubic models represent mathematical descriptions of the microstructure and DT-MRI represents the experimental acquisition. Based on observations on anatomical dissections in mammalian hearts, those synthetic interpolations describe mathematically the variation of the fibers, from the epicardium to the endocardium. Colours in the figure represent the angle of inclination measured from the wall, typically from $-60°$ on the epicardium to $0°$ at mid-wall to $+60°$ in the endocardium.

Mathematical equations modeling the physics of the problem need to be solved in realistic geometries. Moreover, cardiac imaging is continuously improving, there is a wide field of research to remove noise in the acquisitions and to obtain high-resolution recordings. As the quality of the image increases in terms of both signal to noise ratio and spatio-temporal resolution, cardiac accurate models need more computational resources to take profit from this detailed information. Consequently, HPC is a strong tool that can contribute to obtain realistic simulations of the heart using all the information of the detailed data available. The creation of virtual models based on cardiac imaging, using the most recent advances in this field, can be a platform to test new techniques, validate theories, design early clinical trials or predict clinical results.

Data assimilation   Electrical and mechanical models that govern the simulation of the heart contain a large number of parameters in their equations, which often cannot be measured directly or that have to be acquired *ex-vivo*. Although some of them can be found in the literature, a special calibration of these values is required to adapt the simulation to an specific cardiac mechanism.

Data assimilation permits a non-invasive characterization of the parameters that can be used to fit the simulation, to describe and predict the behavior of the system. In particular, data assimilation combines the information available from experimental sources with models describing the cardiac mechanism to estimate the unknown quantities of interest. In terms of clinical applications, data assimilation can improve the cardiac model and assist in diagnosis (Wang et al., 2013; Chabiniok et al., 2012; Xi et al., 2012). Once data assimilation has been performed, the model can be used to predict the evolutions of the system. Consequently, diagnosis could be improved by adapting the simulation to a patient.
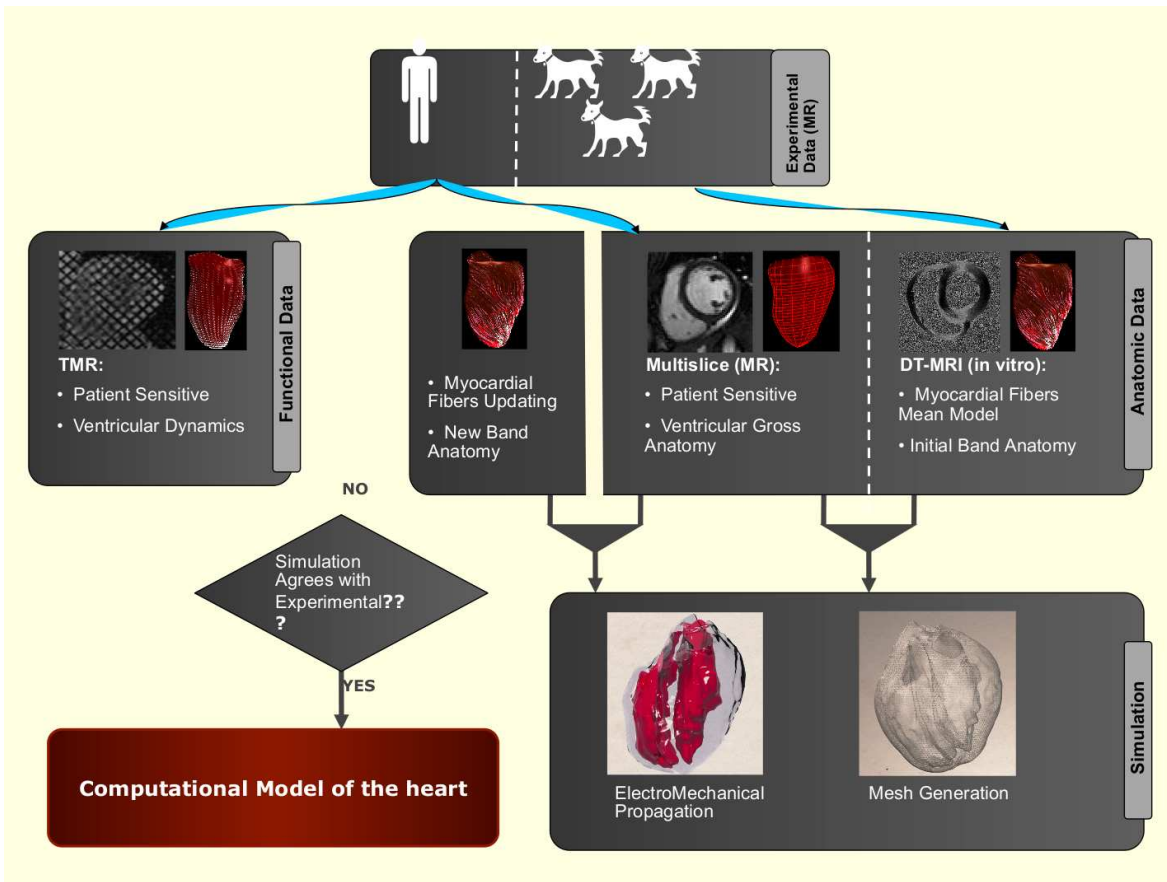
Figure 1.3: Interaction between computational mechanics and image processing techniques. This multidisciplinary project is composed by Hospital de Sant Pau, Centre de Visio per Computador (CVC) and Barcelona Supercomputing Center (BSC). Image designed by Debora Gil (CVC).

Outline of the multidisciplinary project. The HPC-based computational model is a useful tool that can be applied in many multidisciplinary fields. Most of the times, the processing power of computers available to clinical researchers is too limited to simulate physiological and disease mechanisms. In this context, computational scientists are crucial. In the future, the CCM tool presented here aims to cover different clinical disciplines. For example, in pharmaceutical research, the design of HPC-based simulations could improve the time and cost factors in areas such as drug development.

In this thesis, the integrative model requires combining computational mechanics and image processing techniques to develop a cardiac simulation useful for clinical purposes. One possible interaction between the players that compose the computational simulation of the myocardium is illustrated in Figure 1.3. The ideal study provides the geometry of the ventricles and the spatial disposition of the muscular fibers to allow the estimation of the EM sequence of the heart. The anatomy of the ventricles is obtained

from images and is converted into a computational mesh where the numerical equations are solved. Functional data (cardiac deformation) can be recorded through Cine MRI or ultrasound echocardiography. Both modalities provide reliable measurements of intramural motion that could be used to calibrate the simulation. The resultant simulation of the CCM tool is compared with the experimental 3D motion. Ideally, it should match the observed behavior of the heart. This multidisciplinary project is composed by Hospital de Sant Pau, Centre de Visio per Computador (CVC) and Barcelona Supercomputing Center (BSC).

However, the current technology for reconstruction of 3D motion has a temporal resolution that might not be high enough to produce reliable contractions. Advances in medical imaging have the potential to meet the demands of the requirements of this approach. The improvement of 3D motion is crucial to personalise the cardiac simulation.

1.3 Goals of the thesis

This PhD thesis represents an effort in helping cardiologists to grasp the underpinnings of cardiac dynamics, considering that simulations of biological systems are a complementary tool for physicians to study the organs. The tools developed here should give medical researchers additional hints to understand the heart. The use of numerical simulations in therapeutic applications is in the way of becoming a reality, allowing medical doctors to make decisions on subsequent steps in the patient diagnosis and treatment.

This works aims to investigate some aspects of the mathematical and numerical modeling of the cardiovascular system, focusing on:

- The electrophysiological simulation of the heart

- The mechanical simulation of the heart

- The weak EM coupling

- The HPC-based simulation

The computational electrophysiology and computational mechanics are implemented in the same computational tool, Alya, which also solves other engineering problems. Under Alya Red, we group all the biomedical research projects. The resulting software

is then targeted to biomedical research and based in a general purpose simulation code for coupled multiphysics and programmed for parallel computers. This strategy allows a great flexibility to cover the wide range of problems found in biological systems, being all of them seen in the same way and as any other engineering problem: systems of differential equations coupled together. Alya has no dependency on third-parties libraries, being all solvers developed in-house. The coupled EM solution requires solving electrical and mechanical components, which are performed in the same computational code. The simulation tool is flexible enough to introduce all the necessary modelization improvements, preserving the main features, particularly the scalability. In this thesis, electrophysiological and mechanical models are implemented. The CCM tool is used to test properties of the heart. We analyze its potential on EM cardiac applications through a sensitivity analysis and we present a framework that emphasises the possibility to optimise cardiac models.

Questions and Hypotheses of the work.   The work presented here is one of the biomedical problems solved in Alya and means a preliminary step towards the virtual heart simulator. The questions and hypotheses that have been arisen to build and develop the framework are summarized as follows:

- Is HPC necessary?

  Computational meshes are commonly used in numerical simulations, offering the advantage of describing the topology and the geometry of the organ as precisely as required. Nowadays, some anatomical data is hard to obtain, for example the orientation of the fiber field in the heart. Since cardiac imaging techniques are improving fast, the newest technology allows to acquire at a high resolution. In the near future, it will increase even more. Therefore, we have to be prepared to use all the information coming from the new medical equipments to consider the increasingly high resolution obtained from the clinical images. High resolution at both geometrical and material levels produce high resolution meshes in the electrical and mechanical problems, which makes high fidelity simulations. HPC is necessary to compute the models of the heart in a fine mesh, which considers all the detail of the geometry that comes from high definition acquisition.

  In addition, to perform a sensitivity analysis in a cardiac geometry HPC is also needed. One simulation can run in several days in a single computer. If we pretend to analyze the effect of the input parameters in the contraction of the muscle, we need to run a large amount of cases, as it is done in this work.

Finally, the electrophysiological, material and coupling models of high complexity have up to a hundred of degrees of freedom per node. If we use complex models in the cardiac simulation, computer resources are also required.

- Why simple electrophysiological models are used in this thesis?

  Alya's flexibility allows to easily program a large variety of physiological models for each problems that needs to be solved. The purpose of this thesis, is to develop an EM propagation of the heart, including the mutual coupling. To simulate the global pumping action, complex models are not required. Models including detailed information of the ionic processes that occur in the contraction of the muscle are suitable for other studies, such as the effect of drugs in pharmaceutical studies. Those models are already implemented in Alya (O'Hara-Rudy, Grandi-Bers) but are not used in this thesis. Instead, Fitz-Hugh Nagumo and Fenton-Karma models are used to run all the simulations.

- Why a fine mesh is needed in the EM simulation of the heart?

  In the case of the heart, a fine mesh is necessary to prescribe the anatomical details of the heart available from cardiac images, specially the fiber field orientation. The fiber field information is crucial to develop an EM simulation because it determines the resultant movement of the organ. The orientation of the cardiac fiber field influences the contraction of the heart. Mathematical fiber models can be interpolated in the cardiac geometry when the real data is not available. They are useful and probably suitable to obtain optimal simulations. However, we aim to use the experimental data and all the anatomical description of each case when it is possible.

- Why to solve the electrophysiology and the mechanical deformation of the problem in the same computational mesh?

  Electrophysiology and mechanical deformation are solved on the same mesh, with no interpolation. This method allows to avoid stability issues and interpolation errors, paying the price of a high computational cost for the mechanical problem. As all problems are programmed and solved in the same code, supported on the same mesh and with the same parallelization scheme, we find our approach very natural.

- Why to solve both electrical and mechanical problems in the same code?

  Alya is a multiphysics code, specially build to solve complex problems. If everything is programmed in the same code, the control over the development of

the model is broader. This also allows improvements and new capabilities to be exploited.

1.4   Background

This thesis focuses on modeling the heart as an organ, based on conservation laws and differential equations that describe the excitation and propagation process in cardiac tissue coupled with the mechanical contraction of the muscle.

The first electrophysiological model was published by Hodgkin and Huxley (1952), where the authors described the dynamics of the transmembrane voltage V_m and ionic currents through the axon membrane. Given the equivalence with cardiac cells, their work on neurons could be used by cardiac scientists to describe the electrical behavior of the heart. A reduction and adaption of Hodgkin-Huxley model to cardiac cells was published by FitzHugh (1961). Due to its simplicity and generality, the FitzHugh-Nagumo (FHN) model has been used widely and is good trade-off for comparisons and simulations (Murillo and Cai, 2004). More complex electrophysiological models have been developed since the late nineteenth century, ranging from single cell (Noble. D, 2001; Ten-Tusscher and Panfilov, 2006), to tissue and organ level (Vigmond et al., 2003; Noble, 2007). Several works have shown how those computational models can be applied to describe 3D phenomena (Penland et al., 2002; Murillo and Cai, 2004; Fenton et al., 2005).

Regarding the simulation of the cardiac contraction, Mirsky (1973) introduced the first model, considering a non-linear problem with great strains and incompressible material. After this first approach, mechanical models incorporated the description of the fiber orientation (Streeter et al., 1969) in the analysis of the stress (Yin et al., 1987). Nowadays, mechanical models account for the anisotropy of the tissue, considering different properties in the planes perpendicular to the fiber direction and through the thickness (Humphrey et al., 1990; Guccione et al., 1991; Costa et al., 1996; Holzapfel and Ogden, 2009). Although the simulation of the contraction in the heart has been studied extensively, there is less published work in the area compared to the electrical modeling.

Fully coupled EM simulations combine both electrophysiology and mechanics. At the organ level, electrophysiological models are based on reaction-diffusion systems and mechanical models are based on finite deformation elasticity theory. The first coupled EM models that considered the 3D fiber geometry and used the FEM to solve the

equations were developed by Hunter and Smaill (1988) and Nielsen et al. (1991). In the last decades, EM models improved quickly in terms of precision and they have been used to investigate pathological phenomena (Cherubini et al., 2008; Niederer and Smith, 2008; Campbell et al., 2009; Keldermann et al., 2010; Trayanova, 2011; Land et al., 2012). Although fully coupled EM modeling is still the exception rather than the rule in cardiac modeling (Trayanova and Rice, 2011), EM simulations have become of increasing use to understand the properties of the heart. Currently, cardiac models are sufficiently accurate to simulate complex processes. In many cases, they have been proved useful for predicting cardiac mechanisms as resynchronization therapy (Kerckhoffs et al., 2009; Constantino et al., 2012; Sermesant et al., 2012), patient-specific applications (Smith et al., 2011; Niederer et al., 2012; Chabiniok et al., 2012; Krishnamurthy et al., 2013) or cardiac growth (Kerckhoffs et al., 2012). The coupled EM problem is significantly demanding in terms of computing (Nickerson et al., 2006). The development of fully coupled 3D solution in large computational domains has been limited due to extremely high computational cost. Particularly, electrophysiology is a more computationally expensive exercise than the mechanical one. Until recently, EM models have been used successfully to study different aspects of cardiac functions, but are made of relatively small meshes. Nowadays, few models are prepared to run on large supercomputers, particularly for the coupled EM case. This lack of resolution is an obstacle when trying to reproduce the complexity of fiber distribution.

Weak coupled models solve the electrophysiology and mechanics problems separately, with only the timing of activation passing between the two systems. The alternative method is the strong coupling between electrophysiology and mechanics, where both systems are solved simultaneously. Up to the author's knowledge, the groups that develop EM models of the heart at the organ level are summarized here:

- *University of California (UCSD).* The Cardiac Biomedical Science and Engineering Center has developed a coupled EM model in an anatomical heart geometry to study the effects of pacing on synchrony (Kerckhoffs et al., 2006). They use models that represent the cellular electrophysiology to study the benefit of biventricular pacing in a canine heart, in the presence of left bundle branch block (Usyk and McCulloch, 2003).

- *Johns Hopkins University (JHU).* The Computational Cardiology Laboratory has developed a coupled EM model in the canine ventricles to study pathologies as arrhythmia or dyssynchronous heart failure (Trayanova, 2011).

- *University of Tokio (UT).* The UT-Heart Laboratory has developed a multi-scale and multi-physics simulator prepared to perform massively parallel computations. They solve the governing equations of the coupled EM problem, including the ventricular blood flow, using the FEM. The domain is discretized in voxel elements and tetrahedral elements to analyze the electrical and mechanical phenomenon respectively. They apply the simulator on virtual cells and to develop therapeutic devices such as the basic design of an implantable defibrillator (Watanabe et al., 2004; Sugiura et al., 2012).

- *King's College London (KCL).* The research group is focused on the development of computational models of the heart with the capacity to integrate multiple measurement types. The multiscale modeling combines detailed cellular dynamics, electrophysiology and deformation models within a common anatomical heart geometry (Niederer and Smith, 2008; Nordsletten et al., 2010).

- *IBM Research.* The group has developed a code that runs on the Blue Gene supercomputer. They plan to involve higher spatial resolution in the cardiac model.

- *INRIA.* The M3DISIM team has developed a 3D EM model of the ventricles, using FHN model for the transmembrane potential propagation. The contraction is modeled through a constitutive law including an electromechanical coupling (Sainte-Marie et al., 2006; Sermesant et al., 2012; Chapelle et al., 2012; Caruel et al., 2014). The model enables the introduction of pathologies and the simulation of electrophysiology interventions.

- *Stanford University.* The Department of Mechanical Engineering has developed a coupled cardiac EM simulation, proposing a fully implicit, FEM-based modular approach (Goktepe and Kuhl, 2010).

- *Simula Research Laboratory.* The Computational Cardiac Modeling group develops mathematical models of cardiac electromechanics for strongly coupled EM simulations (Sundnes et al., 2014).

- *University of Auckland (AU).* The team has developed a computational model for cardiac EM which couples cellular, tissue, and whole heart modeling paradigms (Hunter et al., 1997; Nickerson et al., 2006).

- *Karlsruhe Institute of Technologgy (KIT).* The group develops computer models of the human heart, modeling and measuring electrophysiological properties of

myocardial cells and tissue for the development of forces (Seemann et al., 2003). The framework is applied to study the effect of heterogeneity in the EM coupling.

- *Politecnico di Milano.* The Laboratory for Modeling and Scientific Computing focuses on the development, analysis and computer implementation of mathematical models for the cardiovascular system. The group studies the coupling between cardiac mechanics and electric signal (Ambrosi et al., 2011)

- *Zhejiang University, Hanzhou.* The group has developed a a unified EM model of the heart at cell level (Xia et al., 2006; Wong et al., 2008). They propose an integrated framework for noninvasive personalization of cardiac electromechanics by combining an integrated cardiac Physiome model and multi-modality observations (Mao et al., 2012).

- *Ecole Polytechnique Federale de Lausanne (EPFL), Switzerland* The Laboratory of Multiscale Modeling of Materials study the interaction between the propagation of the electrical potential through the cardiac tissue (modeled by bidomain equations), and the mechanical response, assuming a decomposition of the deformation gradient between an active and a passive factors (Rossi et al., 2012).

- *Barcelona Supercomputing Center (BSC).* The group develops a computational tool, Alya, that combines the experience acquired in electromechanics and the background in HPC techniques. Electrophysiological models coupled with the mechanical contraction of the muscle are computed and a coupling scheme that link both problems together. The non-linear equations are solved using the FEM with an explicit time scheme using the same computational mesh. The present scheme shows almost linear scalability plots for thousands of processors (Vázquez et al., 2011; Lafortune et al., 2012; Marin et al., 2013). The simulations are performed in Marenostrum, the most powerful supercomputer in Spain, which is hosted in BSC.

Chapter 2

The physical problem: the heart

In this chapter, a basis about the physiology, structure and mechanical properties of the heart is provided, as well as some of the currently used methods for the acquisition of cardiac data.

2.1 The cardiac tissue

The heart is a muscular organ responsible for pumping blood by repeated and rhythmic contractions. In adult humans, the heart weights approximately 250 to 350 g and is usually situated in the middle of the thorax. It is composed of semi-striated muscle that functions by contraction, causing the muscle cells to shorten. It contracts 72 beats per minute.

2.1.1 Cardiac electrophysiology

The wall of the heart has three layers: The *epicardium*, *myocardium* and *endocardium*. Endocardium and epicardium are thin layers consisting primarily of collagen and elastic tissue. In the middle layer, the myocardium, the cells that constitute the muscle show electrical excitability. These specialized cells, called myocytes, are organized into parallel cardiac fibers giving the muscle the striated appearance. The fibers form sheets which are connected one to another by collagen (Fung, 1993), (Fig. 2.1).

Four chambers can be distinguished in the heart: two atria and two ventricles (Fig. 2.2). The interatrial septum is the wall that separates the right and left atria of the heart and the interventricular septum separates the ventricles.
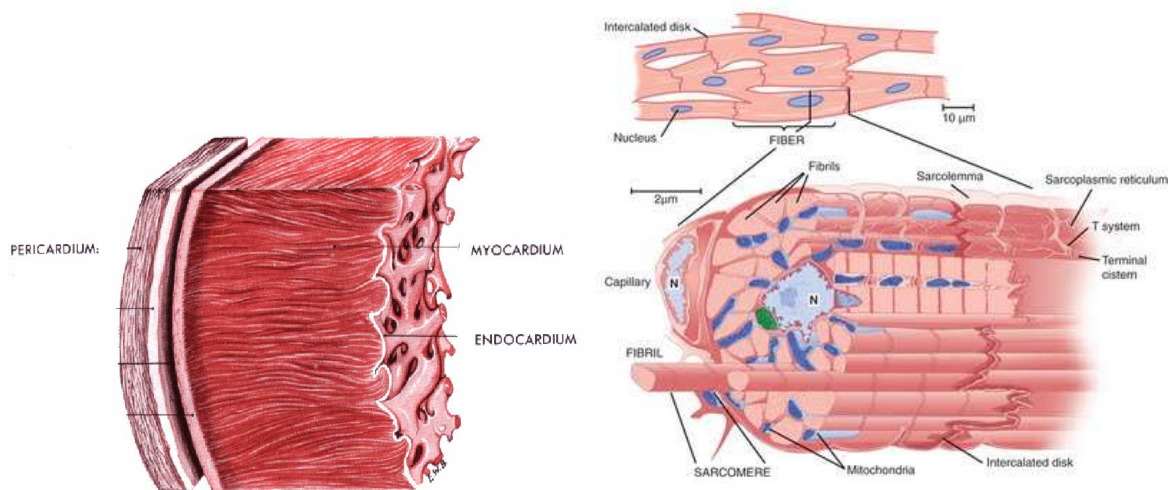
Figure 2.1: Sections of cardiac muscle. Heart wall showing the pericardium, myocardium and endocardium (left). Cardiac fibers give a striated aspect to the myocardium (right). Image by Stephen Gallik.

The valves of the heart are located within the chambers, preventing the back flow of blood. The tricuspid valve is placed between the right atrium and right ventricle and the mitral valve is situated between the left atrium and the left ventricle. Right ventricle (RV) pumps blood to the lungs for oxygenation through the pulmonary artery. Left ventricle (LV) pushes blood into the aorta to deliver it to all the body tissues, pumping blood at a higher pressure than the RV.

The action potential.   A cardiac cell (myocyte) is typically 10 to 20 μm in diameter and 80 to 125 μm in length. The cell membrane acts as an electrical insulator and contains *ion channels* which transport electrical current by diffusion. The potential difference across the membrane is called *transmembrane potential*. Initially, a cardiac cell is at rest, with a potential difference across the membrane. The potential inside the cell is negative compared to the external. If the membrane potential rises to a certain threshold value (close to 40 mV) a rapid process occurs, which can be explained in different phases:

- *Resting membrane potential:* The membrane is polarized at the resting state value of -85 mV. The $Na^+ - K^+$ ATPase is active and exchanges the intracellular Na^+ with the extracellular K^+. The fast Na^+ channels are closed.
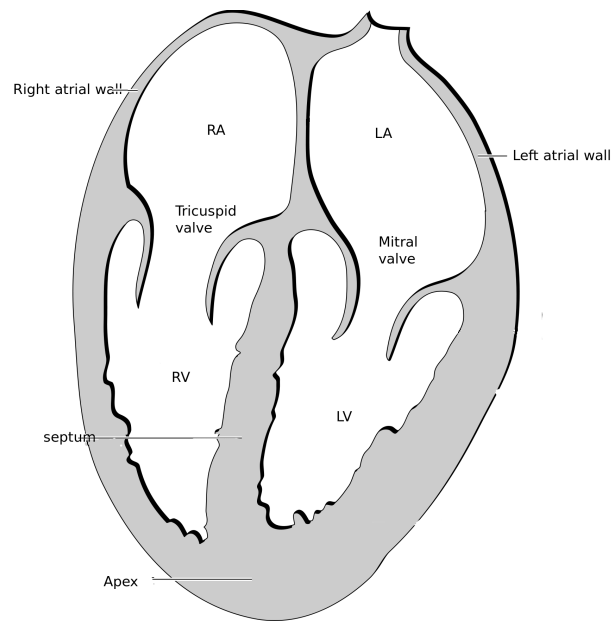
Figure 2.2: Longitudinal cut of the heart showing the four chambers. Illustration by CC Patrick J. Lynch and C. Carl Jaffe, Yale University, 2006.

- *Depolarization:* An excitation opens the fast Na^+ channels, causing a large influx of ions through the membrane and rapid increase of conductance to these ions. The cell changes its potential becoming V_{max} less negative.

- *Early repolarization:* Inactivation of the fast Na^+ channels. A current of K^+ tries to recover the equilibrium of the action potential to the resting state.

- *Plateau:* There is a balance between an inward movement of Ca^{2+} and the outward movement of K^+.

- *Repolarization:* Ca^{2+} channels close while K^+ channels are still open. The cell loses its positive charge and causes the cell to repolarize. K^+ channels close when the membrane potential is restored to -85 mV.

The charge is transported by the ionic currents and is accumulated at the membrane (Fig. 2.3). The complete cycle of depolarization and repolarization is called action potential and is illustrated in Figure 2.4.

Typically, the cell changes its potential in presence of external stimulus coming from an adjacent cell. However, certain cells of the heart have the ability to generate an action potential without any influence. Changes in the electric voltage of the cell drive the mechanism to contract. The calcium concentration allows the interaction between
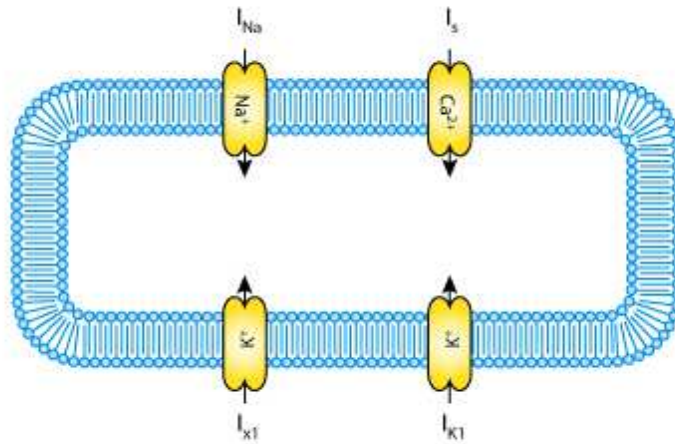
Figure 2.3: Schematic diagram describing the current flows across the cell membrane. From the CellML Project.
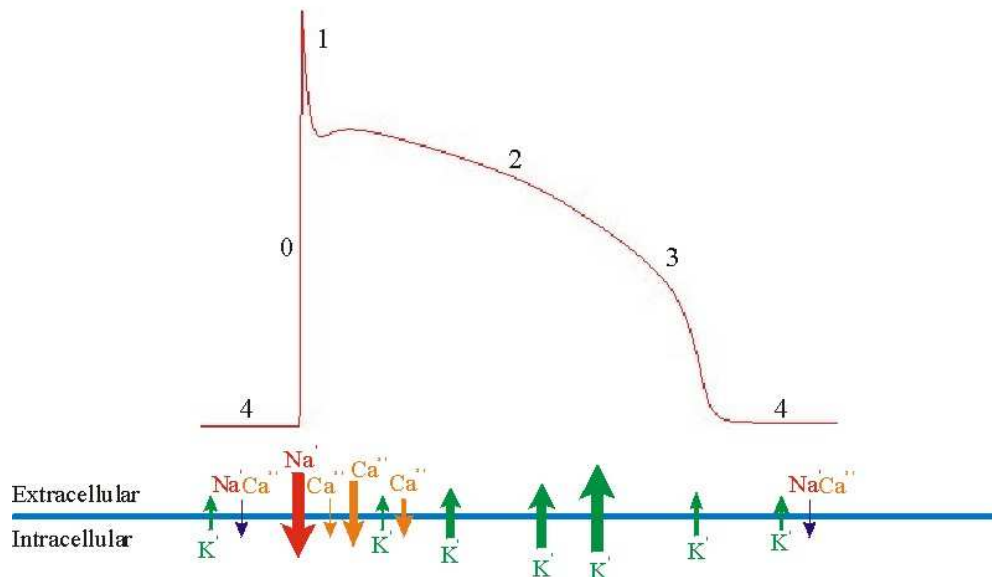

Figure 2.4: Phases of an Action potential: (0) Sodium enters the cell through fast sodium channels; (1) Fast sodium channels close; (2) Calcium and additional sodium enter the cell through slow channels; (3) Potassium exits the cell, and resting membrane potential is reestablished; (4) Equilibration of sodium and potassium occurs.
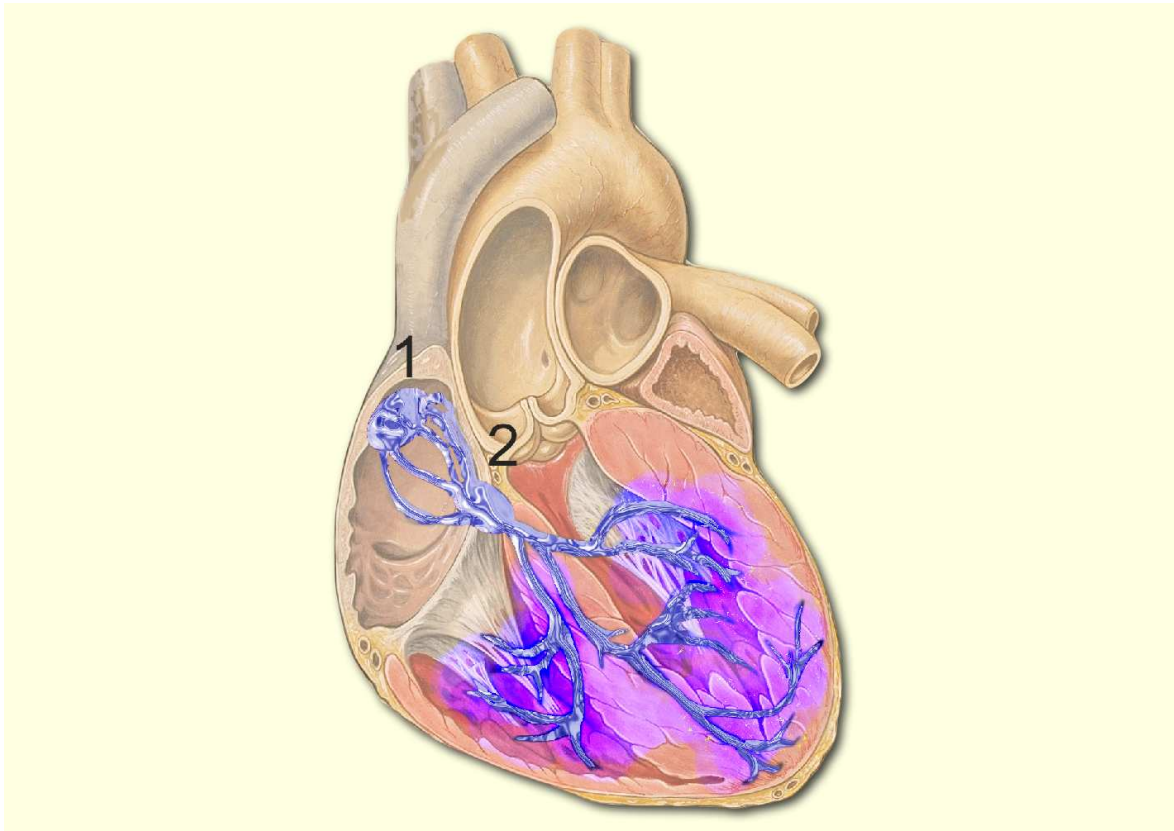
Figure 2.5: Illustration of the heart muscle showing the sinoatrial (1) and atrioventricular (2) nodes and the Purkinje system. By CC Patrick J. Lynch and C. Carl Jaffe, Yale University, 2006.

actin and myosin proteins in the intracellular domain. The myocytes generate an active tension making the cell to shorten.

Purkinje system. The electrical signal that triggers contraction enters from the atrioventricular node to the bundle of His. This bundle branches out into a tree-like structure called Purkinje fibers, which provide rapid delivery of the electrical impulse (Fig. 2.5). Purkinje system and myocardium muscle are electrically connected through transitional cells called myocardium junctions (PMJs), distributed throughout the ventricular subendocardial layer.

2.1.2 Cardiac mechanics

From a mechanical point of view, heart muscle is mainly composed of a thick layer of myocytes assuming the pumping function of the heart (Fig. 2.6). The tissue is considered a nonlinear, anisotropic, viscoelastic and slightly compressible material

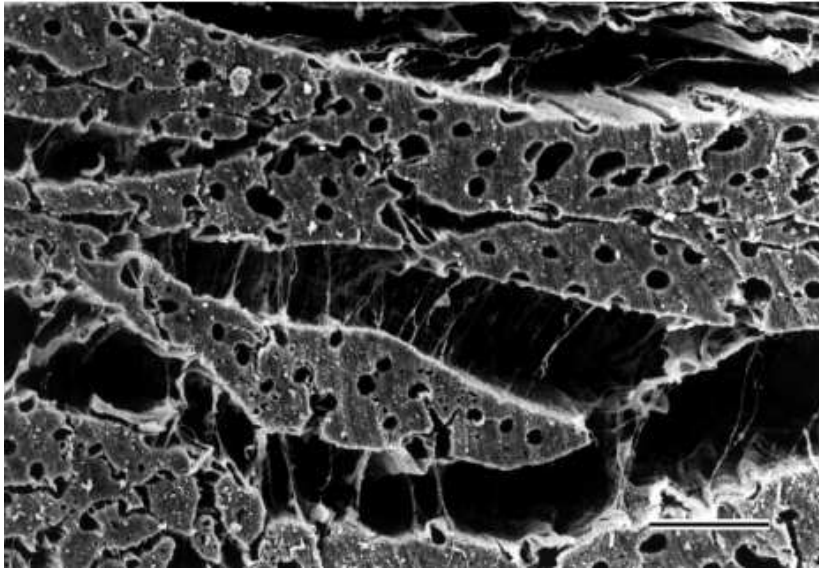Figure 2.6: Scanning electron microscopy of the myocardium sectioned perpendicular to the fibers (Legrice et al., 2001). Fibers, muscle bridges and collagen are visible.

(Fung, 1993; Yin et al., 1996; Humphrey, 2001). Taking into account the behaviour of the myocardium, the stress of the muscle is divided in two parts:

- The active stress represents the active component of the embedded muscle fibers. The active part is generated by the contractile cells when they are electrically stimulated.

- The passive part represents the contribution of the surrounding matrix of connective tissue, mostly collagen and elastin.

2.1.3   The cardiac fiber field

Cardiac fibers are necessary to prescribe both, electrical and mechanical properties of the myocardium. A detailed description of the cardiac fiber architecture is important for an accurate electromechanical modeling. In the last decades, several studies have been performed to inspect the cardiac fiber field, based on the measurements of angles of fiber orientation through the ventricular wall (Streeter et al., 1969; Armour and Randall, 1970; Greenbaum et al., 1981; Legrice et al., 2001). Dissections on mammalian hearts measured the angles of fiber slope, giving a detailed map of the fiber directions in the heart. These works show the complexity of the cardiac fiber direction. From this,
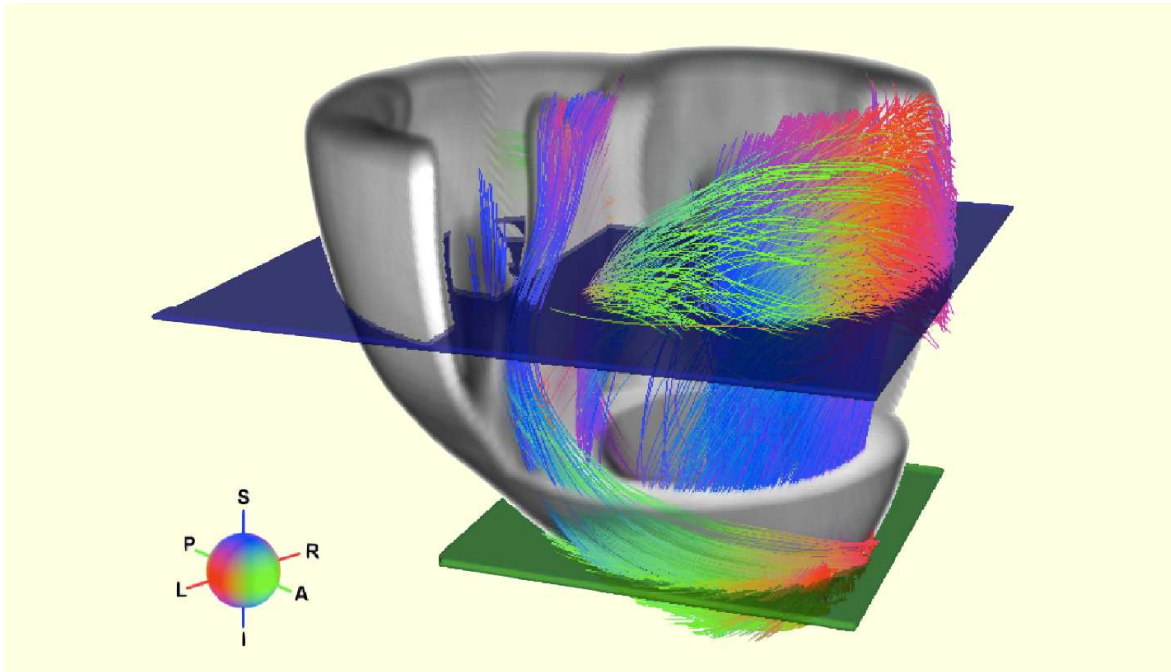
Figure 2.7: Representation of the cardiac fiber field (Peyrat et al., 2006).

mathematical models have been constructed, integrating the fiber orientation. In these synthetic cardiac structures, the angle varies from base to apex across the wall (i.e. transmural), from $-60°$ to $-70°$ in the epicardium to $60°$ to $70°$ in the endocardium (Fig. 2.7).

The fiber directions in the cardiac muscle have an important role. The orientation of the cardiac fibers is necessary in the prescription of the electrophysiological and mechanical behavior of the heart and the coupling between them. In the electrical part, the primary direction of the propagation is the longitudinal fiber direction. In the orthogonal directions, conductivities have the same value but different from the conductivity along the fiber direction. Specifically, the conduction velocity is three times faster along the myocardial fibers than in a perpendicular direction (Rubart and Zipes, 2001; Coghlan et al., 2006). Regarding the mechanical contraction, the fiber distribution influences the active part of the stress. Finally, the fiber field is also necessary in the electromechanical coupling. The excitability of cardiac fibers is determined by the increase of the cellular $[Ca^{2+}]$ concentration, which increases the force of contraction.

Nowadays, measuring these directions in a living heart is still an open-challenge. Models constructed from geometrical data acquired in-vivo are not able to image fiber orientation. Consequently, cardiac models have to include an approximation of the fiber architecture instead of the real one. There are two options for obtaining the vector

fields over the whole myocardial volume, image-based and rule-based methods. The main characteristics of experimental and synthetic fiber models are presented here:

Diffusion Tensor Imaging.   In recent years, Diffusion Tensor Magnetic Resonance Imaging (DT-MRI or DTI) has emerged as a powerful tool for the experimental measurement of cardiac fiber structure. This method is based on the assumption that water diffuses along the myocardial fiber orientation. Applying magnetic field gradients in at least 6 directions in the cardiac sample, it is possible to calculate a tensor T that describes the 3-dimensional shape of the diffusion. This matrix is symmetric and positive. The eigenvalue decomposition leads to $T = PDP^T$, were P is the eigenvectors matrix and D the diagonal matrix of the eigenvalues. The eigenvalues of the diffusion tensor quantify the diffusion rate of water molecules within the tissue structure along the directions given by the corresponding eigenvectors. Finally, the fiber direction is indicated by the tensor's main eigenvector.

DT-MRI is a non-invasive technique which allows a direct measurement of the anisotropy (Basser et al., 1994). However, DT-MRI data is noisy and the quality of the reconstructed images is related with the number of DT-MRI acquisitions. An average model can be obtained combining reconstructions of the same heart sample, giving better quality to the distribution. Up to date, a full 3D DT-MRI acquisition of the fiber data requires extremely long times to achieve the minimal accuracy for the reconstruction (several hours) and can only be performed on *ex-vivo* hearts (Helm et al., 2005). Novel studies in 2D show that the acquisition of high resolution *in-vivo* is becoming feasible (Gamper et al., 2007; Toussaint et al., 2010, 2013; Harmer et al., 2013). Due to cardiac motion, the acquisition of high resolution *in-vivo* DT-MRI is a challenging task. In the near future, the improvement of this technique will lead to a simulation of the human heart including the anatomy and the anisotropic structure of the human organ, both acquired *in-vivo*.

Rule-based fiber models.   The experimental fiber field is not always available. For this reason, rule-based models describing the cardiac fibers are frequently used. Based on experimental measurements such as in Streeter et al. (1969), the fiber orientation is generated by mathematical algorithms. Rule-based models are validated comparing to those in the same geometrical model but with DT-MRI-derived fiber orientation.

In Potse et al. (2006) the following rule-based approach is described. For each ventricular node, the minimal distance d between endocardium and epicardium is

calculated (d_{endo}, d_{epi}). The transmural variation of the fiber field is represented from $-\theta$ on the epicardium to 0 at mid-wall to $+\theta$ on the endocardium, by using the epicardium to endocardium surface distance d. The value of θ usually varies between 60° and 70°. A thickness parameter is defined as

$$e = \frac{d_{endo}}{d_{endo} + d_{epi}} \tag{2.1}$$

The interpolation of the fiber along transmural direction is defined as

$$\theta = R(1 - 2e)^n \tag{2.2}$$

where $R = \pi/3$ for the LV and $R = \pi/4$ for the RV.

This approach has shown some success in ventricular models with basic geometries (Potse et al., 2006; Bishop et al., 2010). However, minimal distance parametrization can yield to singularities in the minimal distance function in realistic geometries, particularly in the septum (Bayer et al., 2012). The advantages of synthetic fiber field models are:

- Fast algorithm and fast implementation

- Fiber direction can be modified to examine its effect in propagation

- New fiber models can be incorporated

- Long acquisitions required to acquire in-vivo fiber data are avoided

Moreover, new studies present a method to personalize the fiber architecture. Based on inverse techniques as the Unscented Kalman Filter, the parameters of the rule-based fiber model are estimated from DT-MRI-derived fiber data (Nagler et al., 2013).

2.2 Electrophysiological models

Modeling the molecular structure of the heart involves a large number of cells. To simulate the electrical activity in the myocardium, one possible approach is to model each cell as a separate unit and couple them together using specific mathematical models. Since this method is numerically expensive, this type of model is useful for small samples of tissue. To avoid the difficulties in the resolution of the mathematical equations, in this thesis the electrical phenomena is studied in a macroscopic level.

At the organ level, reaction-diffusion systems reproduce continuous approximations of the excitation of cardiac muscle (Hunter, 1983). Nowadays, two models are widely used in electro-cardiology to simulate the propagation of the action potential waves in the cardiac tissue: the bidomain and monodomain models.

The bidomain model.   It represents a well-established description of the electrical activity of the myocardium on a macroscopic scale, taking into account the ionic current, the membrane potential and the extracellular potential. In the bidomain model, the simulation of the ionic current requires the solution of a system of partial differential equations (PDE's), with an implicit analysis. The model considers that the muscle cells are connected via small channels in the cell membrane, where substances such as ions pass directly from one cell to another.

The model is suitable for problems that require ion exchange calculations, such as the study of defibrillation or induced arrhythmia in small samples of cardiac tissue (Trayanova et al., 2006). In these applications, the bidomain model captures the tissue behavior.

The monodomain model.   The monodomain model is a simplification of the bidomain equations. It assumes that conductivities are proportional in the intracellular and extracellular spaces. The advantage of the model is that it produces realistic activation patterns, useful for analysis and simplified electrophysiological studies. Depending on the purpose of the study, the monodomain model is accurate enough to simulate the action potential (Sundnes et al., 2006; Potse et al., 2006). However, it cannot be applied in all situations because it does not permit currents in the extracellular domain.

2.2.1   The physiological governing equations

Hodgkin and Huxley (1952) introduced the first continuous mathematical model designed to reproduce cell membrane action potentials. Since then, there has been many complex models developed for cardiac cells following their approach. In general, the action potential $V(x_i, t)$ is modeled using a reaction-diffusion equation through a macroscopic continuous media, which is combined with a microscopic model. The basic
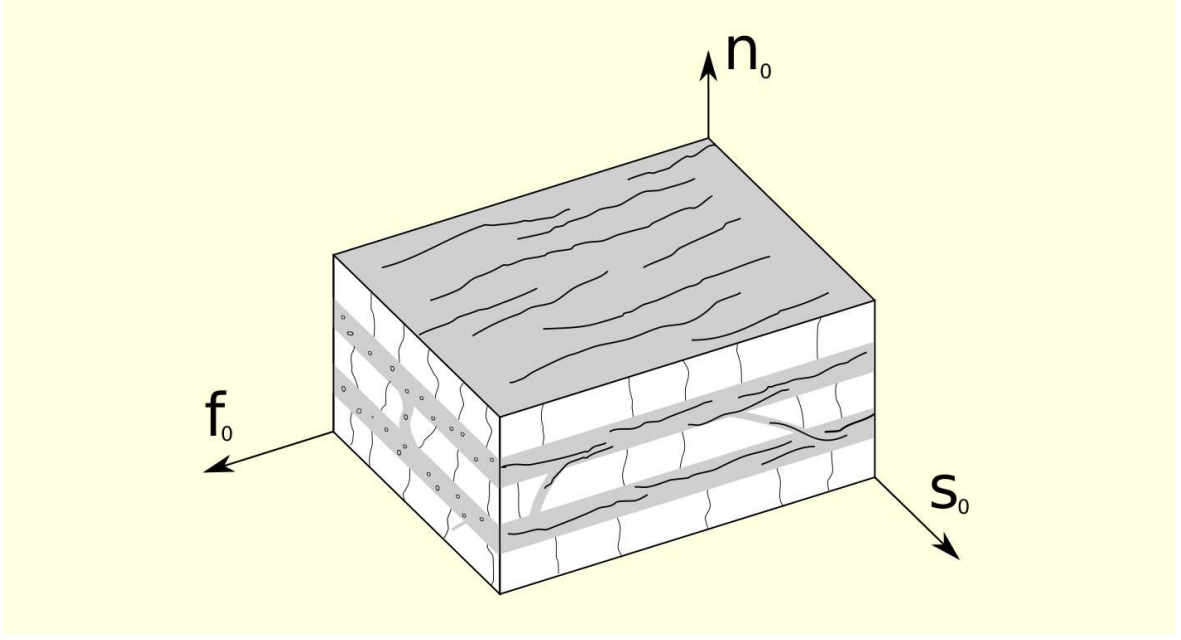
Figure 2.8: Local coordinate system. Fiber (f_0), normal (n_0) and sheet (s_0) directions are drawn.

form of the electrical propagation equation is[1]:

$$\frac{\partial V_\alpha}{\partial t} = \frac{\partial}{\partial x_i}\left(D_{ij}\frac{\partial V_\alpha}{\partial x_j}\right) + L(V_\alpha). \tag{2.3}$$

Greek subindices label the number of tissue domains. In the case of monodomain models $\alpha = 1$. For bidomain models $\alpha = 1, 2$, representing the extracellular and intracellular potentials (Simelius et al., 2001). On the right hand side of the equation two terms can be distinguished:

1) Diffusion term: It is governed by the conductivity tensor D_{ij}, which represents the conductivity in the axial and crosswise fiber direction. At a given point, a set of perpendicular unit vectors is defined: f_0 is the unit vector along the cardiac fiber at the given point, n_0 is perpendicular to the fiber in the sheet plane and s_0 is normal to the sheet plane (Fig. 2.8). The conductivity tensor D_{ij} in 2.3 is written as:

$$D_{ij} = C_{ik}^{-1}\, D_{lk}^{\text{loc}}\, C_{lj}, \tag{2.4}$$

where C_{ij} is the transformation matrix with respect to the local basis $\{f_0, n_o, s_0\}$. Expressed in the basis formed by these three vectors, the local conductivity tensor D_{lk}^{loc}

---

[1]Einstein convention on repeated indexes is used.

is diagonal:

$$\mathbf{D} = \begin{pmatrix} k_f & 0 & 0 \\ 0 & k_s & 0 \\ 0 & 0 & k_n \end{pmatrix} \tag{2.5}$$

whose diagonal components are the axial and crosswise conductivities. As reported in (Clerc, 1976; Rubart and Zipes, 2001; Coghlan et al., 2006), the conduction velocity is three times faster in the direction of the long axis of myocardial fibers than in a direction perpendicular to this long axis. Supposing the same relation, the crosswise conductivity is then one third of the axial conductivity ($k_f = 3k_n = 3k_s$).

2) Non-linear term: $L(V_\alpha)$ is the non-linear operator representing the total membrane ionic current I_{ion} and the applied stimulus I_{app}. For the I_{ion} current, different models reproduce the process of cardiac activation and deactivation. They are commonly grouped into three categories:

- *Phenomenological models.* Simplified models that use the minimum set of currents necessary to reproduce macroscopically observed behavior of cells, such as the action potential (FitzHugh, 1961; Fenton et al., 2005). These models are numerically efficient but they are not able to identify cardiac mechanisms.

- *1st generation ionic models.* They reproduce basic ionic currents and concentrations (Beeler and Reuter, 1977; Luo and Rudy, 1991).

- *2nd generation ionic models.* They give a direct description of ionic currents and concentrations and they reproduce an accurate shape of the action potential (DiFrancesco and Noble, 1985). They are robust models but numerically expensive.

The type of the ionic model I_{ion} is chosen depending on the application of the study. Simple models are suitable to simulate the pumping heart in macroscopic situations, where a detailed description of the mechanisms in the cell membrane is not necessary. On the contrary, complex ionic models are used to study cell processes. For example, pharmaceutical studies demand the modeling of the ionic exchange in the cell membrane. In this case, the evolution of the electrical wave without a detailed description of the mechanisms in the cell membrane would not be enough to capture the effect of drugs in the electrical propagation.

In this thesis, phenomenological models are used to simulate the pumping heart. The ionic models are the following:
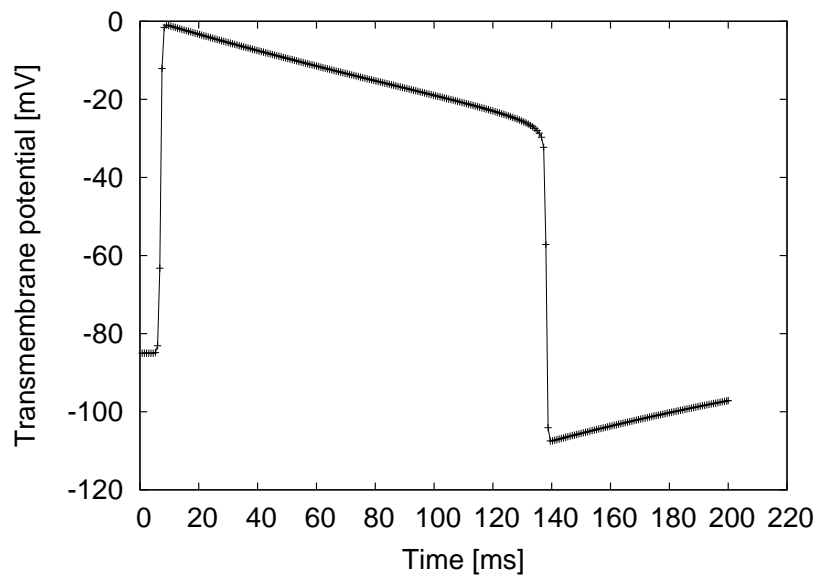
Figure 2.9: Fitzhugh-Nagumo transmembrane potential, temporal evolution for a given position.

Fitzhugh-Nagumo. Based on observations, Fitzhugh-Nagumo (FHN) is a generic model for excitable media (FitzHugh, 1961). It is a simplification of the Hodgkin-Huxley equations and does not include a physiological description of the ion exchange in the cell membrane. Although the model does not account for realistic ionic processes and concentrations, it is able to reproduce the macroscopic behaviour of excitable cells. The most general properties of the myocytes are reproduced using two variables: the transmembrane potential (V), and the recovery potential (w), which is introduced to simulate the repolarization of the cell. The equations of the model are the following:

$$\begin{aligned} I_{\text{ion}} &= c_1 V (V - c_3)(V - 1) + c_2 w \\ \frac{\partial w}{\partial t} &= \varepsilon (V - \gamma w) \end{aligned} \tag{2.6}$$

Constants c_1, c_2 and c_3 define the shape of the propagation wave and ε and γ control the recovery potential evolution. The action potential generated by the FHN model is shown in Figure 2.9. Although the shape is mathematically obtained and it is not based on cellular changes, the propagation of this electrical wave permits to investigate macroscopically how changes in the electrical activation affect the function of the muscle tissue.

Fenton-Karma. This model reproduces quantitatively much of the behavior of a full model. The Fenton-Karma model (FK) is a simple formulation which
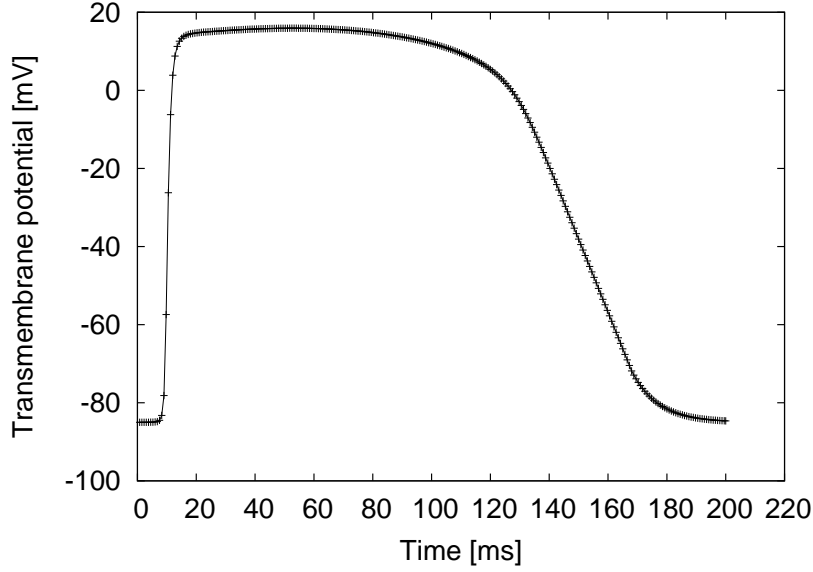
Figure 2.10: Fenton-Karma transmembrane potential, temporal evolution for a given position.

contains three ionic currents, corresponding to sodium, calcium, and potassium (Fenton and Karma, 1998). The total membrane current I_{ion} is given by the sum of the three phenomenological currents J_{fi}, J_{so} and J_{si}. The first one, J_{fi} is analogous to the Na^+ current related to the depolarization of the membrane. Secondly, J_{so} represents the K^+. Finally, J_{si} is comparable to the Ca^{2+} current, and triggers the contraction of the cardiac tissue. FK equations use three variables: the transmembrane potential V and two *ionic gates* v, w. For each current and for each ionic gate one equation is computed:

$$I_{\text{ion}} = J_{\text{fi}}(V, v) + J_{\text{so}}(V) + J_{\text{fi}}(V, w)$$

$$\frac{\partial w}{\partial t} = \Theta(V_{\text{c}} - V)\frac{(1 - w)}{\tau_w^-} - \Theta(V - V_{\text{c}})\frac{w}{\tau_w^+}$$

$$\frac{\partial v}{\partial t} = \Theta(V_{\text{c}} - V)\frac{(1 - v)}{\tau_v^-} - \Theta(V - V_{\text{c}})\frac{v}{\tau_v^+}$$

$$J_{\text{fi}}(V, v) = -\frac{v}{\tau_{\text{d}}}\Theta(V - V_{\text{c}})(1 - V)(V - V_{\text{c}})$$

$$J_{\text{so}}(V) = \frac{V}{\tau_0}\Theta(V_{\text{c}} - V) + \frac{1}{\tau_{\text{r}}}\Theta(V - V_{\text{c}})$$

$$J_{\text{si}}(V, w) = -\frac{w}{2\tau_{\text{si}}}(1 + \tanh[k(V - V_c^{\text{si}})]) \tag{2.7}$$

where Θ is the Heaviside function. Depending on the choice of the model parameters, the FK mimics Beeler-Reuter or Luo-Rudy models (Fenton and Karma, 1998). The action potential generated by the model is shown in Figure 2.10. The shape of the transmembrane potential V is obtained mathematically and reproduces a softer potential evolution than in the FHN case.

In this work, FHN and FK models are used to reproduce the most important characteristics of the action potential.

2.3   Mechanical models

The response of the cardiac tissue is characterized by a constitutive equation which gives the stress as a function of the deformation of the heart. The constitutive relations allow us to mathematically define the characteristics of the cardiac muscle.

Initially, mechanical models described the myocardium as isotropic (Demiray, 1976). Later, tests in the fibers of canine hearts showed that the myocardium has a significant anisotropy with a stiffness substantially bigger in the fiber direction than the orthogonal cross-fiber direction (Yin et al., 1987). To account for the anisotropy of the cardiac tissue, transversely isotropic models where introduced considering the same physical properties in the planes perpendicular to the fiber direction but different properties through the thickness (Humphrey et al., 1990; Guccione et al., 1991; Costa et al., 1996). This version of the law is useful when the fiber field is only characterised by its direction, with no information on their eventual sheet-like grouping. However, experimental tests performed on excised slices of cardiac muscle revealed that the tissue presents a particular orthotropic-layered architecture, meaning that the mechanical properties are different along the axis determined by the fiber orientation (Novak et al., 1994; Dokos et al., 2002). One of the first works in orthotropic constitutive models was developed by Hunter et al. (1997), containing 18 parameters in the equations. Recently, a locally orthotropic constitutive model was introduced by Holzapfel and Ogden (2009), using fiber-based material invariants.

2.3.1   Constitutive equations for the cardiac tissue

A detailed information of the orientation of the fibers is necessary to prescribe complex constitutive equations, specially orthotropic models. Since the complete orientation of the cardiac fibers is hard to obtain, transversely isotropic models are commonly

chosen to model the cardiac muscle (Watanabe et al., 2004; Dorri et al., 2006). The constitutive equations presented here are a transversally isotropic version of the orthotropic law described by Holzapfel (2000).

Governing equations.   Consider Ω_0 as a fixed reference configuration of a body and Ω the deformed one. The position vector of a particle in the body is expressed in this work by X_i in the first configuration and by x_i in the second one (note that capital letters and subscripts are used for scalars or tensors defined in the reference configuration, and lowercase letters and subscripts when defined in the deformed configuration). Being the displacement $u_i = x_i - X_I$, the relation between both measures is given by the deformation gradient:

$$F_{iJ} = \frac{\partial x_i}{\partial X_J} = \delta_{iJ} + \frac{\partial u_i}{\partial X_J} \tag{2.8}$$

In a total-Lagrangian formulation, results are referred to the initial state. The governing equations are written as:

$$\rho_o \frac{\partial^2 u_i}{\partial t^2} = \frac{\partial P_{iJ}}{\partial X_J} + \rho_o B_i \tag{2.9}$$

where ρ_o is the initial density of the body, B_i is the body force and P_{iJ} is the first Piola-Kirchoff stress tensor. Being J the determinant of the deformation gradient F, the Cauchy stress tensor is related to the first Piola-Kirchoff stress as follows:

$$\boldsymbol{\sigma} = J^{-1}\boldsymbol{P}\boldsymbol{F}^T \tag{2.10}$$

Suppose a compressible, homogeneous, hyperelastic material. The constitutive behavior of such material is expressed in terms of a strain energy function W and the right Cauchy-Green deformation $\boldsymbol{b} = \boldsymbol{F}\boldsymbol{F}^T$:

$$\boldsymbol{\sigma} = 2J^{-1}\frac{\partial W(\boldsymbol{b})}{\partial \boldsymbol{b}}\boldsymbol{b} \tag{2.11}$$

It can be useful to develop general expressions of stress in terms of the strain invariants of $\boldsymbol{b}$. The invariants are of particular interest when developing constitutive laws because they remain unchanged when expressed in a different basis. The three first invariants of $\boldsymbol{b}$ are:

$$\boldsymbol{I_1} = tr\boldsymbol{b}, \quad \boldsymbol{I_2} = \Big((tr\boldsymbol{b})^2 - tr\boldsymbol{b}^2\Big), \quad \boldsymbol{I_3} = det(\boldsymbol{b}) \tag{2.12}$$

Figure 2.8 illustrates the orthonormal basis defining the local coordinate system associated with the myocardium structure. It is assumed that the preferred direction

coincides with the muscle fiber orientations. The mean fiber orientation is represented by $\boldsymbol{f_0}$. The sheet axis that lies in plane perpendicular to the fibers is $\boldsymbol{s_0}$ and $\boldsymbol{n_0}$ is the normal to the plane formed by the two other vectors. If the material is modeled as transversally isotropic, the fourth strain invariant will be needed:

$$\boldsymbol{I_4} = \boldsymbol{f_0 b f_0} \tag{2.13}$$

Using the chain rule,

$$\frac{\partial W(\boldsymbol{b})}{\partial \boldsymbol{b}} = \sum_\alpha \frac{\partial W}{\partial I_\alpha} \frac{\partial I_\alpha}{\partial \boldsymbol{b}} \tag{2.14}$$

and the definitions of the strain invariant derivatives (Eq. 2.11) is reformulated as follows Holzapfel and Ogden (2009):

$$\boldsymbol{\sigma} = 2J^{-1}W_1\boldsymbol{b} + 2J^{-1}W_2(I_1\boldsymbol{b} - \boldsymbol{b}^2) + 2JW_3\boldsymbol{I} + 2J^{-1}W_4\overline{\boldsymbol{f}} \otimes \overline{\boldsymbol{f}} \tag{2.15}$$

where the notation $W_i = \dfrac{\partial W}{\partial I_\alpha}$ and $\overline{\boldsymbol{f}} = \boldsymbol{F f_0}$. This notation is used to underline the fact that $\overline{\boldsymbol{f}}$ is not a unitary vector. Based on physiological considerations, a form of W is suggested in Holzapfel and Ogden (2009). The energy function for the reduced transversally isotropic version presented here is given by

$$W = \frac{a}{2b}e^{b(I_1-3)} - \frac{a}{2}(I_1 - 3) + \frac{a_f}{2b_f}\left\{e^{b_f(I_4-1)^2} - 1\right\} + \frac{K}{2}(J - 1)^2 \tag{2.16}$$

The strain-energy function represents the change of the material properties during the activation. The volumetric energy term function of J have been added to make the material compressible. Introducing the expression of the derivatives of the energy in the general stress equation gives the following:

$$J\boldsymbol{\sigma}_{pas} = (a\ e^{b(I_1-3)} - a)\boldsymbol{b} + 2a_f(I_4 - 1)e^{b_f(I_4-1)^2}\overline{\boldsymbol{f}} \otimes \overline{\boldsymbol{f}} + K(J - 1)\boldsymbol{I} \tag{2.17}$$

The strain invariant I_1 represents the non-collagenous material while strain invariant I_4 represents the stiffness of the muscle fibers. The vector $\overline{\boldsymbol{f}}$ defines the fiber direction. In this equation, first term does not depend on the fiber orientation and the second term is directly referred to the fiber field. Finally, in the third term K sets the compressibility. Parameters a, b, a_f, b_f are determined experimentally in Chapter 3.

2.4   Electromechanical coupling

Electro-mechanic: Macroscopically, the excitation-contraction coupling is the phenomenon by which the fibers contract after a wave of electrical activation propagates through the myocardium. A large amount of EM coupling models have been developed (Rice and de Tombe, 2004). A 'one-way coupling' model is presented in this work, considering that the displacements have no influence on electrophysiology. The total Cauchy stress is developed in two parts, active and passive (Humphrey, 2001):

$$\boldsymbol{\sigma} = \boldsymbol{\sigma}_{pas} + \sigma_{act}(\lambda_f, [Ca^{2+}])\boldsymbol{f} \otimes \boldsymbol{f} \tag{2.18}$$

The passive part is governed by a transverse isotropic exponential strain energy function $W(\boldsymbol{b})$, defined in Equation 2.16. The active part is calculated as in Holzapfel (2004). It is assumed to be produced in the direction of the fiber. If the muscle fiber stretch is represented by λ_f, the excitation-contraction coupling is modeled as follows:

$$\sigma_{act} = \gamma \, \frac{[Ca^{2+}]^n}{[Ca^{2+}]^n + C_{50}^n} \sigma_{max}(1 + \beta(\lambda_f - 1)) \tag{2.19}$$

In this equation, C_{50}^n, σ_{max} and β are model parameters. The coupling parameter γ is used to graduate the active stress ($0 < \gamma < 1$). The concentration $[Ca^{2+}]$ mediates the contraction of the myocardium and fluctuates in time following this relation (Hunter et al., 1998):

$$[Ca^{2+}](t_{loc}) = [Ca^{2+}]_{max}(t_{loc}/\tau_{Ca})e^{(1-t_{loc}/\tau_{Ca})} \tag{2.20}$$

where τ_{Ca} is a parameter and t_{loc} is the local activation time. The t_{loc} is initiate to 0 s at the beginning of the simulation for the entire mesh. When the membrane potential overcomes a threshold value (fixed to -5 mV), EM coupling is triggered and t_{loc} starts running at this specific location. Then, $[Ca^{2+}]$ (and consequently σ_{act}) also vary.

Figure 2.11 shows the relation between the local activation time and the action potential, the concentration of intracellular $[Ca^{2+}]$ and the normalized active force produced. Parameter values are $C_{50}^n = 0.5\mu m$, $\sigma_{max} = 100kPa$, $\beta = 2.5, [Ca^{2+}]_{max} = 1.0\mu m$, $n = 3$ and $\tau_{Ca} = 0.06s$. In this problem, the electrical propagation is solved using a monodomain model and a FHN ionic current model. The electrical conductivity is isotropic, equal to 0.012 ms/cm and the membrane capacitance is $C_m = 0.001\mu F/cm^2$.
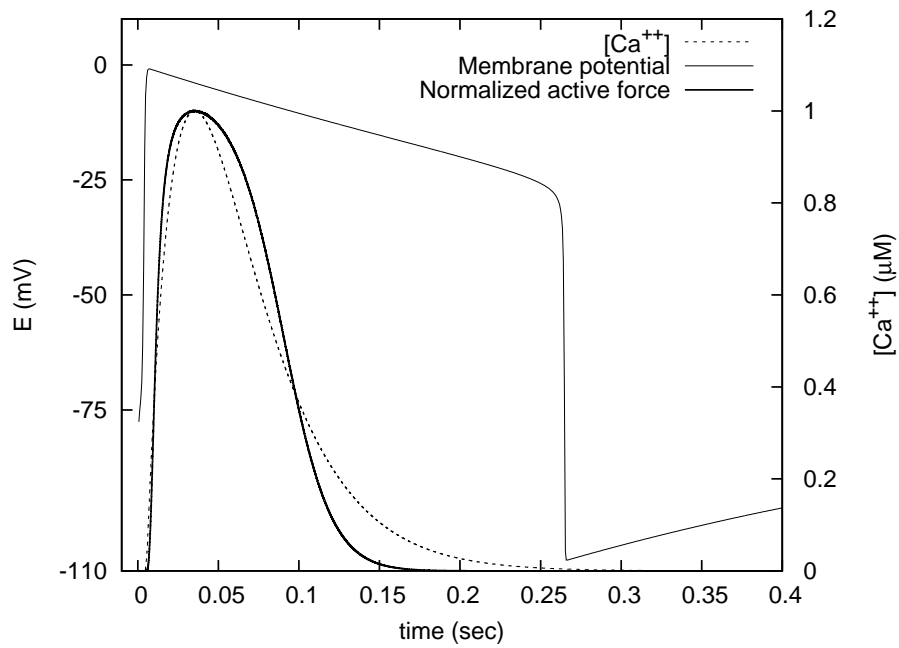
Figure 2.11: Time scale comparison of the normalized active force, the membrane potential and the $[Ca^{2+}]$.

Mechano-electric: The algorithms of continuum mechanics usually make use of two classical descriptions of motion: the Lagrangian description and the Eulerian description (Donea et al., 2004). In a Lagrangian description, the computational mesh follows the movement of the body. Each node of the mesh coincides with the associated material particle during motion. In the Eulerian description, the computational mesh is fixed and the body moves with respect to the grid.

In this work, the mechano-electric coupling follows the Lagrangian description. Therefore, the action potential propagates in the deformed configuration.

Chapter 3

HPC cardiac computational modeling

Working at the organ-level, the cardiac computational model requires solution of three components: the electrical signal, the mechanical deformation and the excitation-contraction coupling that links both problems together. The equations of the complex models describing the heart can not be solved analytically, they must be solved on a computer using numerical techniques.

The main topic of this chapter is the solution of the governing equations to simulate the electromechanical propagation of the heart. The methods are based on a finite element approach (FEM), focusing on the solution in parallel computers. The time evolution of the system is calculated using an Euler scheme. We also present and analyze two different integration rules in the right hand side of the equation that solves the problem, with and without mass lumping. We underline the most remarkable differences between them.

Finally, the computational code *Alya* is presented. The tool is used in this thesis to run cardiac simulations, solving both cardiac electrophysiology and mechanics. Alya is conceived as a multiphysics platform to deal with coupled computational problems in parallel, designed from scratch to take profit of parallel architectures with parallel efficiency.
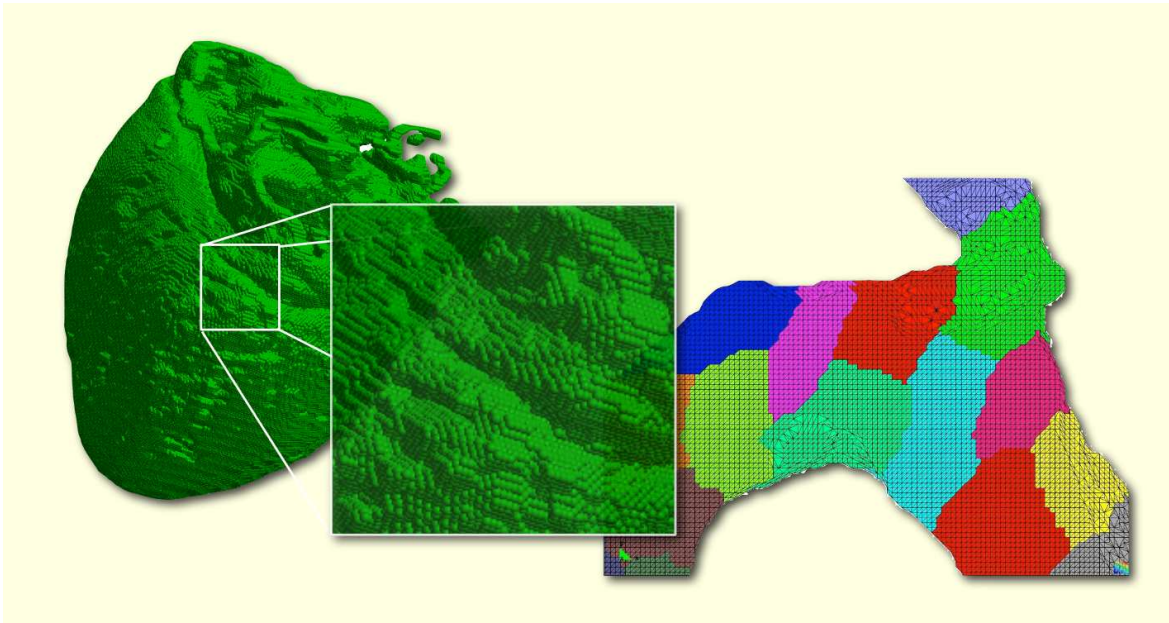
Figure 3.1: Canine ventricular data, Johns Hopkins University. MRI data is processed to obtain the computational mesh. Green dots correspond to the voxels obtained from the image. The geometry is discretized in tetrahedral elements, using the mesh generator Tetgen. A slice of the ventricular mesh is represented in colours.

3.1 The computational domain

To solve the electromechanical problem, the typical domain in this project is a 3D cardiac geometry consisting in two ventricles. Figure 3.1 shows an anatomically detailed MRI-derived canine ventricular model developed by Johns Hopkins University. The continuous volume, extracted from cardiac images, is divided into small elements and the governing equations are numerically solved within these elements. In 3D, the FEM-based space discretization allows different element types to solve the governing equations. Particularly, the cardiac geometry can be divided in tetrahedral or hexahedral elements. After some tests, tetrahedra have been chosen to solve the large-scale problems in this work because they fit anatomical information obtained from clinical images. Given the increasing resolution and accuracy of cardiac imaging, unstructured tetrahedral meshes can be easily adapted to complex geometries and can be efficiently generated from raw data.

This work uses the same mesh for the coupled problem, solving both electrical and mechanical equations in the same discretized domain. We present the electrophysiological and mechanical equations that are solved in the cardiac geometry.

3.2 Computing the electrical activity

Cardiac electrophysiology is modeled here at the organ level. Considering a monodomain scheme, the parabolic reaction diffusion equation can be written as follows:

$$C_m \frac{\partial V}{\partial t} = \frac{\partial}{\partial x_i} \left(\frac{D_{ij}}{S_v} \frac{\partial V}{\partial x_j} \right) + L(V), \tag{3.1}$$

where C_m is the membrane capacitance ($\mu F\,cm^{-2}$) and S_v is the surface to volume ratio. The non linear term $L(V)$ represents the total membrane ionic current is I_{ion} and the applied stimulus I_{app} ($\mu A\,cm^{-2}$).

To find the value of the action potential V, the discretization of the partial differential equations is carried out using a variational formulation (Johnson, 1987). Assuming that the solution V belongs to the the usual FEM interpolation function space $\mathcal{V}$, the test function $\psi \in \mathcal{V}$ is chosen (Eriksson et al., 1996). The simulation domain is Ω and its boundary is $\partial\Omega$. The weak form of Equation 3.1 is obtained by first multiplying by ψ and then integrating over the domain Ω. Three terms can be distinguished in this equation:

$$\underbrace{\int_{\Omega} \psi \frac{\partial V}{\partial t}\, d\Omega}_{\text{Mass term}} = \underbrace{\int_{\Omega} \psi \ \frac{\partial}{\partial x_i} \left(\frac{D_{ij}}{C_m S_v} \frac{\partial V}{\partial x_j} \right) d\Omega}_{\text{Difussion term}} + \underbrace{\frac{1}{C_m} \int_{\Omega} \psi L(V)\, d\Omega}_{\text{Non-Linear term}} \tag{3.2}$$

1) Mass term: Corresponds to the time derivative term.

2) Diffusion term: Using the chain rule and the Gauss's theorem, the diffusion term gives:

$$\int_{\partial\Omega} \psi \ \frac{D_{ij}}{C_m S_v} \ \frac{\partial V}{\partial x_j}\, n_j dS - \int_{\Omega} \frac{D_{ij}}{C_m S_v} \ \frac{\partial \psi}{\partial x_i} \frac{\partial V}{\partial x_j}\, d\Omega \tag{3.3}$$

The first part of the diffusion term is used to impose Neumann boundary conditions. To a first approximation, the fluxes on the boundaries are set to zero, and this part vanishes. No Dirichlet conditions are directly imposed.

3) Non-linear term: Corresponds to the ionic current. For the FHN model, an ordinary differential equation (ODE) is added to simulate the gate potential w.

Linearizing the ionic equation, $L(V)$ can be expressed as:

$$
\begin{aligned}
L(V) &= c_1 V (V - c_3)(V - 1) + c_2 \equiv V f(V) \\
\frac{\partial w}{\partial t} &= \varepsilon (V - \gamma w)
\end{aligned}
\tag{3.4}
$$

Rewriting the three terms in the weak form, the system to be solved is:

$$
\begin{aligned}
\int_\Omega \psi \, \frac{\partial V}{\partial t} \, d\Omega &= - \int_\Omega \frac{D_{ij}}{C_m S_v} \, \frac{\partial \psi}{\partial x_i} \frac{\partial V}{\partial x_j} \, d\Omega + \frac{1}{C_m} \int_\Omega \psi \, V f(V) \, d\Omega \\
\frac{\partial w}{\partial t} &= \varepsilon (V - \gamma w)
\end{aligned}
\tag{3.5}
$$

Discretization in space.   The spatial discretization of Equation 3.5 is performed using a FEM approach. The solution V and its derivative are expressed as:

$$
\begin{aligned}
V(x,t) &= \sum_{k=1}^{n_{nodes}} \psi_k(x) V_k(t) \\
\dot{V}(x,t) &= \sum_{k=1}^{n_{nodes}} \psi_k(x) \dot{V}_k(t)
\end{aligned}
\tag{3.6}
$$

Introducing these expressions, the Equation 3.2 yields:

$$
\dot{V} \int_\Omega \psi_i \psi_j \, d\Omega = -V \int_\Omega \frac{\partial \psi_i}{\partial x_i} \frac{D_{ij}}{C_m S_v} \frac{\partial \psi_j}{\partial x_j} \, d\Omega + V f(V) \frac{1}{C_m} \int_\Omega \psi_i \psi_j \, d\Omega
\tag{3.7}
$$

After discretization, Equation 3.5 can be expressed in a matrix form:

$$
\begin{aligned}
\boldsymbol{M}\dot{\boldsymbol{V}} &= -\boldsymbol{K}\boldsymbol{V} + \boldsymbol{M}\boldsymbol{V} f(\boldsymbol{V}) \\
\dot{\boldsymbol{W}} &= \varepsilon (\boldsymbol{V} - \gamma \boldsymbol{W})
\end{aligned}
\tag{3.8}
$$

The FEM-based formulation leads to a mass matrix $\boldsymbol{M}$ in the time derivative term, a diffusion matrix $\boldsymbol{K}$, with anisotropic diffusion tensor, and a non-linear ODE-like term for the I_{Ion} current.

Discretization in time.   The explicit formulation is particularly well-suited for solving the non-linear equations of the electrophysiological problems, which need very short time-scales. In particular, the explicit scheme is chosen because the non-linear term permits this formulation. Although FHN equations can also be solved implicitly,
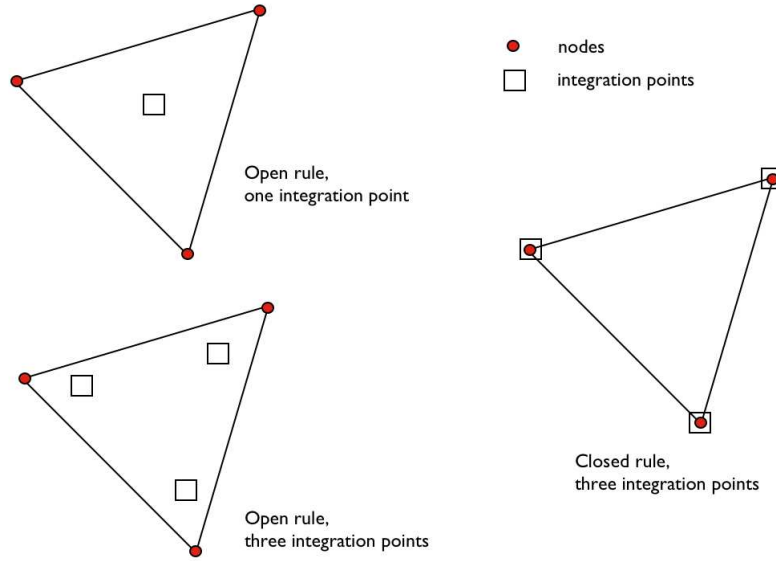
Figure 3.2: Integration rules for triangles. Open rules with one or three integration points and one closed rule with three integration points.

other complex models would permit the implicit solution just in the diffusion term, not in the non-linear term Ten-Tusscher and Panfilov (2006).

The temporal discretization of the equation is performed using the FD method. Then, the derivatives of V and W are expressed as:

$$
\begin{aligned}
\dot{V} &= \frac{V^{n+1} - V^n}{\Delta t} \\
\dot{W} &= \frac{W^{n+1} - W^n}{\Delta t}
\end{aligned}
\tag{3.9}
$$

where Δt is the time step, V^n is the solution at the current step and V^{n+1} is the solution at the new time step. Using an explicit Euler scheme, the matrix form yields:

$$
\begin{aligned}
\frac{\boldsymbol{M}}{\Delta t} \boldsymbol{V^{n+1}} &= \boldsymbol{M} \left(\frac{1}{\Delta t} + f(\boldsymbol{V^n}) \right) \boldsymbol{V^n} + \boldsymbol{K} \boldsymbol{V^n} \\
\boldsymbol{W^{n+1}} &= \boldsymbol{W^n} + \Delta t \left(\boldsymbol{V^{n+1}} + \gamma \boldsymbol{W^n} \right)
\end{aligned}
\tag{3.10}
$$

In the time derivative term $\boldsymbol{M}$ must be inverted. To solve this problem, two different numerical integrations can be applied:
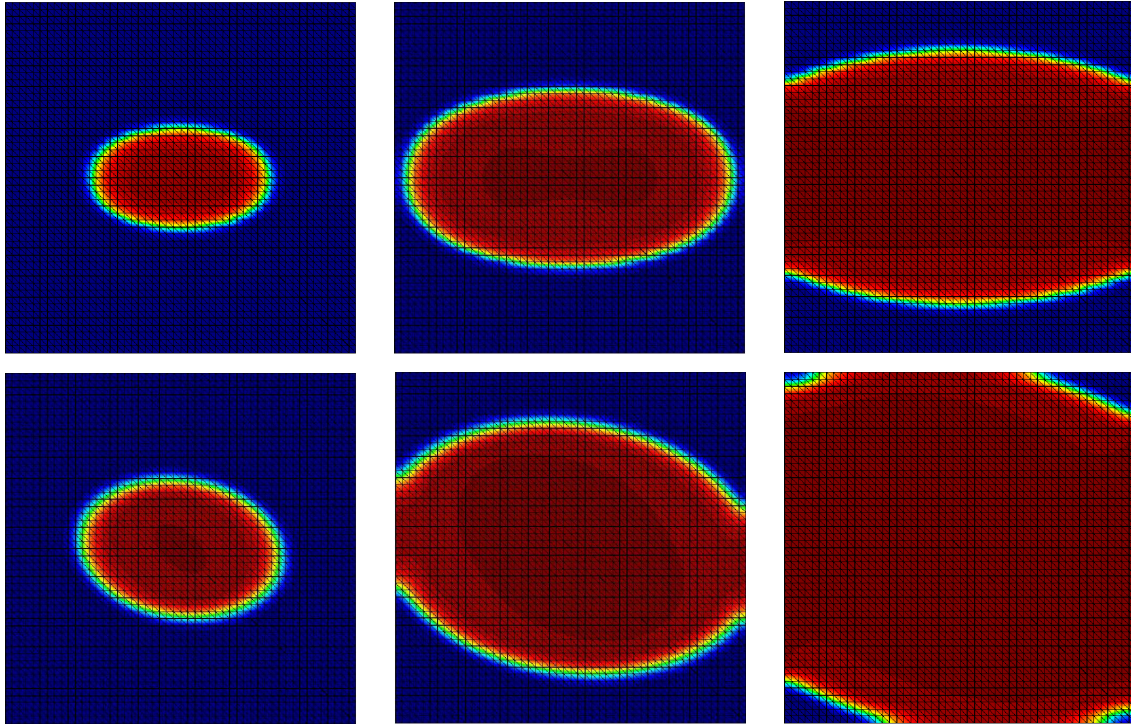
Figure 3.3: Anisotropic 2D potential propagation sequences: closed integration rule for the ODE-like term (top) versus open integration rule for the ODE-like term (bottom). The first option gives the proper shape and propagation speed.

- The *open* rule, where the integration points are not coincident with the nodes. In this case, M is called consistent matrix and is not diagonal. A special treatment of the rows is performed to diagonalize it.

- The *closed* rule, where the integration points are coincident with the nodes. M is called lumped matrix and is diagonal. Nodal locality is preserved because shape functions are built by setting them to one in its own node and zero in the rest of them.

Mass lumping is a numerical technique related to the FEM that has been widely used in different applications. Figure 3.2 shows three integration cases for triangles, where the open and closed rules are used.

To compare the results of the open and closed numerical integrations, the electrical propagation equations are solved in a 2D anisotropic media, with cardiac fibers oriented in horizontal direction (Fig. 3.3). FHN model is used to simulate the evolution of the action potential through the cardiac tissue. In this simulation, conductivities in Cartesian axes are chosen proportional ($k_x = 3k_y$). The figure shows a sequence of the propagation in both cases, computing the consistent and lumped matrices to integrate
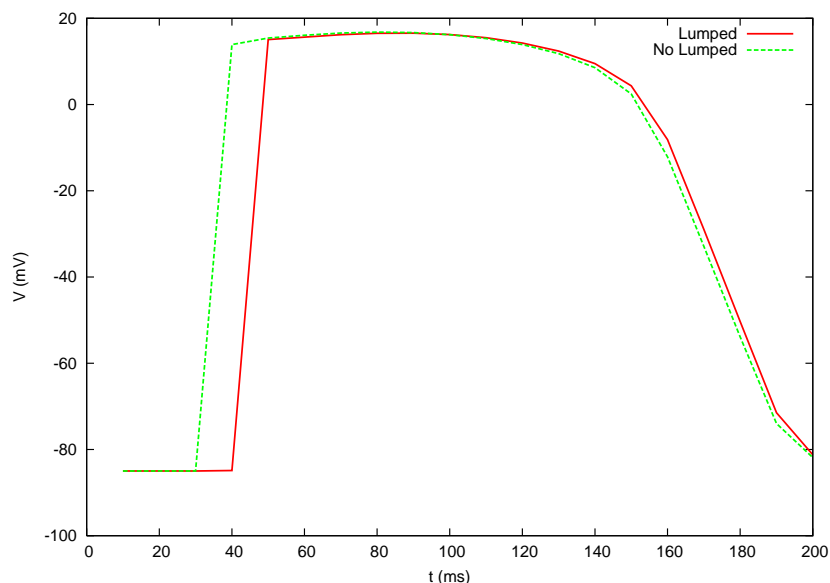
Figure 3.4: Action potential with open and closed integration rules: speed differences for the closed rule ("lumped") and the open rule ("no-lumped") used in the ODE-like term.

the non-linear term in the ODE. Top row corresponds to lumped or closed integration rule and bottom row corresponds to the consistent or open rule. The use of the open rule introduces a significant error in speed and propagation behavior. The difference in speed between the two models can be observed in Figure 3.4. The open rule (green curve, called "no lumped") produces a propagation that arrives earlier than the closed rule (red curve, called "lumped"). Apparently, consistent matrix leads to higher cross-diffusion.

Finally, Figure 3.5 shows the results when the diffusion term is set to zero. In case of no diffusion, the action potential should not propagate through the cardiac tissue. If the governing equations are integrated using the open rule, an artificial numerical diffusion is introduced producing a wrong propagating behavior . On the contrary, when the closed rule is chosen, the initial condition does not propagate, as expected.

Critical time step.   The typical procedure to solve transient problems explicitly is to compute a local time step at each mesh element using its characteristic size h and take the minimum value to obtain the global time step. In the explicit case, the critical time step Δt_{crit} that corresponds to the electrophysiological governing equations should be calculated taking into account the diffusion and the non-linear term. Through numerical experiments, we observed that the most stringent criterion comes from the diffusion part. Independently of the cell model, the critical time step is calculated as
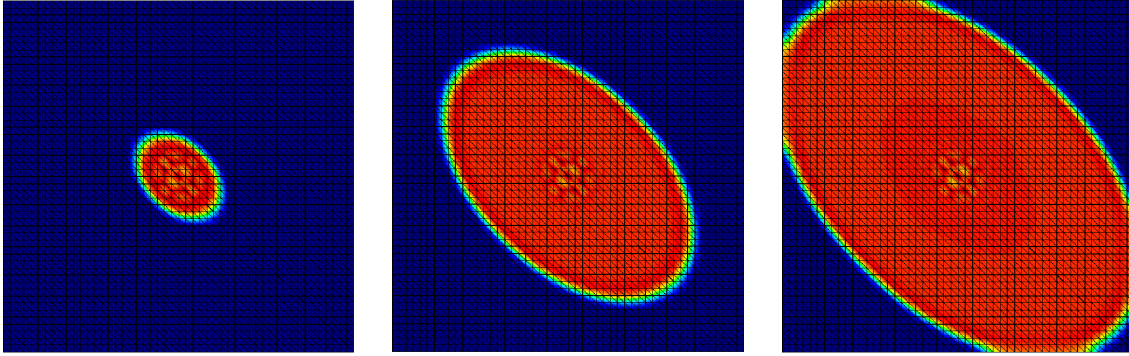
Figure 3.5: Anisotropic 2D potential propagation sequences: when diffusion is set to zero, the open rule introduces an artificial numerical diffusion, producing a wrong propagating behaviour.

follows:

$$\Delta t = \frac{h^2}{2D} \tag{3.11}$$

where h is the characteristic size of the element and D is the largest entry of the diffusion tensor, usually along the fiber. At every time step, Δt is computed for each element of the computational domain. The lowest value is taken as the global time step and used for the explicit time advance.

3.2.1   Simulation in a biventricular geometry

In this section we present an example that shows the potential of the proposed methodology for simulating the electrophysiological problem in realistic cases. This work is done in collaboration with Centre de Visio per Computador (CVC), in Bellaterra (Spain).

We use real data obtained from medical images. The ventricles are the result of a mean model of healthy canine hearts from a study at Johns Hopkins University, which is freely available at http://www.ccbm.jhu.edu/. Firstly, the MR-DTI data is converted to usable file. The external anatomy of the myocardium is described as a field of points regularly distributed, with a mean resolution of 0.2 mm, corresponding to the voxels obtained from the image. The fiber orientation is given as a vector at each coordinate point. Secondly, the geometrical information is converted into a computational mesh, using the software Tetgen. Figure 3.1 shows the input data set and a slice of the resultant mesh. The mesh is made of 17M tetrahedra, maintaining the image resolution.

Finally, electrophysiological simulations are run in Marenostrum supercomputer in parallel. Results are obtained in 15 minutes of wall clock time using 500 cores. The
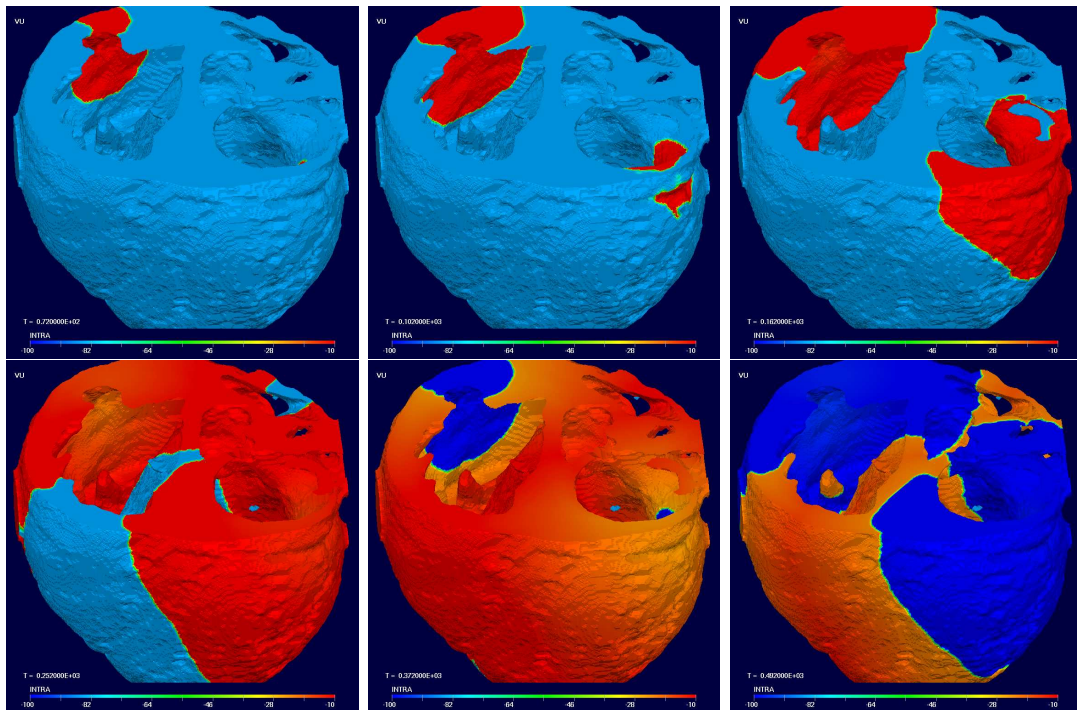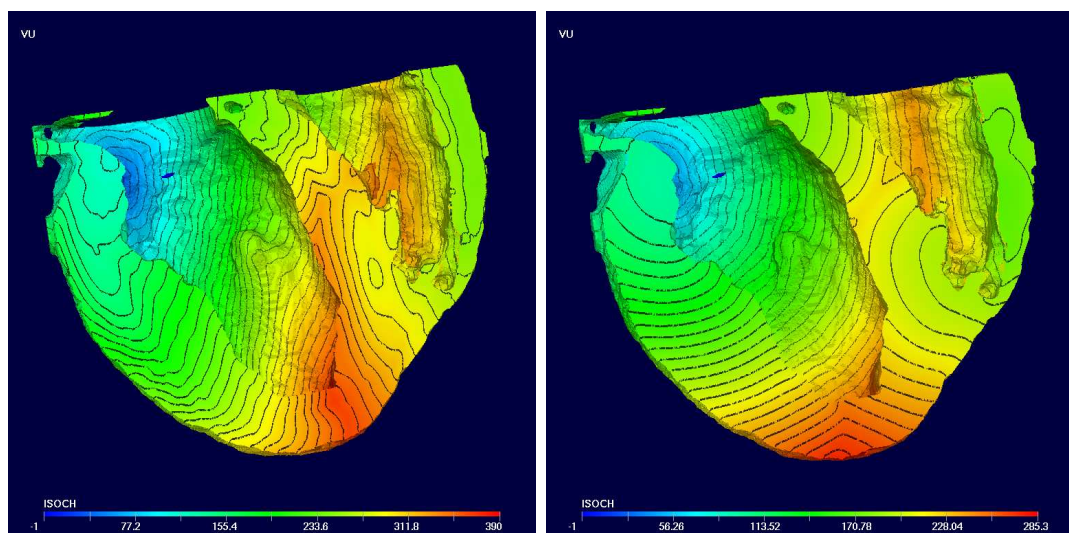
Figure 3.6: Action potential propagation.

Figure 3.7: The isotropic model is represented on the left and the anisotropic case on the right. Isochrones are packed in the septum, due to the fiber conduction action.

initial condition that activates the ventricles is chosen from experimental evidence (Ballester-Rodes et al., 2006). Two stimuli spread from the base to the apex with a delay of 30 ms between them. In Figure 3.6, six snapshots represent the evolution of the action potential through the cardiac tissue at different times.

Moreover, isotropic and anisotropic conductivities are tested in the framework. Figure 3.7 shows the isochrones in both cases. Notice that the isochrones became much tighter packed in the septum, due to the fiber conduction action.

This work is introductory to a wider Computational Biomechanics strategy, attacking the problem of simulating the heart behaviour from the standpoint of a Computational Mechanics researcher. The experience acquired in electrophysiology and the background in HPC techniques allows us to write a parallel code specific for this problem and adapted to run efficiently in a supercomputer.

3.3 Computing the mechanical contraction

The governing equation that describes the mechanical deformation in the cardiac tissue is the following:

$$\rho_o \frac{\partial^2 u_i}{\partial t^2} = \frac{\partial P_{iJ}}{\partial X_J} + \rho_o B_i \tag{3.12}$$

Assuming that the solution u belongs to the the usual FEM trial and interpolation function space $\mathcal{W}$, the test function $\phi \in \mathcal{W}$ is chosen. Then, the weak form in the fixed reference configuration Ω_0 is:

$$\int_{\Omega_0} \phi \rho_o \frac{\partial^2 u_i}{\partial t^2} \, d\Omega_0 = - \int_{\Omega_0} \frac{\partial \phi}{\partial x_J} P_{iJ} \, d\Omega_0 + \int_{\partial \Omega_0} N_J P_{iJ} \phi \, d\Omega_0 + \int_{\Omega_0} \phi \rho_o B_i \, d\Omega_0 \tag{3.13}$$

where ρ_o is the initial density of the body, N_J is the exterior normal of Ω_0 on the surface $\partial \Omega_0$, B_i is the body force and P_{iJ} is the first Piola-Kirchhoff stress tensor. As in the electrophysiological case, space is discretized using the FEM and time is discretized with FD. The discretization of the equations leads to a matrix equation of the form:

$$\boldsymbol{M}\ddot{\boldsymbol{u}} + \boldsymbol{C}(\boldsymbol{u})\dot{\boldsymbol{u}} + \boldsymbol{K}(\boldsymbol{u})\boldsymbol{u} = \boldsymbol{F} \tag{3.14}$$

where $\boldsymbol{F}$ is the force vector, $\boldsymbol{M}$ is the mass matrix and $\boldsymbol{K}$ is the stiffness matrix, which typically depends on the unknown. The second term, proportional to the speed, is called Rayleigh damping, where $\boldsymbol{C}(\boldsymbol{u})$ is the damping matrix. This matrix is added

to damp high frequencies and avoid unphysical oscillations. Usually, it is written as $\boldsymbol{C}(\boldsymbol{u}) = \alpha\boldsymbol{M} + \beta\boldsymbol{K}(\boldsymbol{u})$, where parameters α and β are computed depending on the frequency range to be damped (Belytschko et al., 2000). After some numerical experiments, we have observed that the best choice is to take $\beta = 0$ and $\alpha = c\nu$, where c is a constant between 2 and 10. The frequency ν is computed by running a problem without damping, plotting the displacement for one point in the domain and analyzing its time series. It is worth to remark that when $\beta = 0$ the matrix damping becomes independent of the unknown, which certainly simplifies its computation.

Critical time step. As in the electrophysiological case, the local time step is computed at each mesh element using its characteristic size h. The minimum value is taken to obtain the global time step. For the solid mechanics problem, Δt_{crit} is related directly to the element size and inversely to the information propagation speed. The usual procedure is to compute the local time step using the speed of sound (Belytschko et al., 2000). For each element, Δt is computed at every time step. The explicit time advance is performed choosing the lowest value in the domain.

3.3.1 Characterization of the passive stress

In this section, parameters a, b, a_f, b_f of the passive stress are determined experimentally reproducing the test bi-axial test conducted by Yin et al. (1987)[1].

Passive stresses have been studied intensely in the past; they are typically determined through in-vitro experiments of explanted tissue. A thin square sheet of tissue of about 4 cm × 4 cm × 0.15 cm is extracted from the myocardium. The traction axis are aligned with the fiber (f) and sheet direction (s). The third direction perpendicular to this plane is called the normal direction (n) (Fig. 2.8). First, the stress equation (Eq. 2.17) is solved numerically using the gradient deformation tensor $\boldsymbol{F} = diag[\lambda_f\ \lambda_s\ \lambda_n]$. The subscripts refer to the directions described above and λ is the stretch in the indicated direction. λ_f and λ_s are given (supposing a displacement-controlled test) and λ_n is found solving:

$$\sigma_n = (ae^{(b(I_1-3))} - a)\lambda_n^2 + K(J-1) = 0 \qquad (3.15)$$

since no constraint are applied in this direction. This equation is solved numerically using the bisection method. The stress in the two other directions are then calculated

---

[1]This section has been written in collaboration with P. Lafortune and Antoine Jerusalem (Lafortune et al., 2012)
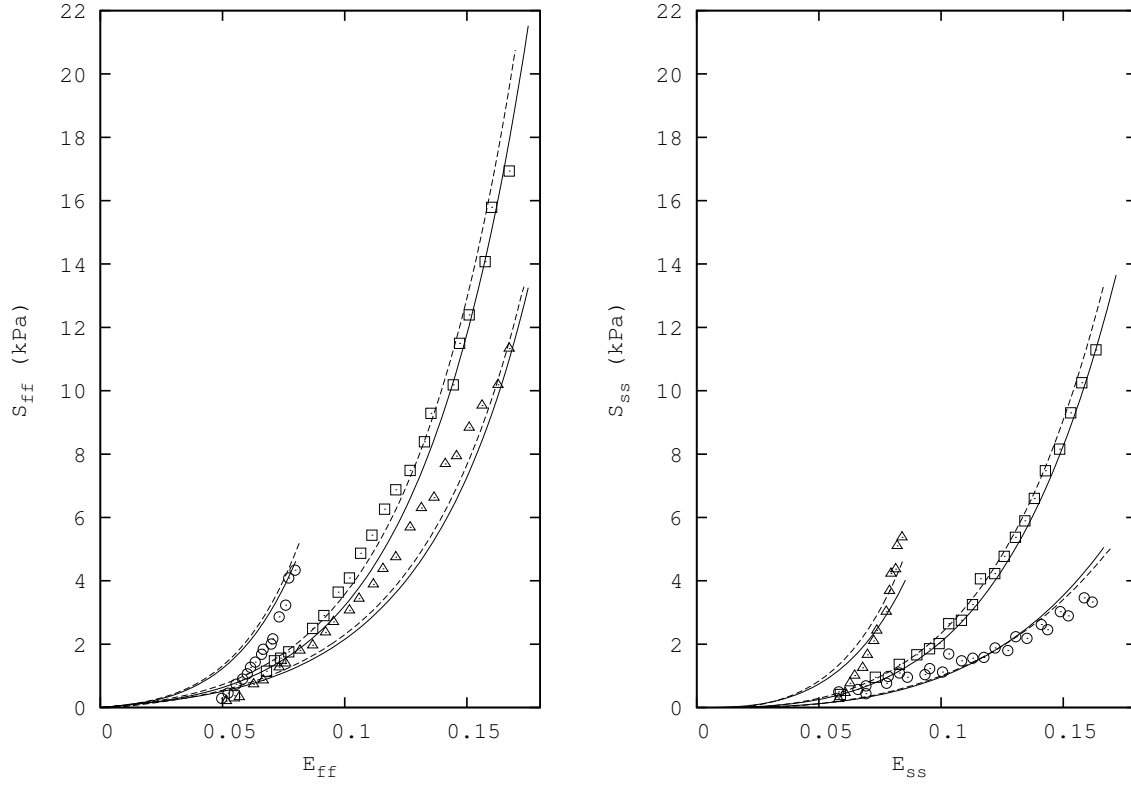
Figure 3.8: Bi-axial test. Experimental values extracted from Yin et al. (1987) for strain ratio E_{ff}/E_{ss} of 0.48 ($\bigcirc$), 1.02 ($\square$) and 2.05 ($\triangle$). The full curves represent the solution of the analytical solution and the dash curves the values obtained with the FEM.

with:

$$\sigma_f = (ae^{(b(I_1-3))} - a)\lambda_f^2 + 2a_f(I_4 - 1)e^{b_f(I_4-1)^2}\lambda_f^2 + K(J - 1) \tag{3.16}$$

$$\sigma_s = (ae^{(b(I_1-3))} - a)\lambda_s^2 + K(J - 1) \tag{3.17}$$

where the constant values are $a = 4.3$ kPa, $b = 9.7$, $a_f = 1.69$ kPa, $b_f = 15.78$. In addition to the numerical solution used to find the parameters, the model is tested reproducing the bi-axial tests with a simple FEM model containing 50 linear hexahedral elements. The results of those tests, along with experimental data, are shown in Figure 3.8.

To characterize the material in compression we can have a general idea using the solution of a uni-axial traction test. The deformation gradient tensor is in this case simplifies to $\boldsymbol{F} = diag[\lambda_f \; \lambda_s \; \lambda_s]$, where f is the fiber direction align with the traction, and s the two other directions forming a perpendicular plan to f. Once again, we suppose here that λ_f is the displacement of the traction machine, and we find λ_s
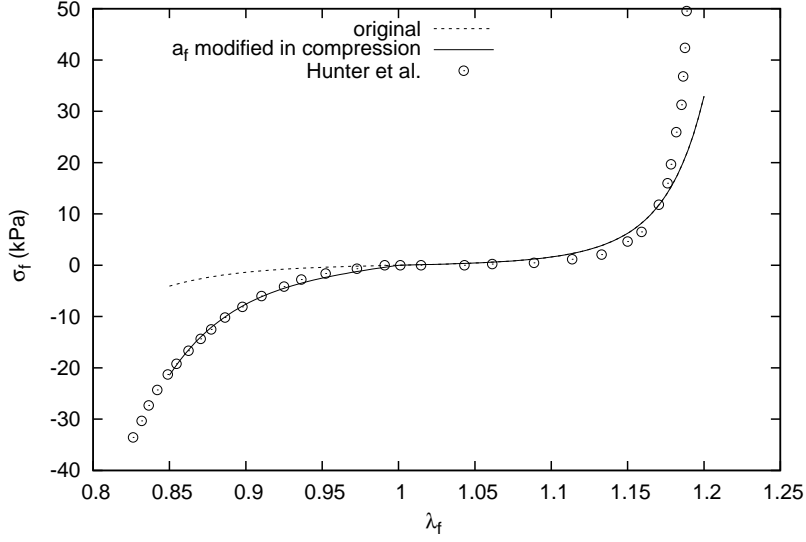
Figure 3.9: Solution of the stress equations for a uni-axial tension-compression test. The response given by the original parameters and when the value of a_f is modified are shown. Values published by Hunter et al. (1997) are also shown.

solving the stress equation in the s directions:

$$\sigma_s = \left(ae^{(b(I_1-3))} - a\right)(\lambda_s^2) + K(J-1) = 0 \tag{3.18}$$

Then, the stress in the f direction can be computed as

$$\sigma_f = \left(ae^{(b(I_1-3))} - a\right)(\lambda_f^2) + 2a_f(I_4-1)e^{b_f(I_4-1)^2}\lambda_f^2 + K(J-1) \tag{3.19}$$

Figure 3.9 shows the result of the uni-axial traction test. First, the behavior of the material with the parameters previously found is plotted. A very low stiffness is observed in compression, due the nature of the exponential functions used in the constitutive equation. To stiffen the material in compression, the constant a_f is increased to $a_f^{comp} = 6.5\, a_f$ when compression is detected in the direction of the fibers ($\lambda_f < 1.0$). The result using the modified coefficient is plotted on the same graphic. Even if acting on the term that controlled the fibers, this modification must be seen as acting on the whole structure. As mentioned by Holzapfel and Ogden (2009), the fibers are most likely to buckle when compressed, and then have a minor contribution.

3.4   Alya

In this thesis, the governing equations of the electrical propagation and the mechanical deformation of the heart are numerically solved in the same code Alya. The code is developed and supported at Barcelona Supercomputing Center (Houzeaux et al., 2013, 2009).

Alya is written in Fortran 90/95. It solves time-dependent PDEs, using a numerical method. Variational formulations and the FEM are preferred but other discretization methods can be easily programmed. Time advance is numerically integrated by FD with trapezoidal rules. Monolithic implicit, by-block segregated or explicit schemes are used.

The platform is designed to be multiphysics and flexible for running in parallel coupled problems using non-structured meshes. Different physical phenomena are solved using the code, such as fluids, meteorology, electromagnetic waves or the EM propagation in the heart (Puzyrev et al., 2013; Marras et al., 2013; Vázquez et al., 2011).

For the coupled EM problem, the code targets the following aspects:

- Large geometries: data coming from high definition acquisition producing high resolution meshes in both electrical and mechanical problems.

- Complex physiological models: electrophysiological, material and coupling models of high complexity, with thousands of degrees of freedom per node.

- Multi-physics problems: electrical activity, mechanical deformation and blood flow.

3.4.1   Code modularity

Alya architecture is modular. It is composed by modules, services and kernel. The modules solve numerically each of the individual physical problems. The services provide a set of complementary tools, called by modules and kernel, for example the parallelization. Finally, the kernel contains the core of Alya where the common procedures lie.

For the EM case, the governing equations of the electrophysiological problem have been computed in a module called *exmedi* and the mechanical equations have been computed separately, in a module called *solidz*. Figure 3.10 shows the modular structure
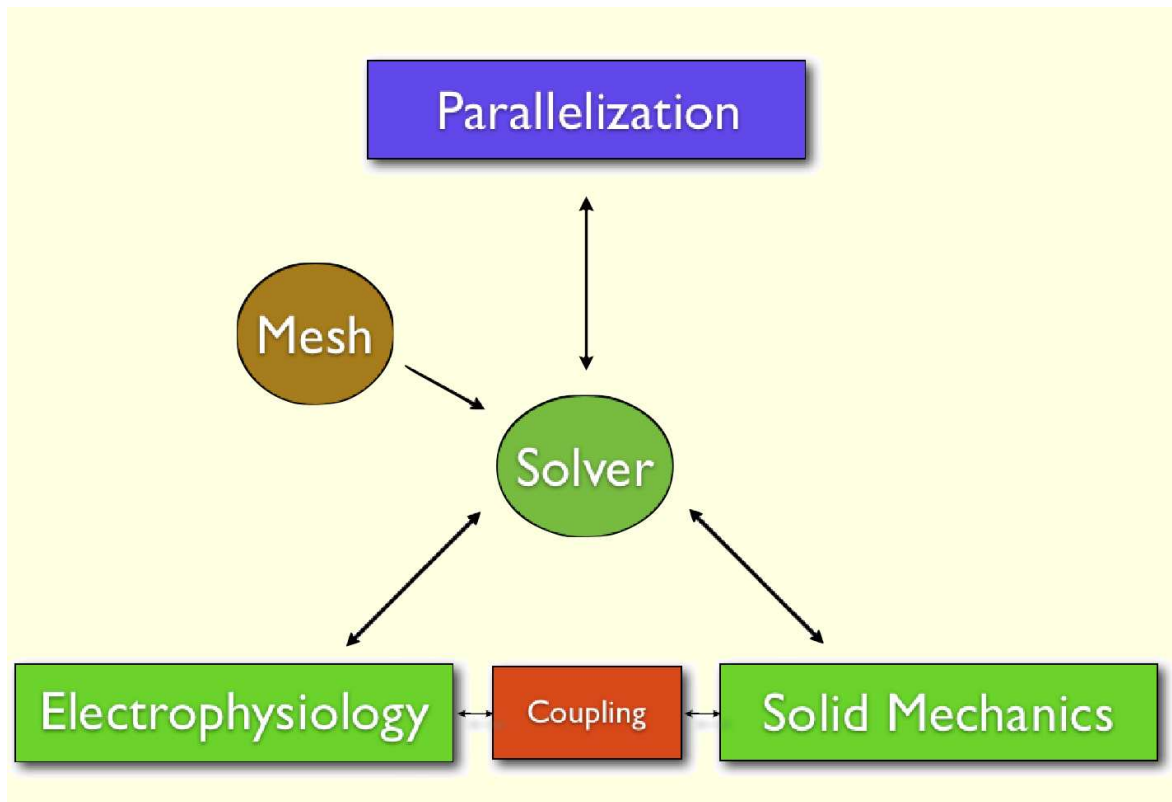
Figure 3.10: Modular structure in Alya.

Do time loop

- Compute the equations of the electrical system (module *exmedi*)

- Compute the coupling factor

- If the coupling factor reaches a threshold

    - Compute the equations of the mechanical system (module *solidz*)

- End If

End Do

Table 3.1: General algorithm to solve the EM problem in Alya.

of the EM system. In this coupled problem, one unique tetrahedral mesh is used to solve the discretized governing equations. Every time step, the problems are solved in a staggered way, using a by-block structure, involving one alternate solution of electrical and mechanical modules. The kernel is in charge of reading data and geometry, computing the mesh, calling the modules or calling the parallelization service. The general algorithm is presented in Table 3.1.

Global time step. Due to the highly transient character, electrical and mechanical problems are solved explicitly, computing the time step in the electrical and the mechanical modules separately. Based on stability criteria, the global time step is the smallest one computed for each of the two modules. The same time step allows a straight synchronization. After many numerical experiments we have found that the electrophysiology time step is around 50% smaller than the mechanical one ($\Delta t = 10^{-6}s$). The accuracy and computational times required in the EM solution are often related by the degree of mesh refinement. For the coupled problem, the mechanical system is highly non-linear and the time to solve it is greater than the electrical system on the same mesh.

Parallelization. Thanks to the code modularity, the electrophysiological and mechanical governing equations are computed in separate modules sequentially and the parallelization is performed external. Work distribution is achieved by sub-division of the original sequential problem in smaller problems running concurrently. Problem sub-division is done using METIS, an automatized mesh partitioner which divides the original mesh in sub-domains and distributing work among the cores (Fig. 3.11). The solver, based on MPI communication, gives at every moment the same result running in parallel with many partitions as running sequentially with a unique partition. The local element matrices are built following the sequence:

1. For each slave, compute elemental LHS and RHS.

2. For each slave, assemble (scatter) elemental RHS and LHS into global LHS and RHS.

3. Exchange RHS of boundary nodes, the nodes belonging to more than one sub-domain and sum up the contribution.

4. The operations of an iterative solver are matrix-vector multiplications. Then, for each slave, compute matrix-vector multiplication.
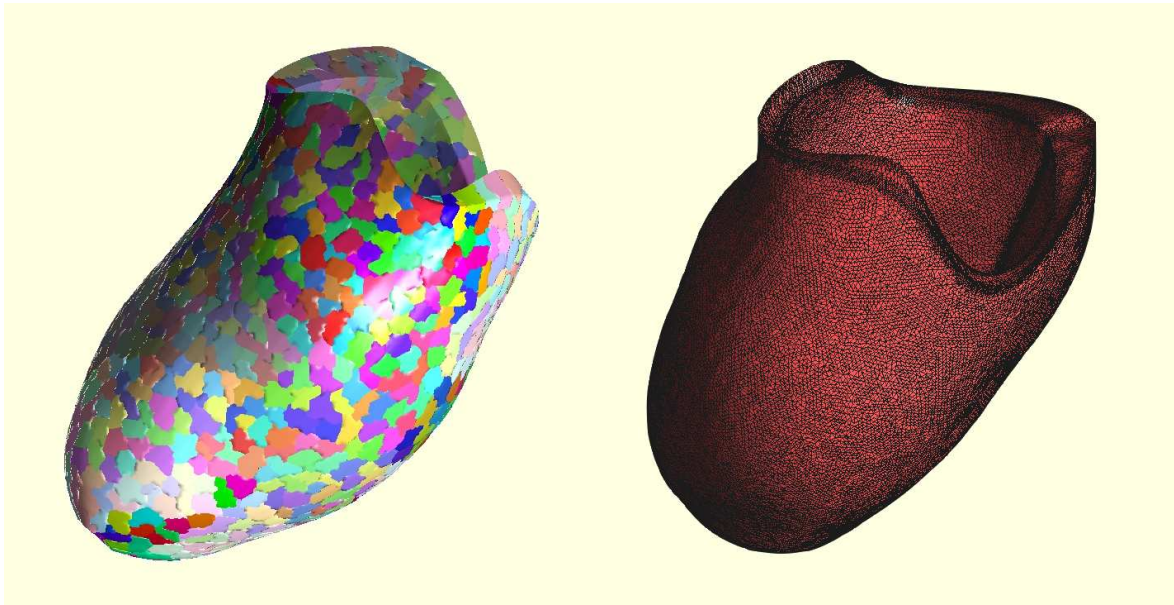
Figure 3.11: 1000-domains mesh partition performed by Metis (left) on a 1M tetrahedra unstructured mesh (right) of a single left ventricle.

5. Exchange the results on the boundary nodes, as was done for the RHS.

3.4.2 Strong scalability

Alya runs efficiently in Marenostrum, the most powerful supercomputer in Spain hosted in Barcelona Supercomputing Center. With the third upgrade (2012-2013), Marenostrum has a peak performance of 1.1 Petaflops, with 48896 Intel Sandy Bridge processors in 3056 nodes, and 84 Xeon Phi 5110P in 42 nodes, with more than 100.8 TB of main memory and 2 PB of GPFS disk storage. At June 2014, Marenostrum is positioned at the 34th place in the TOP500 list of fastest supercomputers in the world.

Alya has shown high parallel efficiency up to several thousands of cores for different physical problems, either coupled or single-physics (Houzeaux et al., 2009, 2011; Puzyrev et al., 2013). Moreover, it has shown scaling behaviour in other supercomputers. In Blue Waters, the supercomputer hosted in the National Center for Supercomputing Applications (NCSA), the code presents a performance up to 100000 cores, achieving more than 85% parallel efficiency. This result contradicts the common belief that engineering simulation codes do not scale efficiently in large supercomputers, opening a new wide horizon of potential applications in the industrial area. The same problem would take 17.4 years for a serial code to do what Alya, on 100000 cores of Blue Waters, can do in less than two hours. Thanks to the high parallel efficiency attained
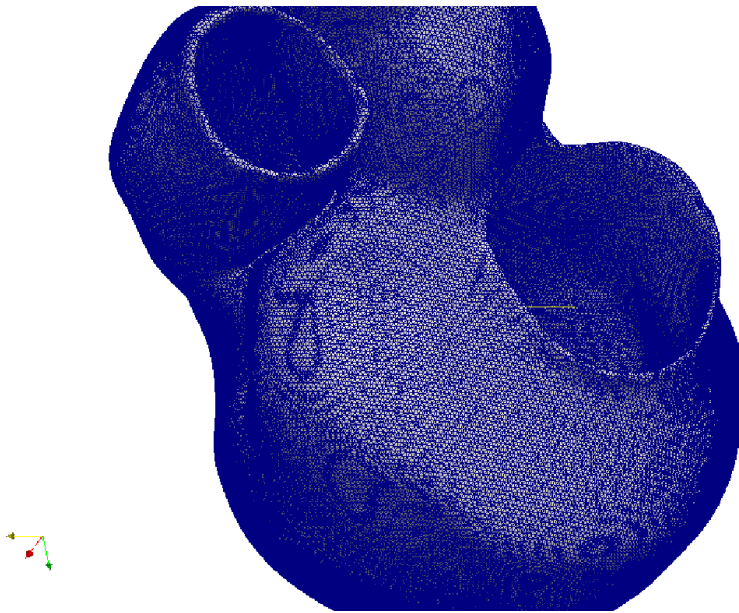
Figure 3.12: Pig biventricular geometry provided by Dr. A. Berruezo (Hospital Clinic de Barcelona) in collaboration with R. Sebastian (Universitat de Valencia) and O. Camara (Universitat Pompeu Fabra).

in codes like Alya, exascale supercomputers will allow solving complex engineers and scientists problems.

CCM parallel efficiency.   For the coupled EM problem, strong scalability measures the CCM parallel efficiency. To illustrate that, a cardiac EM simulation is run for a high-resolution pig biventricular geometry (Fig. 3.12), choosing FHN as the electrophysiological model. A 6M tetrahedral mesh is generated for the geometry provided by Dr. A. Berruezo (Hospital Clinic de Barcelona) in collaboration with R. Sebastian (Universitat de Valencia) and O. Camara (Universitat Pompeu Fabra). The original mesh is progressively subdivided following Houzeaux et al. (2013) in smaller elements, creating a hyerarchy of larger meshes. To perform the scalability test, two meshes coming from the subdivision cycle, 427M and 3.4B elements, are used. They are respectively labelled 'DIV2' and 'DIV3' in Figure 3.13. Scalability is measured upon the time needed to solve one time step. The smaller mesh 'DIV2' shows linear scalability up to 65K processors, being normalized with the 1024 cores run. At 65K 'DIV2' has a mean of 6500 tetrahedra per core. At this end, communication time starts to be noticeable with respect to computing time. However, scalability figures for the larger mesh 'DIV3' are linear up to the top: it is 8 times larger, with a mean of 52K elements per core at 65K cores.
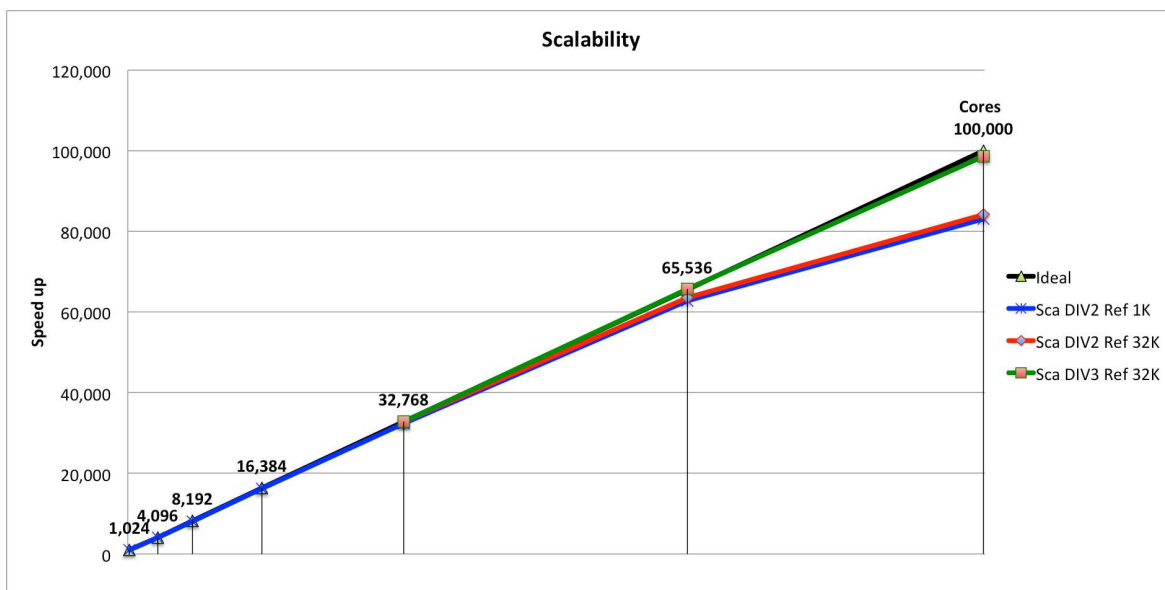
Figure 3.13: Strong scalability in Alya. The vertical axis shows the speedup, the lower horizontal axis is the number of cores and the upper horizontal axis is the elements-per-core average. Tests were carried out in NCSA Blue Waters supercomputer.

Results of the CCM parallel efficiency lead to the congress contribution: M. Vázquez, G. Houzeaux, S. Koric, A. Artigues, J. Aguado-Sierra, R. Arís, D. Mira, H. Calmet, F. Cucchietti, H. Owen, A. Taha, J. M. Cela (2014). Alya: Towards Exascale for Engineering Simulation Codes. *International Supercomputing Conference.*

3.5 Discussion

This chapter introduces the computational aspects of an EM model of the heart, capable of running on supercomputers and flexible enough to easily build up much more complex models, from the numerical algorithms up to the parallel implementation. The purpose of the simulation model is to be capable of reproducing the behavior of the heart with the best degree of accuracy possible in a computer. The resultant simulation tool has to be prepared to include the physiological an mechanical complexity of the currently available models. Moreover, as medical imaging progresses, the highest simulation fidelity is required. For all these reasons, an efficient parallel platform is necessary.

From the numerical point of view, the treatment of the ODE-like terms in the model is introduced. We propose to use a different numerical integration for these terms, similar to that used for the lumped mass matrix. If the ODE-like local terms are 'spacialized',

the solution present spurious numerical effects that can lead to plainly wrong results (notably, the case with zero diffusion). These examples show how a different numerical treatment, which is basically correct, can yield deep errors.

On the computational side, the implementation aspects of the parallel platform Alya are introduced. The combined flexibility and parallel performance give to the proposed approach a great advantage when extending the model towards data assimilation, multi-scales and multi-physics. The present scheme shows almost linear scalability plots for thousands of processors in explicit and implicit formulations. When carefully programmed, this is inherited by all the Physical problems simulated in the platform. Then, in Alya, electrophysiology, mechanical deformation and fluid flow can be coupled retaining this parallel efficiency.

Chapter 4

Applications of the CCM tool

Simulation is an attractive approach for dealing with the many experimental difficulties in determining properties of the heart. An extensive computational model can provide information about cardiac mechanisms that would be impossible to determine accurately by experimental methods.

In this chapter, the CCM tool is applied in several problems to demonstrate the potential of computational simulations. Different electrophysiological and mechanical aspects are studied. Firstly, Aya is used to fit the active force of the cardiac tissue, according to data from the literature. The virtual experiment of modeling the active force of the muscle leads to a surprising result that shows the efficiency of the physical system, the heart. Secondly, a well known standard benchmark is tested in Alya, where the mesh convergence of the code is assessed. Moreover, the framework is used to determine certain properties of the tissue. After that, electrical and mechanical questions are solved through a sensitivity analysis of the simulations. The behaviour of the error in the fiber field reconstruction is investigated in synthetic datasets. Finally, the relation between conductivity and conduction velocity is analyzed.

4.1   Fitting of the active force

In this section, we present a methodology to characterize mechanical properties of the tissue using the CCM tool. The objective is to adjust the active force of the cardiac muscle to reflect the change of volume inside the cavity that has been reported in the literature.
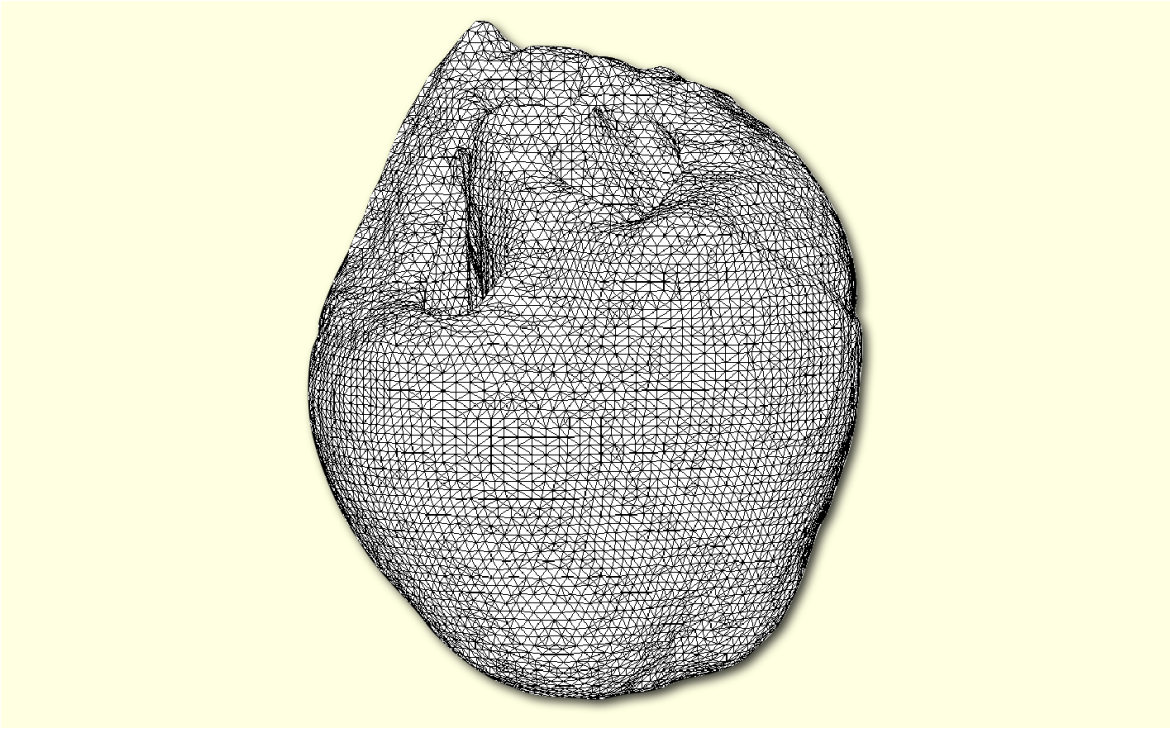
Figure 4.1: Rabbit ventricular mesh, University of Oxford. Discretized in tetrahedral elements using the mesh generator TetGen.

Figure 4.1 shows an anatomically detailed MRI-derived rabbit ventricular model developed by Bishop et al. (2010) at University of Oxford. The experimental fiber field is not available in this study and a mathematical rule-based fiber model is interpolated in the geometry. In order to fit the active force of the computational model, we take into account that in a healthy rabbit heart, the total volume inside the ventricles varies 60% a cardiac cycle (Jung et al., 2012).

In the mechanical constitutive equations, the stress is decomposed in passive and active contributions, with the latter being related to the measured force.

$$\sigma = \sigma_{pas} + \sigma_{act}$$

The action of the active force in contraction in the CCM tool is simulated varying the parameter γ from the following equation:

$$\sigma_{act} = \gamma F_{act}\boldsymbol{f} \otimes \boldsymbol{f}$$

where the active force F_{act} is related to the degree of ventricular filling and the stiffness of the tissue. In order to avoid the cardiac tissue to collapse, we calibrate the active
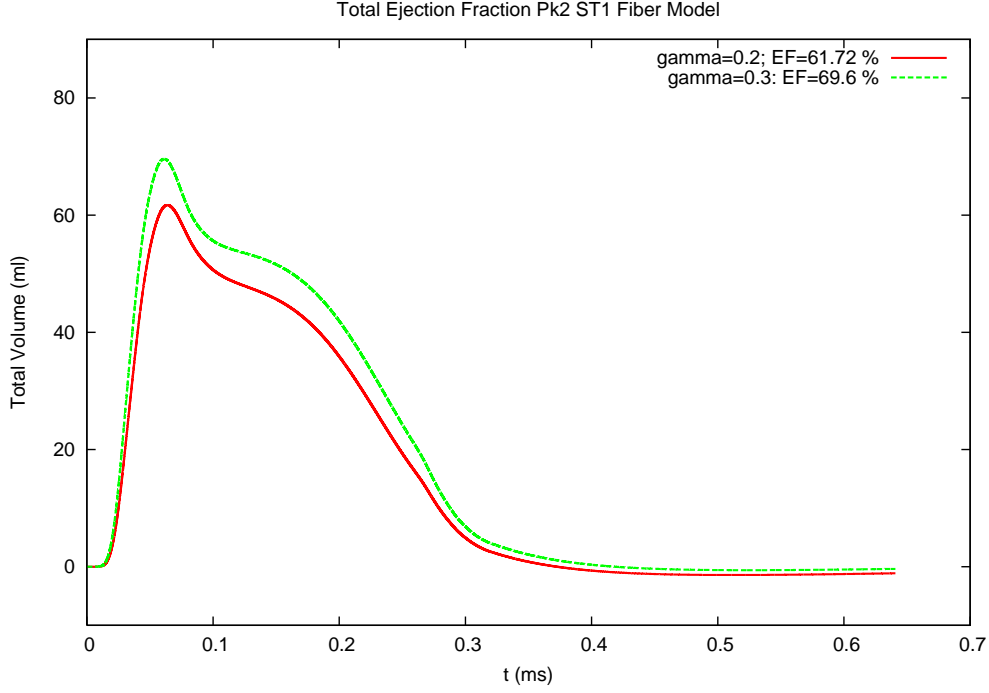
Figure 4.2: Calibration of the active force. The figure represents the change volume inside the cavities vs. time. The theoretical value measured in a rabbit heart is 65%. The CCM tool is calibrated to adjust this percentage.

force of the muscle. The parameter γ, also named control factor, is calibrated against the expected change of volume in the two cavities:

$$EjectionFraction(\%) = \frac{MaximumVolume - MinimumVolume}{MinimumVolume} * 100$$

which is 60% in a healthy rabbit heart. In Alya, the volume inside the cavities is calculated through a discrete form of the Gauss's theorem.

We solve the coupled EM problem in the 3D cardiac domain, using FNH equations for the electrophysiological part. Giving different values of the control factor we observe that choosing $\gamma = 0.2$ or $\gamma = 0.3$ the simulation yields to a ejection fraction (EF) percentage that is close to the expected value. For $\gamma = 0.2$, we measure 61.72 % of the EF and for $\gamma = 0.3$, we measure 69.6 % (Fig. 4.2). Although both results are sufficient for our purpose, we choose $\gamma = 0.2$, which is nearer to the theoretical value.

Discussion.   This application has been designed to calibrate the active force. The parameter γ has been fitted to accomplish the theoretical EF value, finding that $\gamma = 0.2$ yields to an acceptable result, close to the experimental one. Therefore, simulations

performed in this thesis use $\gamma = 0.2$ in most of the situations. In case of simulating a new circumstance, such as a pathological situation, the same procedure should be taken into account to calibrate the active force of the muscle.

In addition, an indirect result has been found. Notice that increasing the active force 30% of its value, the EF only increases 8%. Although the fiber model used in the simulation is a mathematical approach, the helical structure of the heart gives stability an efficiency to the system. Varying considerably the contraction force, the EF does not change the same amount. The design of the heart compensates a wrong functioning of the tissue because of the microstructure disposition, saving the global behavior. This unexpected result could explain that in some occasions the heart continues pumping after a cardiac dysfunction, as in a damaged heart where non-beating cells form scar tissue. The complexity of the cardiac architecture is an evidence. The complex arrangement of myocites distributes the energy efficiently to pump a sufficient supply of blood, even when some part of the tissue is damaged. As Streeter et al. (1969) said, "No man-made structure is designed like a heart". Nowadays, existing techniques can not provide complete descriptions of the global muscular architecture. Simulations can help to improve them.

Conclusion.   The results show the potential of the framework, which is a virtual lab that can help to interpret theories that are not validated yet. In the present application, we underline two main features:

1. Decreasing the active force 30%, the EF value only decreases 8%.

2. The helical structure of the fiber field gives efficiency and stability to the cardiac ventricles. Variations in the properties of the material can be compensated by the system, allowing the heart to behave normally.

4.2   Relation between conductivity and conduction velocity

Accurate conductivity values are essential for realistic simulations of cardiac electrophysiological phenomena. Nowadays, the experimental determination of those data is hard to obtain and results present large variation because of the complexity of the measurements. Although conductivity values are available from measurements in
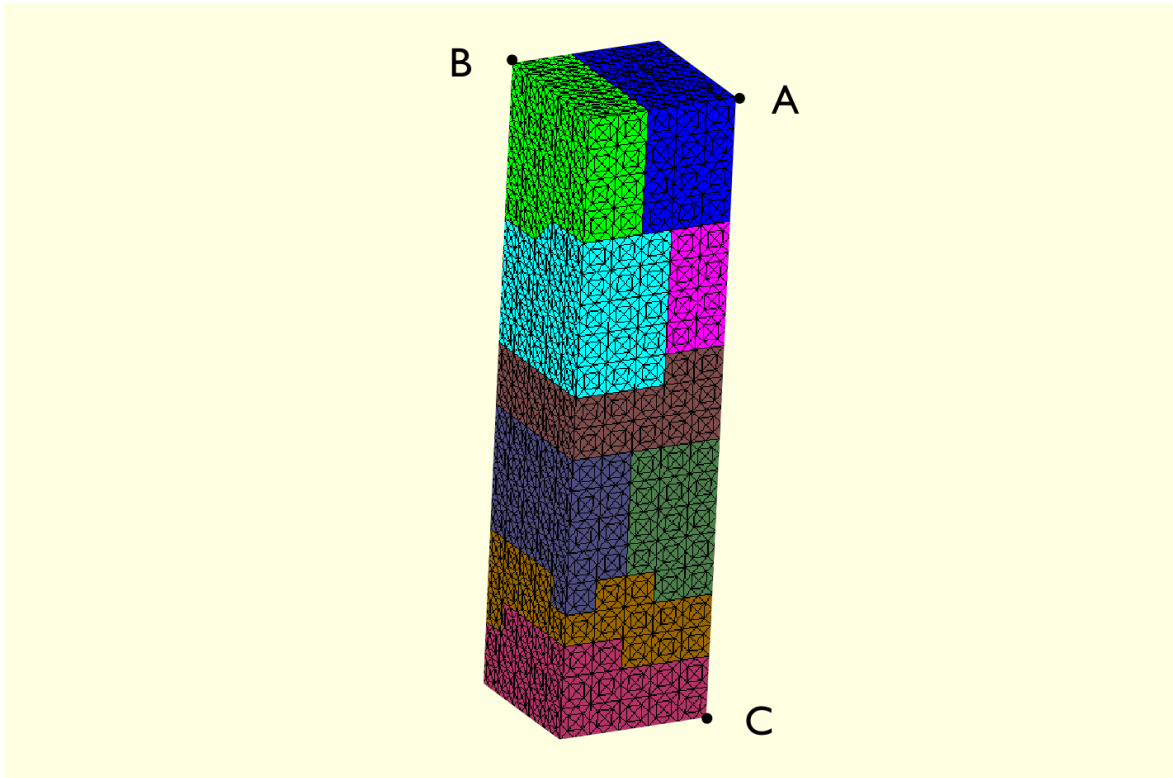
Figure 4.3: 3D slab of cardiac tissue. Colours represent the different domains when solved in parallel. A and B represent nodes of initial stimuli. C represents the node where the velocity is measured.

the laboratory (Roth, 1997), results can vary depending on the experiment, producing significantly different simulation output. Apparently, there is no preferred conductivity value agreement in the community.

Myocardial structure is considered anisotropic because of the existence of the fiber field. The current propagates more rapidly along the tissue fibers than across them. In the governing equations, the conductivity tensor represents the anisotropy of the cardiac tissue (Eq. 2.3), which is composed by the axial and crosswise fiber conductivities. As explained in chapter 2, in the local basis the conductivity tensor D is diagonal, where k_f, k_s and k_n are the axial and crosswise conductivities. Experiments in mammalian hearts have determined that the electrical conduction velocity is three times faster along the myocardial fibers than in a perpendicular direction (Clerc, 1976; Roberts et al., 1979; Rubart and Zipes, 2001; Coghlan et al., 2006). Supposing the same relation in D, the crosswise conductivity should be one third of the axial conductivity ($k_f = 3k_n = 3k_s$).

Cardiac simulation is an appropriate tool to determine parameters and properties that are hard to obtain, such as conductivity (Stinstra et al., 2005). The present study aims
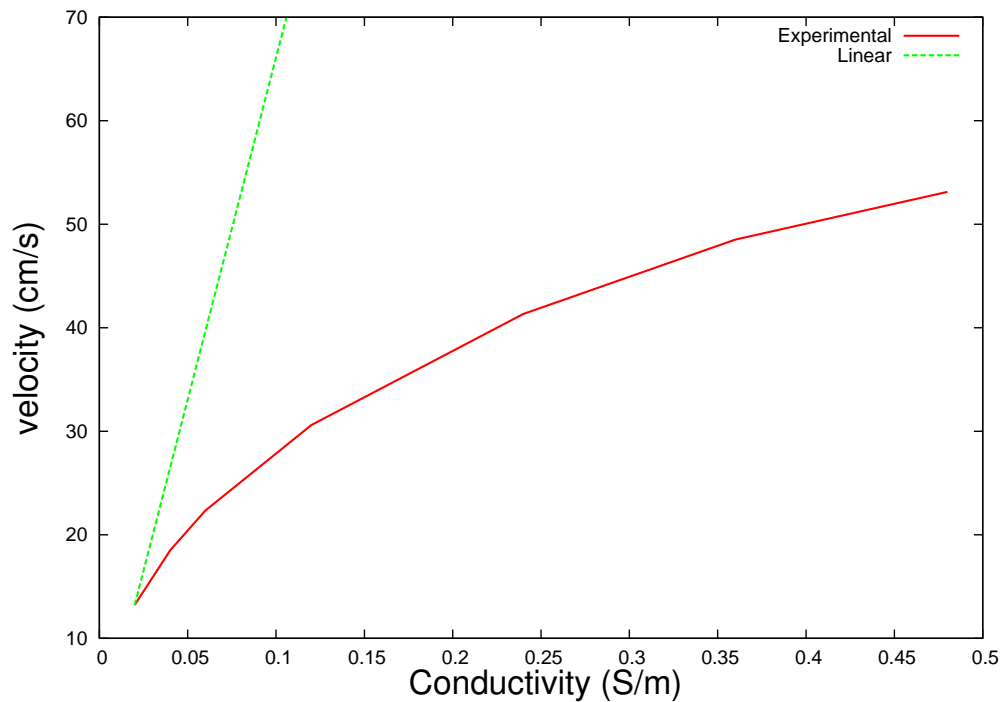
Figure 4.4: The relation between the conductivity and the velocity of propagation is not linear. Green line corresponds to the lineal case. Red line corresponds to the measured relation.

to examine the electrical propagation in the cardiac tissue to answer the question 'How conductivity and conduction velocity are related?'.

FHN model is used to simulate the electrical activity of the heart in a 3D slab of cardiac tissue, consisting in a cuboid of 2.5 mm x 2.5 mm x 10 mm. Fibers are defined to be aligned in the long axis (10 mm) of the cuboid. The domain discretized in 96000 elements, where $\Delta x = 0.25$ mm. To investigate the relation between conductivity and conduction velocity, the tissue is considered isotropic ($k_f = k_n = k_s$). The stimulus current is located at one corner of one face (2.5 mm x 2.5 mm) of the slab (point A in Figure 4.3). Values of the conductivity along the fibers are changed from 0.02 S/m to 0.48 S/m. For each value, the simulation of the electrical propagation is performed and the velocity along the fibers is measured. If exists the same relation between conductivity and conduction velocity, the velocity should increase linearly with the conductivity.

Results are presented in Figure 4.4. Red line corresponds to the experimental relation between conductivity and conduction velocity. Green line represents the assumed relation. From this graphic, we observe that the relation between the conductivity and the conduction velocity is not linear. If we increase the conductivity linearly, conduction

velocity does not increases the same amount. To obtain a conduction velocity that approximately increases by three, the conductivity needs to be increased by ten:

$$k_f = 0.24 \ S/m \implies v_f = 41.33 \ cm/s$$

$$k_n = k_s = 0.02 \ S/m \implies v_n = v_s = 13.22 \ cm/s$$

Finally, to check if the relation in the conduction velocity is fulfilled with the new values, we perform the anisotropic case choosing the conductivity values that we have found ($k_f = 0.24$ S/m and $k_n = k_s = 0.02$ S/m). The experimental velocities in the anisotropic case are the following:

$$v_f = 45.73 \ cm/s \ ; \ \ v_n = v_s = 17.17 \ cm/s$$

We observe that the relation between the axial and crosswise velocities has is close to the relation that has been reported in the literature ($v_f = 3v_n = 3v_s$).

Discussion. Results clearly show that the relation between the conductivity and the velocity of propagation is not linear. For each situation, the conductivity needs to be calibrated with the simulation. Therefore, we propose a framework to calibrate the conductivity parameters for each new case:

1. Explore a range of k_f. For each conductivity value, perform the isotropic electrical simulation and measure the resultant conduction velocity along the fibers (v_f).

2. Plot the conductivity versus the conduction velocity.

3. Choose the axial and crosswise conductivities from the graphic, keeping the experimental relation $v_f = 3v_n = 3v_s$.

4. Check if the relation is fulfilled in the anisotropic situation.

The method should be applied for a new electrophysiological model implemented in the code.

Conclusion. As in the previous sections, this result shows the potential of the simulation platform as a virtual lab where cardiac properties can be tested. The main conclusion of the present application is that the relation between the conductivity and

the conduction velocity is not linear. In addition, a new framework has been presented. The method should be used to calibrate every new electrophysiological model and find the conductivity parameters that fulfill the experimental evidence between the velocity, along the fiber field and transversally.

4.3   Mesh convergence

Cardiac electrophysiological simulations are becoming increasingly complex. Computational codes represent the detailed physiology and pathologies of the heart, while at the same time take advantage of the computational potential of HPC architecture. To verify that the code gives a faithful representation of the governing equations, Niederer et al. (2011) have provided a N-version benchmark to the community. N-version code comparisons studies are typically applied in contexts where simulations are intrinsically unable to be validated against direct observations. The benchmark has been created to generate a consensus converged solution. The test assesses if the simulation software produces the same electrophysiological result at multiple spatial discretizations.

The geometry used in this section is the same as in the previous one, a cuboid of 2.5 mm x 2.5 mm x 10 mm. Fibers are defined to be aligned in the long axis (10 mm) of the cuboid and the stimulus current is located at the corner of one face (2.5 mm x 2.5 mm) of the slab (point A in Figure 4.3). Initially, the membrane potential is set to -85 mV. The benchmark is performed in Alya. The problem is solved at four spatial resolutions ($\Delta x = 0.5$ mm, 0.25 mm, 0.125 mm, 0.0625 mm) and each spatial resolution is solved with a PDE time step ($\Delta t = 0.08$ ms, 0.02 ms, 0.0017 ms, 0.00032 ms respectively). Using a monodomain model (FHN equations for the non-linear term) with transversely isotropic conductivity, the governing equations are solved explicitly. Both open and closed rules are used in the integration scheme to study if this subtle difference in implementation can cause discrepancies in the simulations. We measure the velocity of propagation at the opposite corner of the cuboid, considering that the node is activated when the upstroke passes through 0 mV.

Two different situations are studied. Firstly, we consider that the propagation in the cardiac tissue is isotropic. Secondly, we consider the anisotropic version.

1. Isotropic.   The conductivity along the fiber is set to 0.12 S/m. In this case, we measure the velocity along the fiber direction, from point A to point C (Fig. 4.3). The distance between the corners is 1 cm. The propagation wave is illustrated in one face of
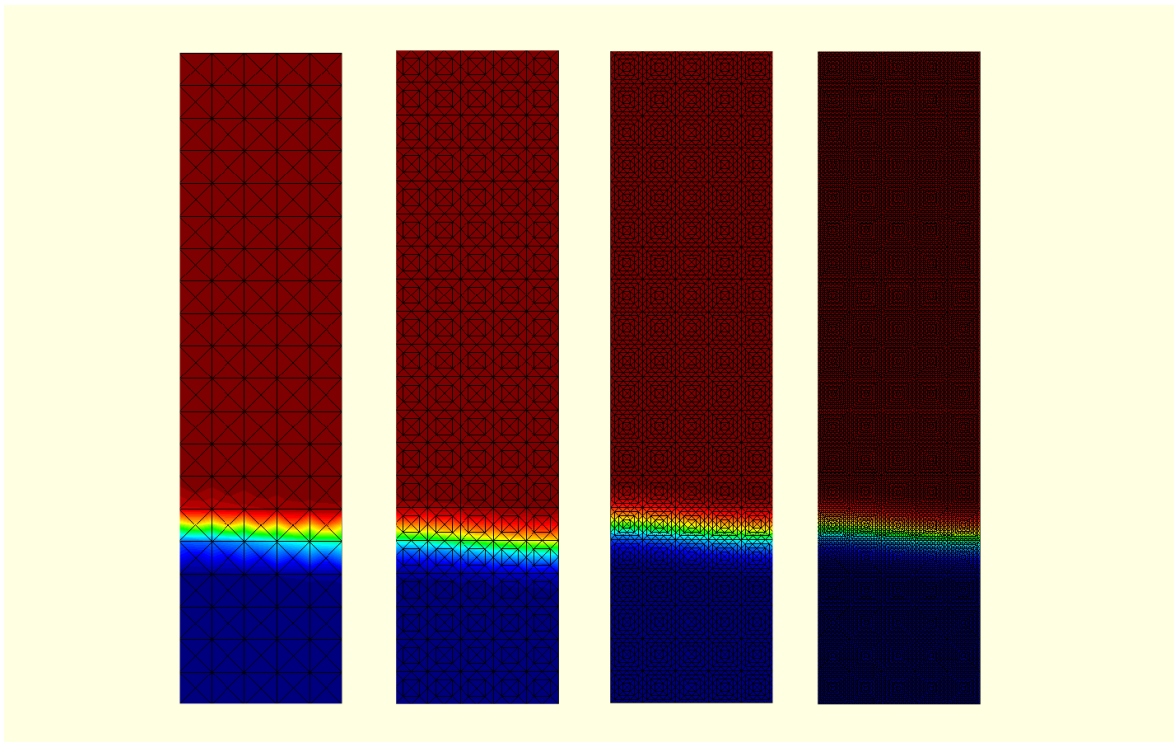
Figure 4.5: The problem is solved at four spatial resolutions. From left to right, $\Delta x = 0.5$ mm, 0.25 mm, 0.125 mm and 0.0625 mm. Colours represent the evolution of the action potential trough the cardiac tissue.

Elements	Δx (mm)	C: velocity (cm/s)	O: velocity (cm/s)
12000	0.5	30.15	31.75
96000	0.25	30.61	31.01
768000	0.125	30.76	30.98
6144000	0.0625	30.78	30.84

Table 4.1: Velocity of the wave front calculated in the same domain with different spatial discretization for the isotropic case. Results for closed (C) and open (O) integration rules.

the cuboid in Figure 4.5. On the left side of the figure, the geometry has been discretized in space of 12000 elements. Solving the FHN equations in this domain and using the closed integration rule, the velocity of the propagation wave that is measured is 30.15 cm/s. In the second case, the mesh is refined and the total elements in the same domain increases to 96000. The velocity recorded in this slab is 30.61 cm/s. In the third case, the mesh contains 768000 elements and the velocity gives 30.76 cm/s. Finally, the fourth discretization corresponds to a mesh of 6144000 elements. In this case the velocity is 30.78 cm/s, which can be considered equivalent to the previous result. The behavior of the system is stable for spatial discretizations lower than $\Delta x = 0.125$ mm, giving the same velocity. Moreover, open and closed rules are used in the integration scheme, causing discrepancies up to 5% (Table 4.1). With the closed integration, the activation presents an increase of time, specially for coarser resolutions.

1. Anisotropic. The conductivity along the fiber is set to 0.24 S/m and the transversal directions are set to 0.02 S/m. From the starting point of the stimulus, point B in Figure 4.3, and the opposite corner, point C in Figure 4.3, the distance is 1.601 cm. In this case, only the closed integration scheme has been used. The resultant velocities are summarized in Table 4.2. As in the isotropic case, the system behaves stable for spatial discretizations lower than $\Delta x = 0.125$ mm.

Elements	Δx (mm)	velocity (cm/s)
12000	0.5	31.28
96000	0.25	33.58
768000	0.125	34.02
6144000	0.0625	33.91

Table 4.2: Velocity of the wave front calculated in the same domain with different spatial discretization for the anisotropic case.

Discussion.   The benchmark presented in Niederer et al. (2011) has been tested in a cuboid using four different spatial discretizations. The velocity calculated for the solver at coarse spatial resolutions is substantially closer to that obtained with the finest spatial resolution. This result shows mesh convergence of Alya. As the authors reported in the paper, codes performing simulations with and without mass lumping obtain different times. Using the mass lumping (closed integration) an increase of time in the activation pattern is recorded, specially for coarser resolutions. This effect is also captured with Alya. The closed rule yields to smaller velocities, specially for the coarsest mesh.

Conclusion.   In the spatial range we are working in this thesis, the velocities become stable. Results obtained at coarse and fine spatial resolutions are close, specially at high resolution meshes.

4.4   Effect of the noise in the cardiac fiber field

The cardiac fiber field can be obtained experimentally with the image technique DT-MRI, but the acquisitions always include noise in its recordings. The noise is originated by two components: the scanner apparatus and the patient breathe inside the scanner. In cardiac MRI images, random noise is essentially white and has its origin in thermal Brownian motion of electrons.

The CCM tool is used here to assess the effect of errors in the input fiber field, derived from the data acquisition methodology, and to evaluate the error sensitivity. In this case, only the electrophysiological governing equations are solved, using FK model. A cubic-shaped slice of cardiac tissue has been used, which has a crosswise fiber field (Fig. 4.6). Three different examples of the same slab are simulated: one with a uniform fiber field, set as the reference, and two more with perturbed fiber fields (10% and 20% of random noise). The percentage of error added to the direction of fibers in the reference is defined by $\alpha \pm \alpha \cdot g \cdot r(x_i)$ where $g = 0.1$ or $g = 0.2$ and $0 \leq r(x_i) \leq 1$ is a random function defined for each point in space x_i. To quantify the error of such a transient problem, the isochrones are calculated for each case. The isochrones are contour lines connecting points where the propagating potential reach a marker value at the same time (-5 mV in this case). Once the polarization wave passes through all the domain, the isochrone field can be compared for the different cases in the discrete L^2 norm.
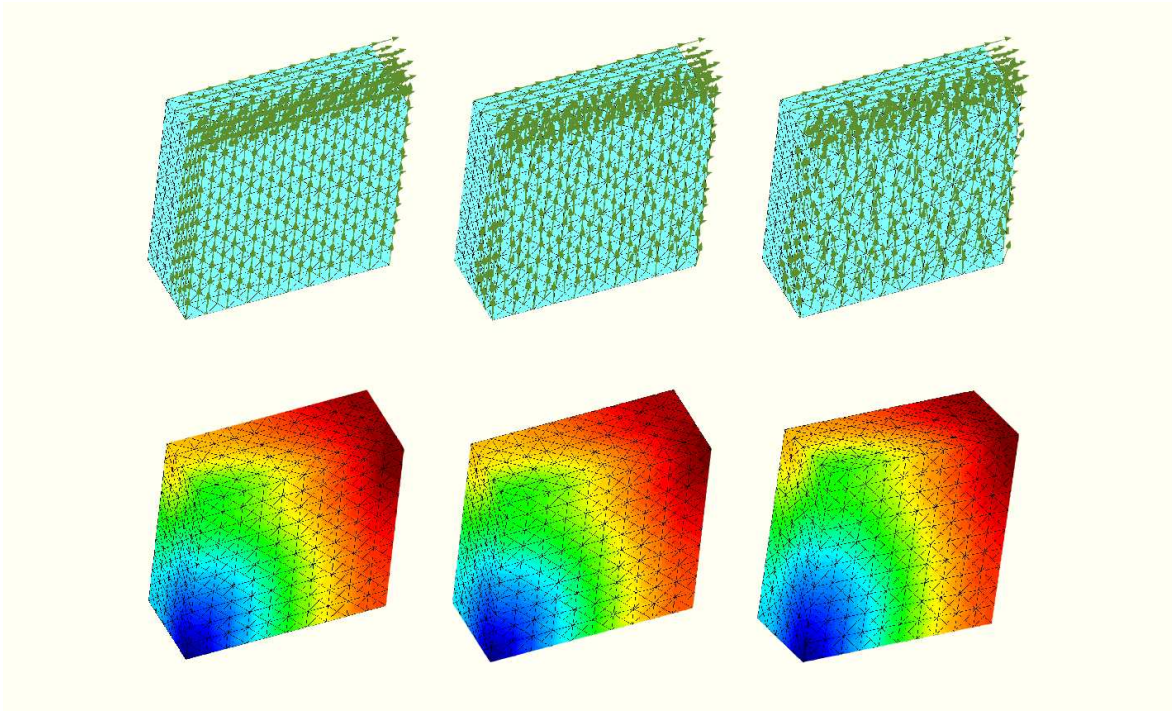
Figure 4.6: Noise in fiber orientation in 3D. In (a) the distribution of fibers has no noise. In (b) noise in fiber orientation has grown up to 10%. Fibers in (c) has 20% of random noise. The corespondent isochrones are (d), (e) and (f). FK model has been used in the simulations.

Discussion. In this section we study the effect of the noise that appear in the acquisition of the fiber field. Usually, cardiac images include noise in the captured data. To simulate this situation, random noise has been added into the synthetic data. Results presented in Figure 4.6 show the influence of the noise in the direction of the electrical propagation in cardiac tissue. We present three different situations: The exact fiber field and two situations containing noise in the fiber direction. In the first row, the fiber field orientation is drawn for each case. Isochrones suggest that 10% of random noise in the acquisition does not significantly compromise the temporal pattern of the electrical wave. However, the maps indicate local differences in the case of 20% of random noise. This result would suggest that, when obtaining highly error acquisitions, the orientation of the anisotropy varies.

Conclusion. In the present application, we underline two main features:

1. 10% of random noise in the acquisition does not significantly compromise the temporal pattern of the electrical wave.

2. High error acquisitions varies the orientation of the anisotropy.

Chapter 5

Data assimilation. Inverse problem

The construction of cardiac models that describe accurately the behavior of the heart is a challenging task. Computational modeling has already shown a great potential to better understanding mechanisms involved in pathologies. However, assimilation of clinical data is a crucial step to increase the model reliability and to obtain quantities of interest in-silico. An accurate modeling requires the characterization of the electrical and material properties of soft tissue, which most of the times are not accessible through clinical technology directly or that have to be acquired *ex-vivo*. Nowadays, data assimilation methods permit an objective characterization of myocardial tissue. Some of the EM properties of the cardiac muscle can be determined indirectly, combining mathematical algorithms and experimental data. However, extracting the values from the available measurements is not always possible. For example, some material parameters, such as myocardial stiffness, still remain unknown.

The CCM tool presented in this thesis uses a large amount of parameters and some of them are not determined experimentally. In this chapter, we perform two data assimilation techniques to find some values. In the first part, we review the Kalman Filter method, for the effective estimation of relevant physical parameters and we apply the technique to the 1D FHN equation. Specifically, the electrical problem is studied with the Ensemble Kalman Filter to estimate the conductivity. In the second part, parameters of the mechanical problem are estimated with another inverse problem. This section is the result of a collaboration with the biomedical Engineering group at King's College London. The mechanical characterization of the cardiac tissue is performed in a human left ventricle (LV) geometry using their in-house simulation code *Cheart*. The aim is to make a detailed analysis of the sensitivity to one of the uncertainties of the process: the distribution of fiber orientation.

This is a first approach of the inverse problem. The discretization of the partial differential equations is carried out using the finite differences method and is implemented in an in-house Fortran code. In the future, it will be extended to the FEM formulation and it will be integrated in the CCM tool in Alya.

5.1   Kalman filters

This section gives a brief introduction to the Kalman Filters (KF), as sequential data assimilation methodologies and outlines the general theory of the Ensemble Kalman Filter (EnKF), which is used in non-linear problems. The aim is to present a comprehensive derivation of the KF used for the parameter estimation in 1D electrophysiological problems.

The KF is a computational algorithm that can estimate the variables of a wide range of processes. Measurements are combined with the mathematical model to predict the evolution of the system and to estimate the variables, parameters or initial conditions of the model (Kalman, 1960). The KF is a sequential filter method. It is integrated forward in time and, whenever measurements are available, they are used to reinitialize the model before the integration continues.

The behavior of the physical system is described through the state equation. The vector x contains all of the information about the present state of the system, but cannot be measured directly. Instead, vector y is measured, which is corrupted by the noise z. Using the knowledge of the system and the measurement dynamics, the estimator gives an accurate value of the current state.

The filter is build under two premises:

- The KF estimates the states of a system. The average value of the state estimate has to be equal to the average value of the true state.

- The state estimate should have the smallest error possible compared to the true state. In mathematical terms, the filter minimizes the variance of the estimation error.

5.1.1 Kalman filters for linear systems

If the physical process can be approximated as a linear system ($x_{k+1} = Ax_k + B_k u_k$), the KF can be described by the following two equations:

$$
\begin{aligned}
x_{k+1} &= Ax_k + B_k u_k + w_k \\
y_{k+1} &= C_k x_k + z_k
\end{aligned}
\tag{5.1}
$$

where k is the time index, u is a known input and A, B, and C are matrices. The process noise is represented by w.

The noise covariance matrices S_w and S_z are defined as:

$$
\begin{aligned}
S_w &= E(w_k w_k^T) \\
S_z &= E(z_k z_k^T)
\end{aligned}
\tag{5.2}
$$

where $E()$ is the expected value. The process noise covariance is $S_w = E(w_k w_k^T)$, also named Q, and $S_z = E(z_k z_k^T)$ is the measurement noise covariance, also named R. The general formulation of the KF is given as follows:

$$
\begin{aligned}
K_k &= P_k C^T (C P_k C^T + S_z)^{-1} \\
x_{k+1} &= (Ax_k + Bu_k) + K_k(y_{k+1} - Cx_k) \\
P_{k+1} &= (I - KC_k)P_k
\end{aligned}
\tag{5.3}
$$

where K matrix is called the Kalman gain and P matrix is the estimation error covariance. K is chosen to be the gain that minimizes the error covariance P.

In the filter, x_{k+1} represents the state vector in the system model corrected by the second term $K_k(y_{k+1} - Cx_k)$. The difference $y_{k+1} - Cx_{k+1}$ is called the measurement innovation, or the residual. The residual reflects the discrepancy between the predicted measurement Cx_{k+1} and the measurement y_{k+1}. The state estimate x_{k+1} has to be corrected due to the measurements. If the measurement noise is small, S_z will be small and K will be large. In this case, high credibility will be given to the measurement when computing the next state estimate x_{k+1}. On the contrary, K will be small in case of low confidence on the measurement y.

Computational Cost   The computational cost associated with matrix inversion is proportional to n^3, where n is the number of elements in the domain and also the size of the matrix (Kalman, 1960).

5.1.2   The Ensemble Kalman filters for non-linear systems

Non-linear systems are treated with Extended Kalman filter. Particularly, the Ensemble Kalman Filter (EnK) is used in this section. It is an extension of the linear KF theory to non-linear systems, representing the distribution of the system state using a random sample called the ensemble. At the current assimilation time, the EnKF assumes that the forecast error is randomly sampled by an ensemble of forecasts, denoted by x_1^e , x_2^e,... x_N^e . The forecast ensemble consists of N members, which are state vectors of dimension n:

$$X^e = \left(\begin{array}{cccc} x_1^e, & x_2^e, & ..., & x_N^e \end{array}\right) \tag{5.4}$$

The ensemble mean is defined by

$$\overline{x}^e = N^{-1} \sum_{i=1}^{n} x_i^e \tag{5.5}$$

and the perturbed observations are $y_i^k = y^k + v_i^k$ where $v_i \sim N(0, R)$ is the associated noise. The ensemble perturbation from the mean for i-th member is $x'^e = x_i^e - \overline{x}_i^e$. In the EnKF the covariance matrix is replaced by the sample covariance of the ensemble the matrix E_x:

$$E_x = \left(\begin{array}{cccc} x_1^e - \overline{x}_1^e, & x_2^e - \overline{x}_2^e, & ..., & x_N^e - \overline{x}_N^e \end{array}\right) \tag{5.6}$$

and the estimation error P is determined by:

$$P = \frac{E_x E_x^T}{N - 1} \tag{5.7}$$

Implementation of the filter.   For each ensemble member, the EnKF is described as:

$$\begin{aligned} x_i^{k+1} &= x_i^k + K^k(y_i^{k+1} - Cx_i^k) \\ K &= P_k C^T (C P_k C^T + R)^{-1} \end{aligned} \tag{5.8}$$
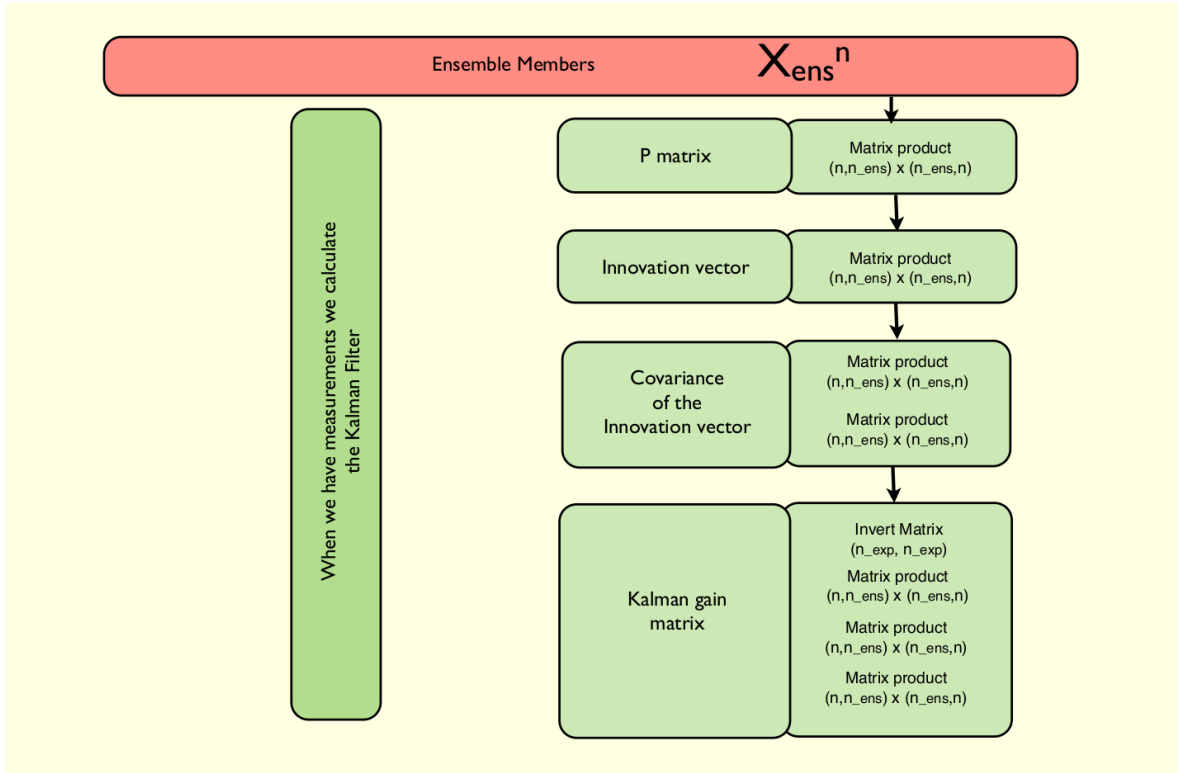
Figure 5.1: Operations involved when solving the EnKF.

Figure 5.1 presents an schematic view of the operations involved when solving the EnKF, where n represents the number of elements in the domain, n_{exp} is the number of measurements and n_{nsml} is the number of ensembles.

5.1.3 Non-Linear Application: FHN equation

In this section, we illustrate the methodology presented above with the estimation insilico of electrical parameters in the 1D FHN governing equations. The EnKF and the partial differential equations of the electrophysiological problem are implemented in an in-house Fortran code. For simplicity in this first approach, the discretization is carried out using the finite differences method. In the future, it will be extended to the FEM formulation in Alya.

The reaction-diffusion equation in the 1D FHN model is given by:

$$\frac{\partial V}{\partial t} = D\frac{\partial^2 V}{\partial x^2} + I_{Ion} \tag{5.9}$$
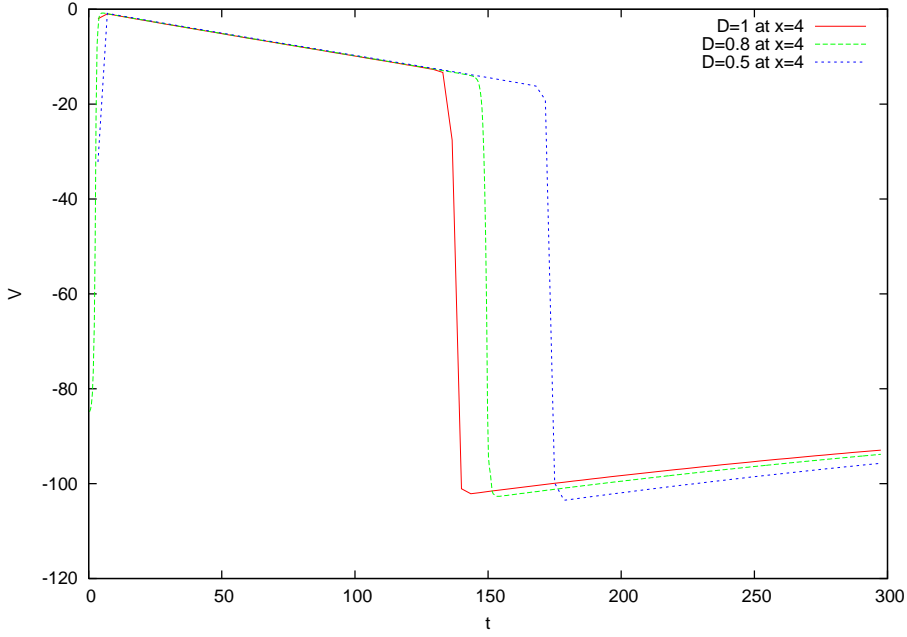
Figure 5.2: True potential evolution in $x = 4$. Some results for conductivity D are plotted. Units: V (mV), t (ms), D (S/m).

Using the finite differences method, the iterative scheme yields to:

$$
\begin{aligned}
V_x^{n+1} &= V_x^n + D\frac{\Delta t}{(\Delta x)^2}(V_{x+1}^n - 2V_x^n + V_{x-1}^n) + C_1 V_x^n(V_x^n - \alpha)(1 - V_x^n) + C_2\omega \\
\omega^{n+1} &= \omega^n + \Delta t\epsilon(V_x^n - \gamma\omega^n)
\end{aligned}
\tag{5.10}
$$

The governing equations are solved in 1D computational domain, discretized in 10 elements. This is a very coarse mesh, which is useful to test the method. Therefore, we use the easy framework to analyze some problems related with the EnKF.

Estimation of D.   Nowadays, action potential in myocardial tissue can be measured experimentally, but conductivity values can not be measured directly. To characterize the conductivity of the system in a controlled situation, we propose an in-silico framework using the EnKF.

In 1D, the conductivity is a scalar. The true result is generated numerically solving the governing equations of the FHN model. Notice that different values of D leads to a significant difference in the action potential's shape (Fig. 5.2). As showed in chapter 4, the relation between conductivity and conduction velocity is not linear. In the figure, we can observe the same behavior: reducing the conductivity value, the velocity of the wave is also reduced but it is not keeping the same relation.

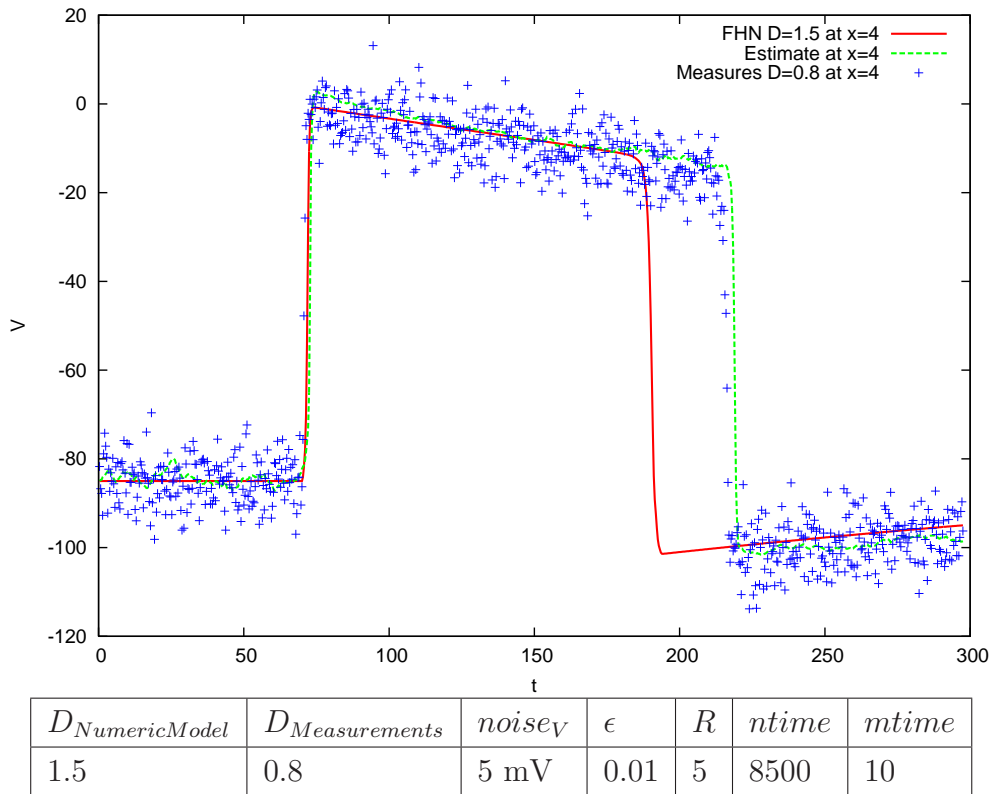| $D_{NumericModel}$	$D_{Measurements}$	$noise_V$	ϵ	R	$ntime$	$mtime$
1.5	0.8	5 mV	0.01	5	8500	10

Figure 5.3: True potential and estimation obtained from EnKF in $x = 4$. Values used in the EnKF to generate the numerical result (true solution) and the measurements. In this case, $R = 5$. Units: V (mV), t (ms), D (S/m).

To perform the EnKF, we compute the numerical solution of the FHN model. We use the FD scheme in space and explicit solver in time. Firstly, we compute the simulation with the conductivity value $D = 1.5$ S/m. The result is set as the reference (true result). Secondly, measurements are generated in-silico, adding Gaussian noise to the numerical solution of the FHN equation in the 1D domain. In this case, the conductivity is set to $D = 0.8$ S/m and the Gaussian noise is 5 mV. To determine the estimate of $V(x, t)$, the EnKF is implemented using 50 ensembles. The values are presented in Figure 5.3, where $ntimes$ refers to the total simulation time and $mtimes$ refers to the time interval when the measurements are created. R is the matrix associated with the noise in the measurements, which gives the confidence in the measurements.

The result of the EnKF is plotted in Figure 5.3. Notice that a large number of measurements are available in this process (blue points). Although the numerical solution is calculated with $D = 1.5$ S/m (red line), the confidence in the measurements ($R = 5$) and the large amount of measurements produce an action potential corresponding to $D = 0.8$ S/m. The filter gives a solution corrected by the measurements (green line).

In this example, the steps in the parameter estimation procedure are the following:

1. Compute the electrophysiological equations with the theoretical value ($D = 1.5$ S/m).

2. Correct the solution with the measurements that are available, performing the EnKF.

3. Evaluate the parameter from the estimated action potential. From the graphic we estimate the value of the parameter to $D = 0.75$ S/m.

Confidence of the filter R. From the previous study, we observe that results depend on the confidence of the filter. To study the effect of R matrix, we consider the same situation as in the previous case and we test different values of R in the EnKF. Theoretical action potential and measurements are obtained using the same parameters introduced above. Then, the filter is implemented twice, choosing $R = 20$ and $R = 0.1$.

On the one hand, Figure 5.4 shows the result of the EnKF with $R = 20$. In this case, the estimated electrical wave is similar to the one presented in Figure 5.3. For comparison with the true potential evolution, we can affirm that the conductivity parameter is close to $D = 0.75$ S/m. On the other hand, Figure 5.5 shows the result of the the filter using $R = 0.1$. In this case, the action potential presents fluctuations because the estimated electrical wave is following the measurements, more than in the previous case. The filter believes the noisy measurements and follows them. From the figure, we can affirm that the parameter is close to $D = 0.85$ S/m.

Effect of the number of measurements available. In the in-silico processes previously presented, a large number of measurements are available. However, not always we have access to this amount of data. The parameter calibration is also possible when physical experiments have a narrow window of measurements.

Figure 5.6 illustrates the result of the EnKF considering less measurements than the previous example. On the top, the filter uses $R = 20$ to estimate the action potential. In this case, the repolarization and the depolarization of the electrical wave are not captured correctly. Since we have less measurements, we need to increase the confidence of the filter. On the bottom, the figure shows the result in the same situation using $R = 5$. In this case, the estimated action potential is closer to the real one. From this result, we observe that if the number of measurements is small, a smaller R is convenient.
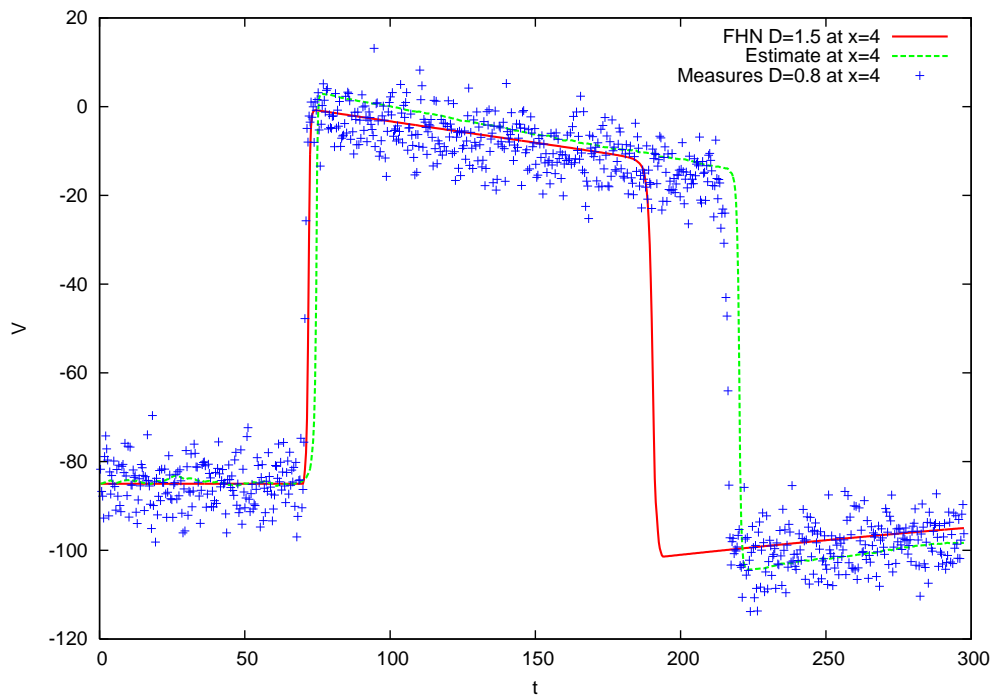
Figure 5.4: The confidence of the filter is $R = 20$. The filter responds to the measurements slowly. Units: V (mV), t (ms), D (S/m).
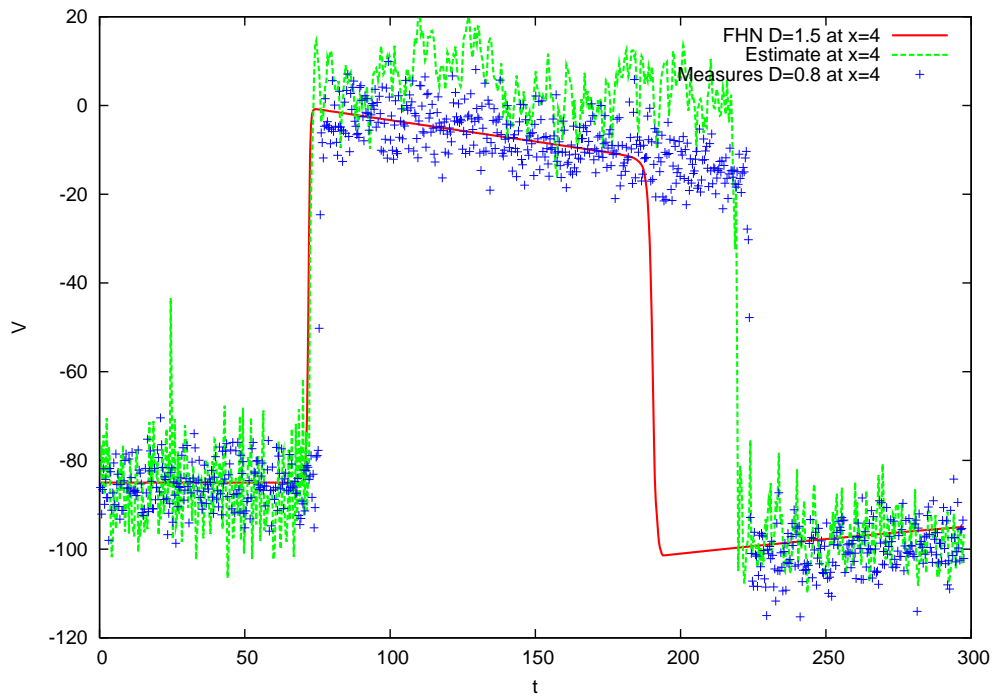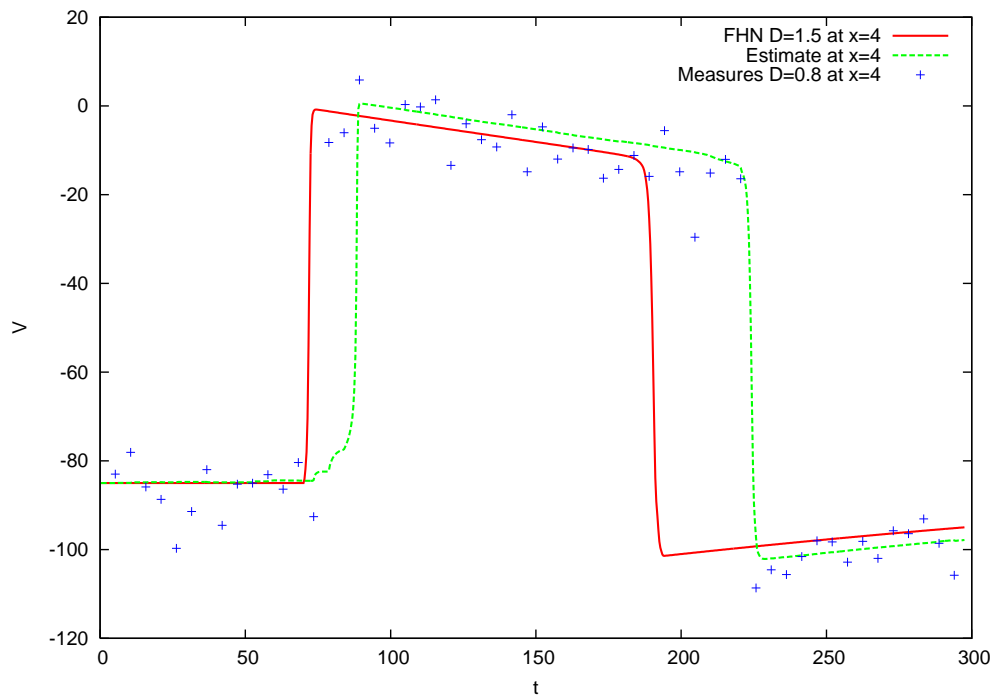

Figure 5.5: The confidence of the filter is $R = 0.1$. In this case, the filter is following the measurements. Units: V (mV), t (ms), D (S/m).

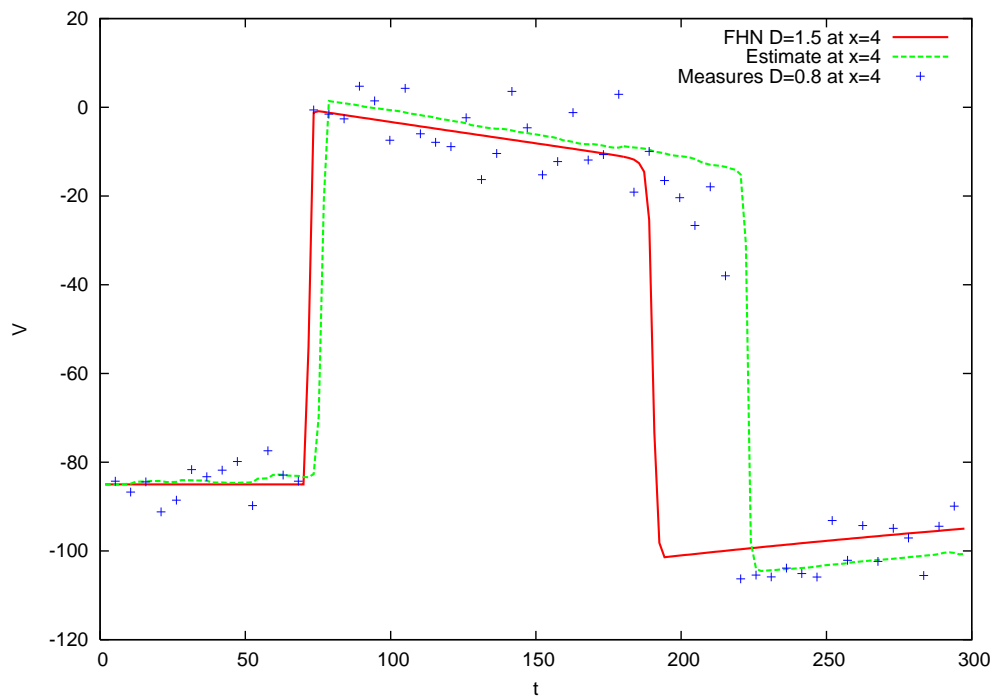| $D_{NumericModel}$	$D_{Measurements}$	$noise_V$	ϵ	$ntime$	$mtime$
1.5	0.8	5 mV	0.01	8500	150

Figure 5.6: Result of the EnKF considering less measurements. Top: $R = 20$. Bottom: $R = 5$

5.1.4 Discussion

EnKF is a suitable method to estimate parameters in non-linear problems. In this section we have applied the filter to determine the conductivity in the 1D FHN equation. We have seen that if we have a lot of measurements we can use high values of R. On the contrary, when the number of measurements is small, we need to choose a smaller R. For our purpose, values between $R = 10$ and $R = 20$ are correct. Nevertheless, a balance between confidence of the filter and the number of measurements available has to be established for each new case.

Parameter estimation is essential to model a patient-specific heart. The present method can be used to determine other parameters of the electrical model and it can be extended to estimate parameters in the mechanical equations of the heart. However, cases with high dispersion on geometry and parameters require a more robust strategy (Sermesant et al., 2012, 2006).

5.2 Characterization of the cardiac tissue in a human LV geometry

In this section, we use an alternative methodology to characterize the parameters of the cardiac model. Particularly, we focus on the characterization of the mechanical deformation of the muscle.

Up to date, there is a lack of personalised data on fiber orientation. Fully 3D acquisition and reconstruction of the cardiac architecture through DT-MRI require long times and are hard to obtain. Consequently, a few cardiac models include the anatomical and the fiber description coming from the same geometry. In most cases, transmural heterogeneity of the fiber field across the wall is described mathematically, interpolating fiber directions from the epicardium to the endocardium by using surface distance functions. Based on measurements by Streeter et al. (1969), fibers are embedded in the cardiac geometry interpolating their direction from $-\theta$ on the epicardium to 0 at mid-wall to $+\theta$ on the endocardium, where the standard value is $\theta = 60°$.

To investigate the relevance of the fiber orientation in the deformation of the heart, we present an inverse study, combining knowledge coming from various disciplines including anatomy and biomechanics. The work assesses how the cardiac material properties change for different fiber field configurations.
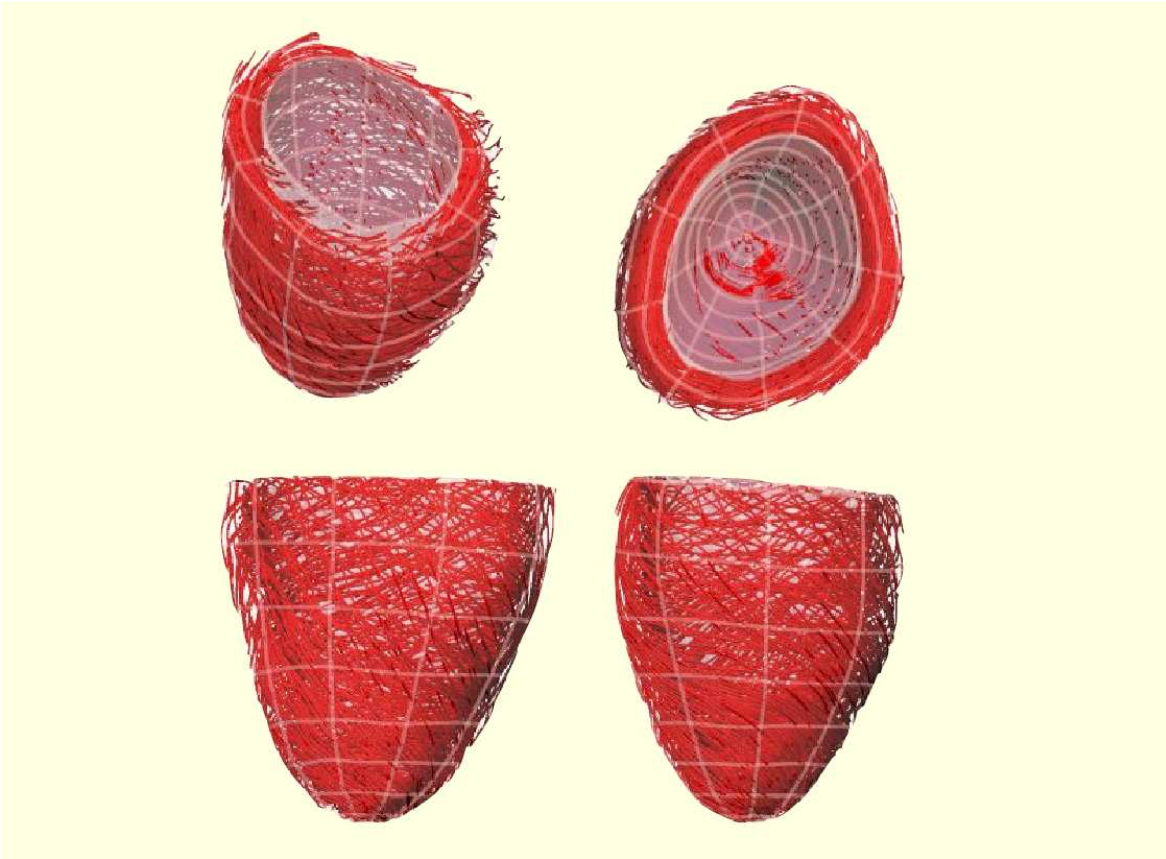
Figure 5.7: Human LV and experimental fiber field extracted in vivo with DT-MRI. From King's College of London.

5.2.1   Methods

To perform the mechanical simulations, the cardiac geometry and the fiber field are required. In this work, a human LV geometry is obtained from MRI images and cardiac human fibers are captured in vivo DT-MRI at King's College of London (KCL). The human LV and the experimental cardiac fibers are shown in Figure 5.7.

Firstly, the end systolic frame is segmented. The volume mesh is built using an approach developed by Lamata et al. (2011). The method uses medical image registration and a cubic-Hermite warping technique to fit a template mesh to a given geometry. The mesh, with 12 elements and 436 nodal positions, provides a continuous representation of the cavity.

Secondly, human fibers are captured in vivo DT-MRI through a novel technique developed by Toussaint et al. (2013) and integrated in the human LV geometry. In addition, a variety of mathematical fiber fields are prepared to interpolate in the LV geometry. Rule-based synthetic fibers with transmural heterogeneity are computed,

choosing different values of the interpolation angle θ. To study the difference in contraction, we explore the interpolation angles $0°$, $\pm 30°$, $\pm 60°$, $\pm 90°$ and we compare results with the simulation obtained using the in-vivo DT-MRI fibers.

Finally, to evaluate the difference in contraction obtained using the rule-based fiber models and the experimental DT-MRI fiber field, we build a functional. The shape of the functional gives information about the sensitivity of the model to changes in the fiber orientation and the minimum of the objective function localizes the set of parameters that best fit the reference.

Material constitutive law.   Focusing on the mechanical properties of the muscle, myocardium is modeled as transversely isotropic hyperelastic material. In this work, the mechanical behaviour of the cardiac tissue is described with a constitutive law that isolates the passive component of the stress, introduced by Guccione et al. (1991). The reason of modeling the heart as a passive material is to simplify the situation and reduce uncertainties of the inverse problem. With this approach, the fundamental properties of the constitutive law are limited and the number of parameters are decreased. This formulation does not consider the active term and reproduces the mechanical properties of the stress-free material with four parameters:

$$
\begin{aligned}
W &= C_1(e^Q - 1) \\
Q &= C_2 E_{ff}^2 + C_3(E_{ss}^2 + E_{nn}^2 + 2E_{sn}^2) + C_4(2Efs^2 + 2E_{fn}^2)
\end{aligned}
\tag{5.11}
$$

where W is the strain energy density function, C_1, C_2, C_3, C_4 are the constitutive parameters and E_{ij} is the Green-Lagrange strain in sheet / normal / fiber direction. Particularly, C_2 represents the stiffness in the myocardium fiber direction (Costa et al., 2001). In order to describe the material properties, the constitutive parameters are reparameterized into C_1, α, r_3 and r_4, as in Xi et al. (2012):

$$
\begin{aligned}
\alpha &= C_1 + C_2 + C_3 \\
r_3 &= C_3/\alpha \\
r_4 &= C_4/\alpha
\end{aligned}
\tag{5.12}
$$

where r_2, r_3, r_4 are the anisotropies of C_2, C_3, C_4 and fulfill that:
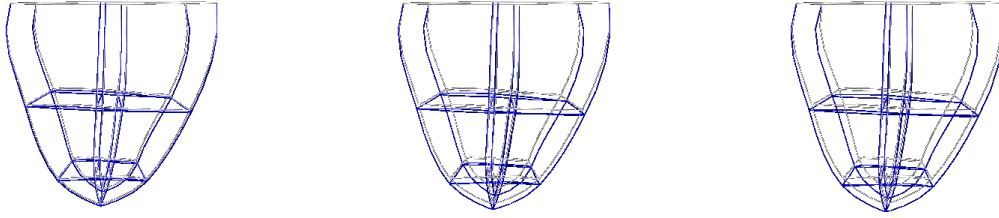
$$
r_2 + r_3 + r_4 = 1
\tag{5.13}
$$

Figure 5.8: Passive inflation of LV.

With this reformulation, the material properties can be split in two parts:

- $C_1 - \alpha$ space: It is related with bulk stiffness. Linear terms of W are considered in C_1 value. Meanwhile, α refers to the exponential terms of the strain-energy function.

- $r_3 - r_4$ space: It is related with the anisotropy of the myocardial structure, which indicates the relative stiffness along the myofiber compared to other material directions.

Computational model. The solid mechanical model is implemented in *Cheart*, the simulation code developed and supported at KCL. The LV is fixed at the base on its epicardium nodes and the apex is free to move. Pressure is applied as a boundary condition on the endocardium of the cubic-Hermite mesh with a quasi-static loading, increasing from a minimum of 0 kPa to a maximum of 1.5 kPa. The quasi-static finite-elasticity formulation is denoted in the Lagrangian frame as described in McCormick et al. (2013) and the stress equilibrium governing equation is solved using the finite element method as explained in Nordsletten et al. (2011). Figure 5.8 represents the passive inflation performed in the LV.

5.2.2   Parameter estimation framework

To determine the values that produce a movement of the LV geometry that is consistent with experimental observations, parameter estimation techniques are often used. In this work, we present a methodology to scope the relevance of the fiber architecture in the deformation of the LV.

The aim is to investigate how a change in the fiber orientation might bias the estimation of material parameters. To study their influence in the resultant movement of the ventricle, a set of passive inflation simulations are performed in the human LV geometry, changing the fiber field that has been interpolated in the geometry and the C_i parameters from the Guccione law. Notice that in the passive constitutive law, multiple combination of values C_1, C_2, C_3, C_4 are able to reproduce similar cardiac state. Despite the complexity of determining constitutive parameters in the inverse problem, this 4-parameter law makes the estimation practicable.

To design the problem, we need the following ingredients:

1) Ground-truth. The simulation of the passive inflation of the LV performed with the human fiber field obtained from in-vivo DT-MRI is established as the reference or ground-truth. The constitutive parameters are chosen based on previous results on a healthy case, published by Xi et al. (2012) and listed in Table 5.1.

C_1 (kPa)	C_2	C_3	C_4
1	19.13	10.67	12.76

Table 5.1: Constitutive parameters of the Guccione law for a healthy case. This values have been used to generate the ground-truth.

2) Rule-based fiber field orientations. A variety of simulations are performed in the human LV cavity using different mathematical descriptions of the cardiac fibers. We explore different fiber fields, which have a linear variation across the wall, from $-\theta$ degrees in the epicardium to θ degrees in the endocardium ($\theta = 0°, \pm 30°, \pm 60°, \pm 90°$). For each fiber field interpolation, simulations are generated by changing C_i values in the Guccione law.

3) Functional to minimize. For each fiber field distribution, the constitutive parameters that best fit the reference movement of the LV minimize the difference between the ground-truth and the simulation obtained with the rule-based fibers. In this work, the difference is evaluated with a functional at the end-diastolic frame, measuring the averaged distance between equivalent Gauss point of the reference and simulated meshes at a certain time point. The functional is defined as the objective function J:

$$J(x, y) = \sqrt{\frac{1}{G} \sum_g |x_g - y_g|^2} \qquad (5.14)$$

where g is the number of Gauss points per element and x_g, y_g are the coordinates of the reference and the simulation respectively. The averaged distance J is calculated between each simulation and the ground-truth at end-diastolic time step.

5.2.3   Simulation set-up

The sensitivity of the fiber orientation in the estimation of material parameters is tested through a set of passive inflation simulations performed in the human LV geometry. First, the reference is established. Then, simulations of the passive filling of the human LV are performed for different sets of C_i values and the variety of fiber field orientations that are interpolated in the geometry. Following the *Forward Models* presented in Table 5.2, data assimilation is applied in a each case.

For each rule-based fiber field Do

1. *Forward Model A*: Fixing C_3 and C_4 on the reference values, compute the simulations to explore $C_1 - \alpha$ space.

   (a) Find the optimal point for each fiber field in $C_1 - \alpha$ space.
   (b) Calculate the hessian at the optimal point
   (c) Calculate the bias

2. *Forward Model B*: Fixing C_1 and α on the reference values, compute the simulations to explore explore $r_3 - r_4$ space.

End Do

Table 5.2: General algorithm to solve the inverse problem.

Notice that in this study parameters are not estimated by optimisation. The combination of parameters that best fit the reference is achieved by minimizing the difference between the reference and the simulation model. In order to understand the impact of fiber orientation in the problem, an exploration of the values of the functional is performed, measuring the similarity between the observation and the simulation. For each case, the functional J presented above is evaluated to draw the $C_1 - \alpha$ and $r3 - r4$ landscapes. With this 'brute-force' data assimilation approach, the location of the global minimum is found at each $C_1 - \alpha$ and $r3 - r4$ spaces. Finally, the bias and the hessian are calculated to characterise the curvature of J at the critical point.

We expect that the functional obtained from a model with the best identifiable fibers yields to the highest hessian value. Therefore, if a simulation is performed with a fiber field that is far from the reference, the hessian value decreases and the optimal value changes (a bias is introduced).

5.2.4   Results

In this section we present the results of the inverse problem to study the sensitivity to the fiber field in the passive inflation of the human LV. The reference or ground-truth has been performed using the theoretical values from Table 5.1 and considering the DT-MRI human fiber field obtained in-vivo. For each rule-based fiber field, the general algorithm from Table 5.2 is performed. To determine the values of the Guccione law that produce a behavior consistent with the reference, we explore the functional introduced in Equation 5.14. First, the $C_1 - \alpha$ landscape is obtained performing passive inflation simulations, holding the C_3 and C_4 parameters to the theoretical values. With this method, we explore the combinations of C_1 and α parameters for a given fiber field.

Results are shown in Figure 5.9, where the objective function is plotted in the $C_1 - \alpha$ parameter space for all the mathematical descriptions of the fiber field ($\theta = 0°, \pm 30°, \pm 60°, \pm 90°$). Numerical results are summarized in Table 5.3. In the figure, the reference behaviour is also drawn, named DT-MRI. On the one hand, yellow dots show the position of the theoretical values listed in Table 5.1 and red dots show the minimum of the functional found for each rule-based fiber field. The reference corresponds to the result obtained with the experimental human fibers, which gives $C_1 = 1$ kPa and $\alpha = 42.56$. On the other hand, the closeness of the contour lines indicates the rapid increase of the objective function, away from the minimum. It can be seen that there is only one minimum at each space, giving the assurance of unique values. Notice that the parameters in the Guccione law are coupled between them. Therefore, an increase of C_1 can be compensated by a decrease of C_2, C_3, C_4 (Xi et al., 2011). The coupling relationship can be visualized in the figure, represented as the dark blue valley. The first graphic (*Angle 0*), corresponds to the simulations where the interpolation angle of the fiber field is $\theta = 0°$. In order to have a behavior similar to the reference (DT-MRI), we observe that a change in the interpolation angle makes a change in the constitutive parameter values. In this case, the minimum value of C_1 is localized at 1.1 kPa and $\alpha = 38.43$. For $\theta = 0°$, we observe the minimum of J yields to an increase of C_1 and a decrease of C_2, compared with the ground truth. Consequently,

the change of the fiber orientation produces a decrease of the stiffness (C_2 parameter) in this case.
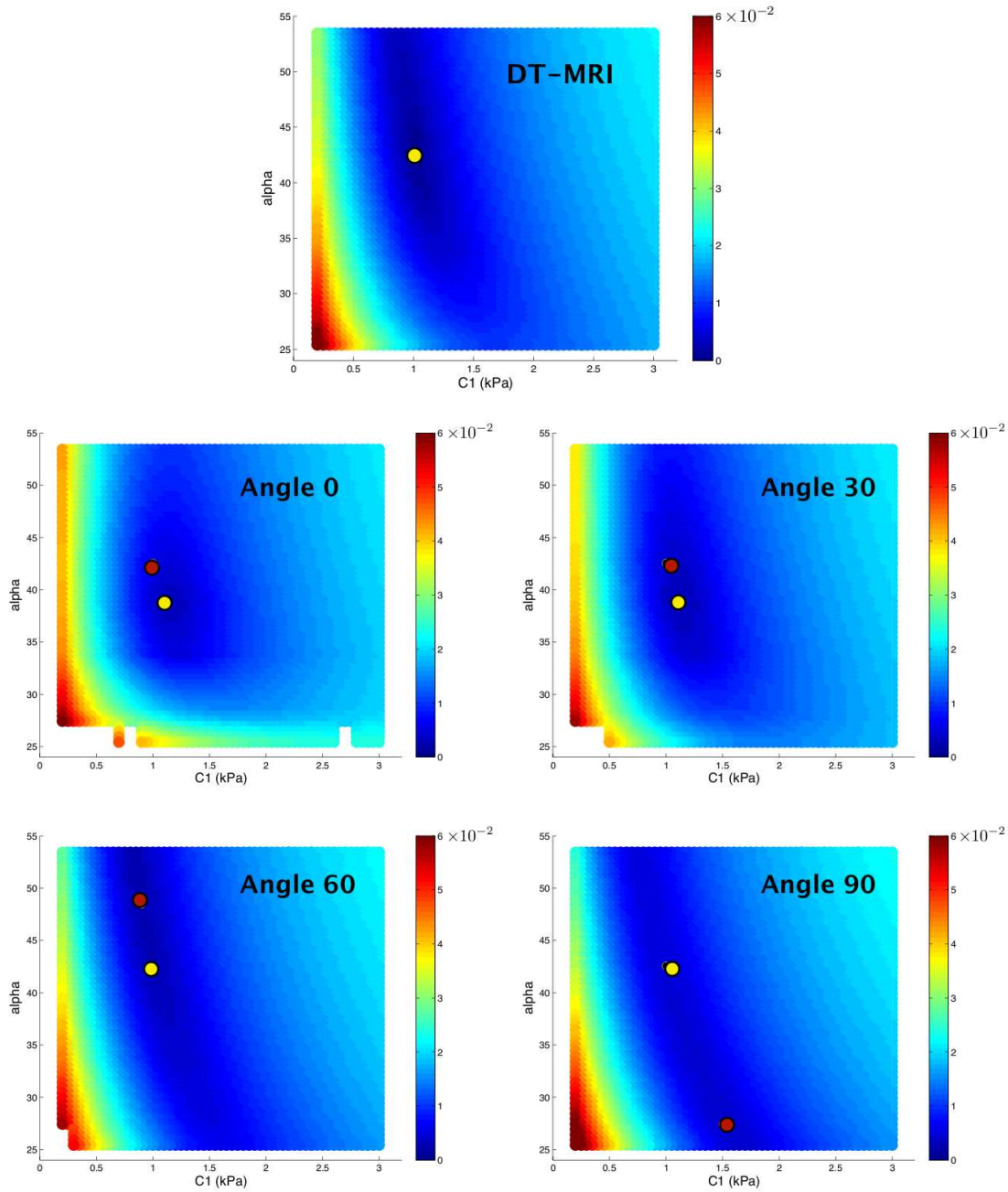

Figure 5.9: $C_1 - \alpha$ landscape of the functional. Yellow dot: Ground Truth. Red dot: Minimum value of the functional.

Model	$C_1 min$ (kPa)	αmin	*Hessian*	*Bias*
DT-MRI	1	42.56	1.17E-05	0
Angle 0	1.1	38.43	7.51E-07	0.868
Angle 30	1.1	38.43	6.42E-07	0.881
Angle 60	0.9	48.43	1.27E-07	0.912
Angle 90	1.5	27.43	1.55E-06	0.916

Table 5.3: Values of C_1, α obtained from the inverse problem. The hessian and bias are calculated to characterize the minimum.

The same procedure is repeated for other fiber field distributions. In the figure, we observe that simulations obtained with $\theta = 60°$ and $\theta = 90°$ yield to patterns that are close to the experimental one (DT-MRI). In Table 5.3, we observe that angles $\theta = 0°$ and $\theta = 30°$ yield to the same combination of parameters and, therefore, the same stiffness. In both cases, C_1 increases and C_2 decreases compared to the DT-MRI fiber field. On the contrary, $\theta = 60°$ gives the opposite situation. C_1 decreases and C_2 increases compared to the ground truth, increasing the stiffness. Regarding, $\theta = 90°$, results show that this rule-based fiber field yields to a large decrease of the stiffness.

Moreover, the bias and the hessian are calculated for each case, to characterise the curvature of the functional at the critical point. As expected, we observe that the hessian value decreases when the simulation is performed using a fiber field that is different from the reference. The lowest hessian value is obtained for $\theta = 60°$. On the contrary, $\theta = 90°$ has the largest value, which indicates that this rule-based fiber field is closer to the reference.

Similarly, Figure 5.10 presents the objective function in relation to the $r_3 - r_4$ space. In this case, C_1 and α are fixed and we explore combinations of C_3 and C_4. Results show differences between the simulations performed using the human fiber field and the rule-based. Particularly, simulations obtained using $\theta = 30°$ and $\theta = 60°$ yield to a pattern that is closer to the experimental one (DT-MRI). Probably an intermediate angle would give the best combination of C_3 and C_4 parameters.

Finally, Table 5.4 summarizes the sets of parameters of the Guccione law obtained in the inverse study. In order to fit the reference contraction, we observe that different fiber field orientations yield to different constitutive parameters.
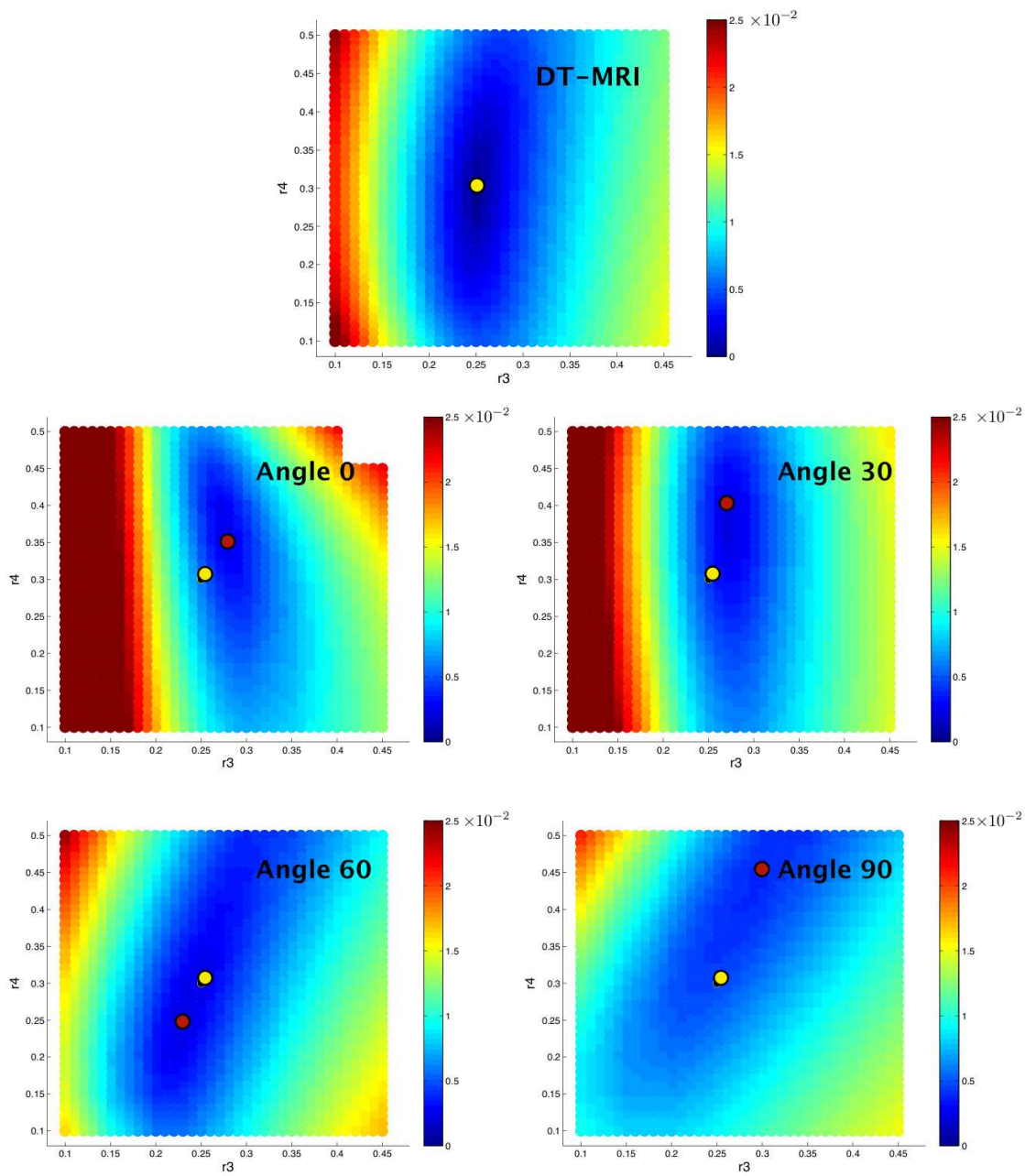
Figure 5.10: $r3 - r4$ landscape of the functional. Yellow dot: Ground Truth. Red dot: Minimum value of the functional.

$Model$	$C_1 min$ (kPa)	$C_2 min$	$C_3 min$	$C_4 min$
DT-MRI	1	19.13	10.64	12.76
Angle 0	1.1	15	11.92	14.89
Angle 30	1.1	15	11.49	17.02
Angle 60	0.9	25	9.79	10.64
Angle 90	1.5	4	12.76	19.15

Table 5.4: Values of C_1, C_2, $C3$ and $C4$ obtained from the inverse problem.

5.2.5 Computational remarks

The code is solved sequentially in an Intel Core i7-3770 CPU 3.40 GHz. One simulation runs in 100 s. For each fiber field distribution, a complete analysis requires 10 hours on a single PC. Since the computational requirements for this study are not excessive, the application of the method is practical. However, the implementation of the inverse problem in a parallel platform would increase the potential of the framework.

5.2.6 Discussion

The definition of myocardial parameters in the governing equations is necessary in cardiac biomechanics. In this section, we have introduced a preliminary work to adjust the mechanical properties of the heart, required for the simulations. Particularly, the framework has been used to study the effect of tissue structure. To scope and develop the method, we have build the framework in a controlled situation. The fiber field orientation has been the only factor that has changed.

Mathematical fibers have been embedded in the cardiac geometry interpolating their direction from $-\theta$ on the epicardium to 0 at mid-wall to $+\theta$ on the endocardium. Simulations of the passive inflation of the cavity have been performed using rule-based fiber fields and have been compared to the reference simulation, obtained with the experimental DT-MRI fiber field. The difference between the reference and the mathematical models has been evaluated with a functional at the end systolic frame. For each case, the model parameters of the constitutive law that best fit the reference have been calculated.

Recently, Carapella et al. (2014) have published a computational study of the impact of tissue microstructure on contraction of the left ventricle in rat. They state that in order to represent the effect of the fiber field on cardiac mechanics, and to have a patient-specific approach, further investigation of the sheet orientation should be carried out. The present work has been performed in-silico, with perfect control on

boundary conditions. We have tested the the sensitivity of the model to the fiber direction, through the evaluation of changes in the location of the minimum in the $C_1 - \alpha$ and $r_3 - r_4$ spaces. At the end systolic frame, results show that for each fiber field orientation, a different combination of parameters yields to a contraction that is close to the reference. Probably, the rule-based fiber model obtained with $\theta = 90°$ has the closest match in this example. However, as described in Carapella et al. (2014), further investigation is necessary to understand the impact of the fiber field orientation on cardiac deformation. Working with real data would increase the challenge, due to the noise in the acquisitions. Finally, the improvement of in-vivo DT-MRI techniques is also crucial, to set the ground truth simulation of the in-silico framework.

Chapter 6

Sensitivity Analysis of the EM Computational Model

This chapter presents a sensitivity analysis study using the cardiac computational modeling (CCM) code based on HPC strategies. Focusing on the electromechanical propagation in the myocardium, the application aims to investigate the effect of initial conditions in the resultant simulation. Particularly, we study the influence of different settings of the heart microstructure in the contraction of the tissue, such as the electrical activation. The analysis is performed in a biventricular geometry, where 14 different activation protocols are tested. In addition, two different fiber field orientations are interpolated in the geometry. The activation protocols and the fiber field descriptions are combined to run a wide spectrum of simulations. For each case, results are evaluated by quantifying the total activation time, ejection fraction and the time of maximal contraction. A total of 52 electromechanical simulations are needed to test all the inputs parameters in this work. One simulation of 600 ms in real time requires about 30 min of wall clock time in 512 processors. Consequently, the complete study requires high computational resources.

Considering the complexity of cardiac models, the sensitivity analysis presented here emphasises the possibility to optimise the cardiac activation protocols by use of the present method. Results presented show that the proposed CCM tool is capable of capturing variations to small input parameter changes.

The results presented in this chapter lead to the article: R. Arís, J. Aguado-Sierra, G. Houzeaux, D. Gil, Agnés Borràs, R. Sebastian and M. Vázquez. Sensitivity Analysis to Initial Stimuli and Fiber Orientation of a Biventricular Electromechanical Computational Model of the Heart. *Submitted.*

6.1   Introduction

The CCM tool is used to simulate a pumping heart, focusing on the EM propagation through the tissue. Working at the organ level, the CCM requires the solution of three components: the electrical signal, computed as a non-linear reaction-diffusion system, the mechanical deformation, which produces the contraction of the heart and the excitation-contraction coupling scheme that links both problems together.

It has been reported that the specific location where the stimuli enters the myocardium, along with the anatomical variations, determine the overall activation sequence of the heart and the epicardial breakthrough of the electrical wave (Durrer et al., 1970). Obtaining an accurate representation of the Purkinje system in the in-vivo heart is a huge challenge still unsolved, and the variability of the Purkinje fiber geometry across and within species is unknown. We aim to understand the effect of modeling various initial stimuli protocols and its resulting electromechanical response. The Purkinje system modeler has been developed by Sebastian et al. at University of Valencia (Sebastian et al., 2013). Each initial stimuli protocol is composed of a set of locations and times determined by the Purkinje tree structure and its PMJs, where the electrical stimuli reach the right or left ventricular myocardium, a magnitude of the stimulus. For this reason, it is necessary to test the sensitivity of the CCM model to different initial stimuli and analyze the importance of the initial activation in the dynamics of the system.

A biventricular geometry is employed to study the sensitivity of the code to different settings of the heart microstructure. Fourteen initial activation protocols and two transmural fiber field interpolations are tested. For each case, simulations are evaluated and analyzed to assess if the variation of the inputs has an impact in the pumping motion of the muscle.

6.2   Computational mesh

To perform the simulations, the rabbit ventricular geometry developed by Bishop et al. (2010) at the University of Oxford is used. The model represents the ventricles of the heart and does not include valves, great vessels, pericardium and organs around the heart. The geometry consists of 432000 linear tetrahedra and 82619 nodes with a resolution of 0.05 cm. An important issue is how to anchor the heart. In this work, myocardium has been fixed in the apex, but only in z (z axis is the apex to base
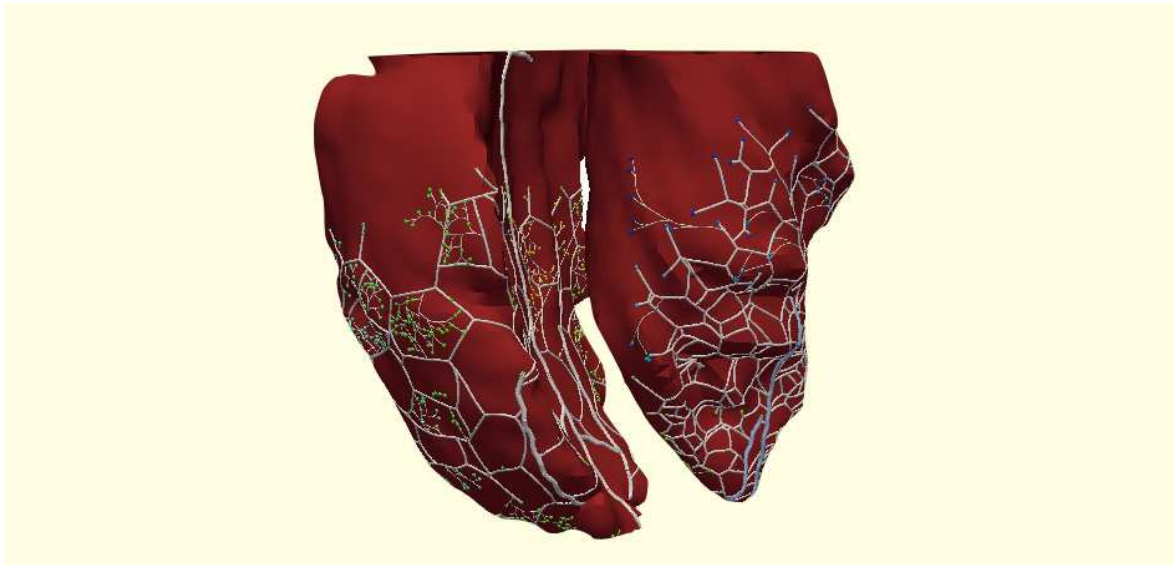
Figure 6.1: Nodes in the endocardium (red), coupled to the Purkinje system tree (white) and PMJs (small spheres), where the electrical propagation is initiated.

direction, or longitudinal direction, in our reference frame). The resultant movement is a rotation of the apex in xy axial plane, i.e. torsion of the heart, and a displacement of the base towards the apex in the longitudinal axis z.

6.2.1 Initial Stimuli

To study the impact of the initial stimuli in the simulations, the ending points of the Purkinje network are supposed as the starting conditions for the coupled EM simulations. 14 different activation protocols have been generated, varying the density of initial stimuli and time of activation Sebastian et al. (2013). For each ventricle, the network has been constructed independently (Figure 6.1 and Table 6.1), being applied at the nodes level in our finite element model.

Considering the number of nodes and the time of activation, we briefly describe the activation protocols as follows:

- Activation protocols 1, 3, 6 and 7 present high density of nodes (> 490) in both ventricles, but different time of activation between them. Activation protocol 2 shows high density of activation in the RV but not on the LV.

- Activation protocols 4, 5 and 8 have low density of nodes (< 379). In addition, the activation in cases 4 and 5 is performed from apex to base.

- Activation protocols 9 to 12 are activated only in the RV, simulating a left ventricular bundle branch block. Each case has different density of activation. Notice that activation protocols 5-12, 8-10 and 7-11 have the same number of stimuli locations in the RV.

- Punctual activations are performed in protocols 13 and 14. Based on the study of Ballester-Rodes et al. (2006), activation protocol 13 is initiated in two nodes in the base (one node in each ventricle) with a delay of 30 ms between them. Finally, Activation protocol 14 is activated in one node in the epicardial surface of the apex. This protocol is commonly used in cardiac simulations, as in Bishop et al. (2009).

Activation Protocol	Nodes RV	Nodes LV	Activation Protocol	Nodes RV	Nodes LV
1	741	714	8	327	151
2	738	178	9	514	0
3	571	758	10	327	0
4	379	145	11	805	0
5	85	90	12	85	0
6	802	720	13	1	1
7	805	490	14	1	

Table 6.1: Number of nodes for each activation protocol in both ventricles.

As can be seen from Table 6.1, the activation protocols have different density of nodes in the ventricles. To compare this, the location of the nodes of the initial stimuli is drawn in Figure 6.2. For each protocol, coordinate z (oriented from apex to base) versus the time of activation is presented. Green color refers to the stimuli located in the LV and red color to the stimuli located in the RV. Notice that most of the protocols activate the Purkinje network within 30-40 ms. Moreover, only activation protocols 4 and 9 take up to 55 ms to complete the initial activation. Finally, the LV is not activated in protocols 9 to 12.

6.2.2 Fiber Field

Since the experimental fiber field is not available for this model, the cardiac fiber orientation is calculated using the rule-based model described in chapter 2. The parameters of this function are chosen to fit the observations of Streeter et al. (1969). The interpolation of the fiber along transmural direction, called helix angle α, is defined as $\alpha = R(1 - 2e)^n$ where $R = \pi/3$ for the LV and $R = \pi/4$ for the RV.
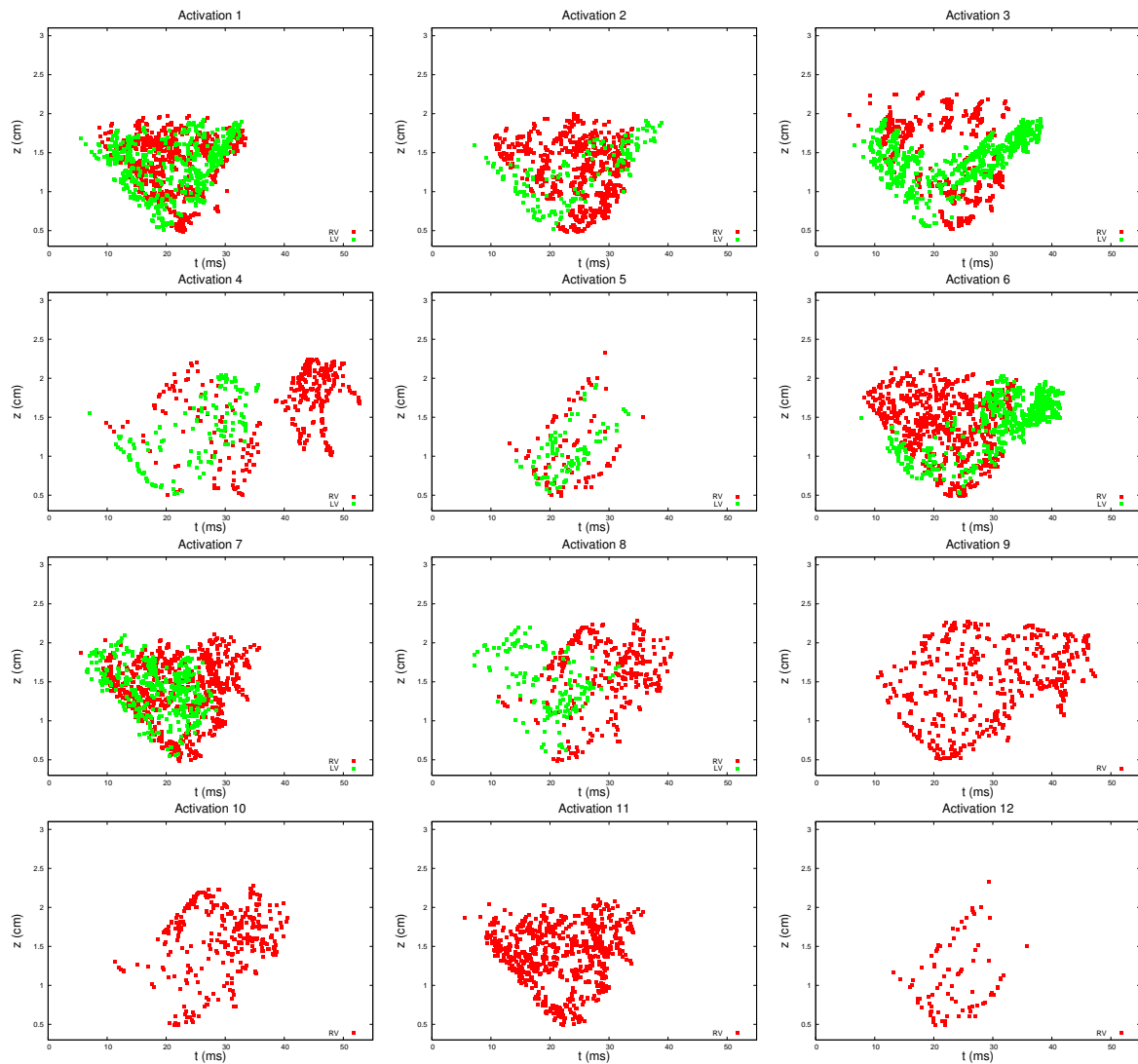
Figure 6.2: Activation of PMJs in the ventricles. Number and location (with respect to the longitudinal axis z) of PMJs activated over time. Clusters of points correspond to PMJs activated at nearly the same time and close to each other. Green color refers to the stimuli in the LV, while the red colored stimuli are located in the RV.

Two different interpolations are produced to study the impact of the transmural rotation in the fiber orientation: linear and cubic, corresponding to $n = 1$ and $n = 3$ values in the formulation.

6.2.3 Measurements: Volume and Ejection Fraction

Ejection fraction represents the volumetric fraction of blood pumped out of the ventricle with each heart beat or cardiac cycle. It can be applied to either the right ventricle or the left ventricle. In a healthy rabbit, ejection fraction of 70% can be considered as normal (Zou et al., 2009). The ejection fraction in this work is approximated to:

$$EjectionFraction(\%) = \frac{MaximumVolume - MinimumVolume}{MinimumVolume} * 100$$

The minimum volume is achieved after cavity contraction.

6.3 Linear rule-based fiber field interpolated in the ventricles

Evolution of the EM wave.   A qualitative analysis of the wavefront at t=45 ms and t=64 ms from the initial activation is shown in Figure 6.3 and Figure 6.4. At these early times, the electromechanical wave has already reached the epicardium in all cases but the total activation of the ventricles is not completed yet. In Figure 6.3, we can observe that different initial stimuli leads to different activation sequence of the heart. The closest match appears between the activation protocols which have the same number of nodes in the activation of the RV, activation protocols 5-12, 8-10 and 7-11. As protocols 10, 11 and 12 are not activated in the LV, the activation is produced by diffusion from the RV and contraction occurs later. Figure 6.4 shows the evolution of the wavefront at t=64 ms. In most of the cases, global patterns of electrical activation are similar. The main differences can be observed in the protocols with low density of nodes that activate the ventricles (activation protocols 5, 12, 13 and 14). On the contrary, mechanical contraction is different in almost all situations. Some similarities can be found between activation protocols 1-6-7, for example, which have high density of nodes in the RV and similar sequence of activation.
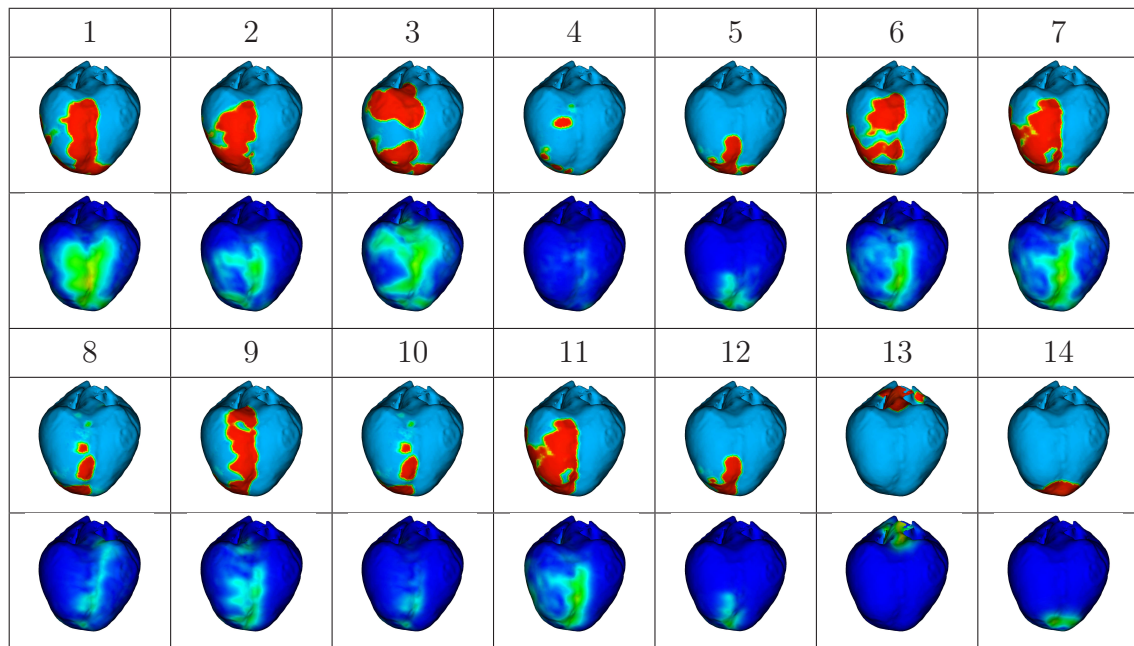
Figure 6.3: Anterior view of the ventricles. Simulation of the electrical and mechanical components of the EM wave propagating at t=45 ms for each activation protocol. ST1 fiber field interpolated in the geometry. Red coloured areas in the first row correspond to the electrical component of the EM wave. In the second row, we present the biventricular deformation of the tissue.
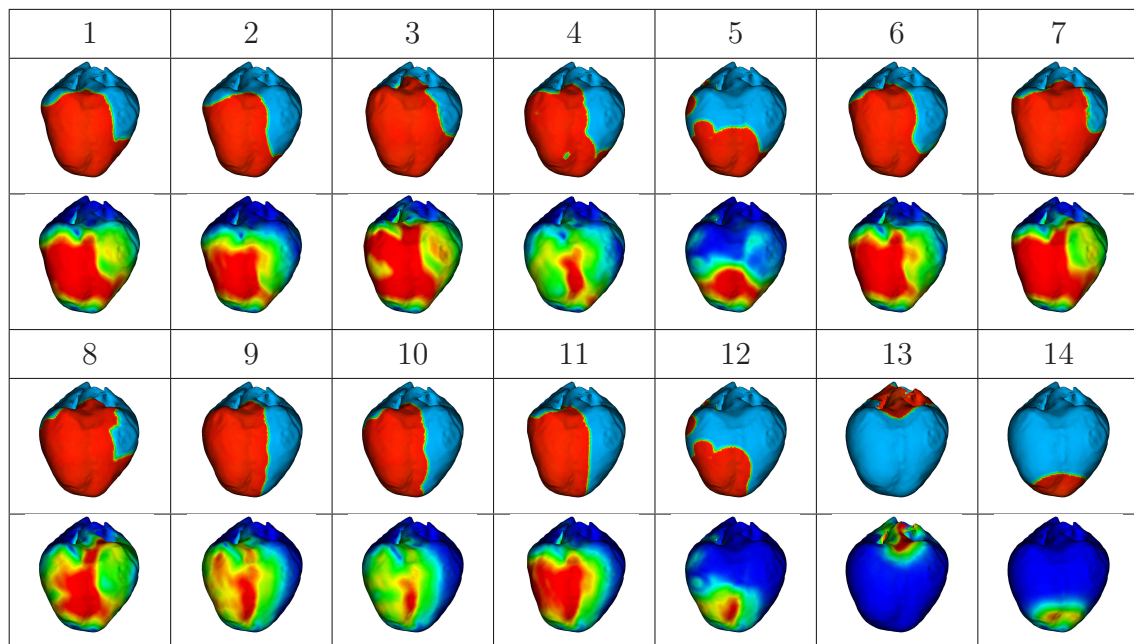

Figure 6.4: Evolution of the EM wave at t=64 ms. First row corresponds to the electrical component of the EM wave. The second row represents the deformation of the tissue.

Activation Protocol	1	2	3	4	5	6	7
Breakthrough	1	0.96	1	1.15	0.73	0.92	0.77
	post mid	ant inf	ant sup	post inf	post inf	post mid	post mid
Maximal Contraction	3	3.26	3	3.58	3.5	3	2.85
Total Activation	4.31	4.5	4.15	4.54	4.54	4.19	4.08
EF (%)	71.4	73.6	69.5	66.6	70.8	68.9	70.3
Activation protocol	8	9	10	11	12	13	14
Breakthrough	0.92	0.85	0.88	0.77	0.73		
	post inf	post inf	post inf	post mid	post inf		
Maximal Contraction	3.38	4.96	5.08	4.85	5.12	8.81	6.85
Total Activation	4.31	5.12	5.19	5	5.31	7.62	8.23
EF (%)	67.7	58	57.2	57.9	58.7	57.3	77

Table 6.2: Normalized times of breakthrough, total activation (electrical component of the EM wave), maximal contraction and ejection fraction of the ventricles. The area where the activation first appears in the epicardium is described as anterior (ant), posterior (post), inferior (inf), middle (mid), superior (sup).

Epicardial Breakthrough. The major advance of the EM wave through the myocardium is studied for each activation protocol. Table 6.2 shows the time and the location where the EM wave first reach the epicardium. Notice that times have been normalized to a reference, which is the time of breakthrough in protocol 1. Moreover, activation protocols 13 and 14 are not included in this analysis because the nodes of activation are close to the epicardium.

From the simulations, we observe that the epicardial activation first arises at the posterior part of the ventricles in most of the activation protocols. Only activation protocols 2 and 3 have a different behavior and the epicardial breakthrough is in the anterior part. Furthermore, the major advance is generally found in the middle or the inferior site of the ventricles. The exception is protocol 3, which first activates the basal part of the epicardium. As in the case of the evolution of the EM wave presented above, the closest match exists between protocols 5-12, 8-10 and 7-11 because they have the same activation in the RV.

Maximal contraction. The time of maximal contraction of the cavity is approximated to the time of the minimum volume inside the ventricles. Table 6.2 shows the results for each activation protocol. As can be seen from the table, protocols 2, 4, 5 and 8 present an increase of the time of maximal contraction compared to the

reference (protocol 1). The reason of this change can be a decrease in the left ventricular activation density, see Figure 6.2. In all these cases, the nodes that activate the LV are spread. The same occurs with protocols 9 to 12, which have no activation in the LV. Probably, low (or zero) density in the nodes of activation of the LV extends the time to reach the maximal contraction. Moreover, the largest time of maximum contraction is given by activation protocol 13, where the stimulus is initiated at two nodes in the base of the ventricles.

Although the time to reach the minimum volume inside the cavity is different in all activation protocols, in most cases the mechanical pattern is very similar, see Figure 6.5. Only activation protocols 13 and 14 show a shape in the base which deviates from the average. The mechanical pattern at the beginning of the propagation varies between the activation protocols but at maximum contraction the protocols present a similar contraction.
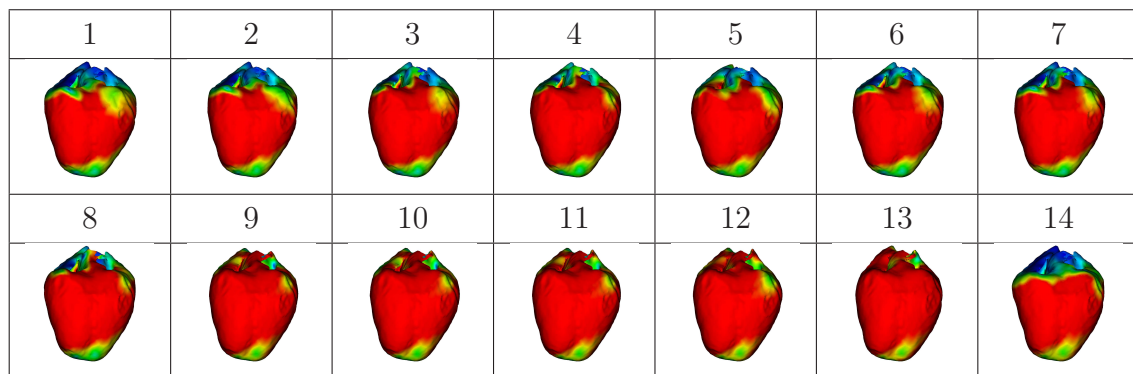
Figure 6.5: Time of maximal contraction for each activation protocol. Colours represent the displacement.

Total Activation. The ventricles are totally activated when the electrical component of the EM wave spreads through all the cardiac tissue. As can be seen in Table 6.2, activation protocols which have low density or have no activation in the LV (protocols 2, 4, 5, 8 and 9-12) increase the total activation time, compared to protocol 1.

Furthermore, most of the cases reach the total activation of the cavities after the time of maximal contraction. However, activation protocol 13, which has two initial stimuli in the base of the ventricles, has a different behavior. In this activation protocol, the total activation in the cavity is captured first and the time of maximal contraction is obtained later.
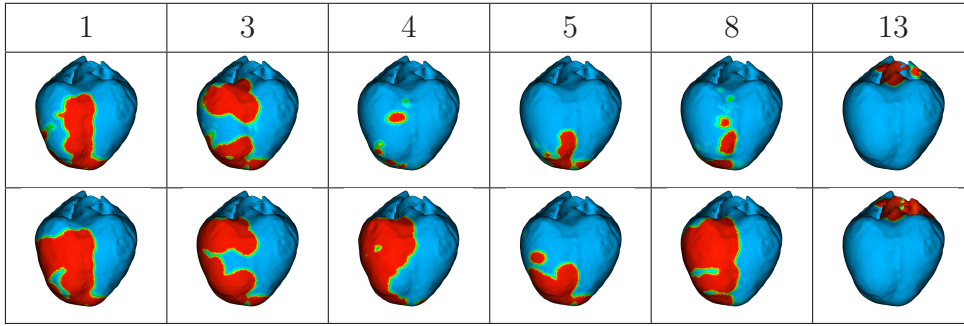
1	3	4	5	8	13

Figure 6.6: Electrical component of the EM activation at t=45 ms for each activation protocol. Top: Activation protocols activated in a period of 55 ms. Bottom: Activation protocols with synchronous activation.

Ejection Fraction.   We calculate the ejection fraction rate in the LV cavity. Results are presented in Table 6.2. Notice that activation protocols 1 to 8 present values close to 70%, with 5% of variability. However, activation protocols which have no initial stimuli on the LV (protocols from 9 to 12) have this value reduced by 18%. The same result is obtained in activation protocol 13, which is activated only at the base. Finally, the maximum EF value, 77%, is reached in activation protocol 14, where the initial activation is located in one node in the epicardial surface of the apex.

6.3.1   Influence of the time-sequence in the activation of the EM wave

Previous results have been performed using different activation protocols. The purpose of this section is to study how the temporal sequence of activation affects the propagation of the EM wave through the cardiac tissue. In this process, we choose some of the activation protocols from Table 6.1 and we proceed to stimulate all the nodes of each protocol at the same time, to establish a synchronous activation of the models.

In Figure 6.6, qualitative differences can be observed at the beginning of the propagation for the two time-sequences. However, Table 6.3 shows that at time of maximal contraction results obtained with the protocols activated synchronously and non-synchronously are very similar. In addition, the deformation patterns present no discrepancies in the simulation. It is worth to mention that synchronous activation protocols tend to reach the maximal contraction slightly earlier than non-synchronous cases, but differences are not significant. Regarding the total activation, times between synchronous and non-synchronous protocols are similar too. Finally, ejection fraction

rate of the LV is also calculated for synchronous and non-synchronous activations. We observe that the rate increases in the synchronous cases, achieving values up to 2.5 % larger than the non-synchronous cases.

Maximal Contraction						
Protocol	1	3	4	5	8	13
Non-Sync	3	3	3.58	3.5	3.38	8.81
Sync	3	2.88	3.54	3.5	3.31	8.73

Total Activation						
Protocol	1	3	4	5	8	13
Non-Sync	4.31	4.15	4.54	4.54	4.31	7.62
Sync	4.31	4.08	4.54	4.58	4.38	7.42

EF (%)						
Protocol	1	3	4	5	8	13
Non-Sync	71.4	69.5	66.6	70.8	67.7	57.3
Sync	72.2	71.9	66.6	71.5	68.5	58.8

Table 6.3: Times of maximal contraction and total activation normalized to protocol 1. Value of ejection fraction for protocols activated non-synchronously and synchronously.

6.3.2 Density of activation

In order to study how the density of nodes in the initial activation influences the resultant movement of the heart, we reduce the number of stimuli in protocol number 1 homogeneously. From each two nodes in the activation system we choose one, and we obtain half of the density, maintaining the temporal activation of each node. The simulation performed with the modified activation protocol gives similar results compared to the original, see Table 6.4. Times of maximal contraction and total activation are equivalent. We only observe that ejection fraction decreases 0.1 % when we reduce the density by half. Furthermore, we test the synchronous activation in the new set. If we compare the results with the non-synchronous simulations, we observe that if the density of nodes decreases and the activation is synchronous, the resultant ejection fraction increases 1.5 %, see Figure 6.7. This result agrees the previous section: the ejection fraction rate increases in the synchronous cases.

Maximal Contraction		
Protocol	1	Modified 1
Non-Sync	3	3.27
Sync	3	3.08

Total Activation		
Protocol	1	Modified 1
Non-Sync	4.31	4.35
Sync	4.27	4.31

EF (%)		
Protocol	1	Modified 1
Non-Sync	71.4	71.3
Sync	72.2	72.8

Table 6.4: Normalized times of maximal contraction and total activation for protocol 1 and modified protocol 1, where the density is reduced to half of the nodes. Synchronous and non-synchronous results are presented.
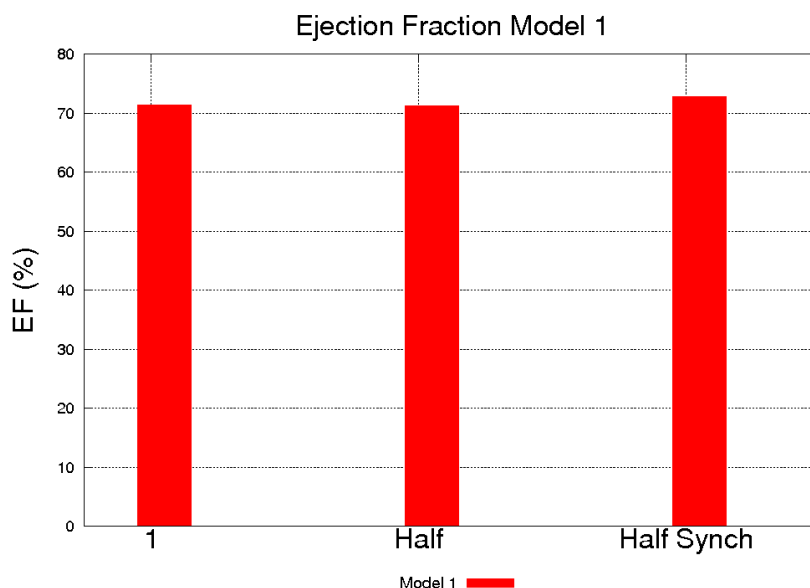
Figure 6.7: Ejection fraction results. Left: activation protocol 1. Middle: activation protocol 1 modified (the activation is reduced to half of the nodes). Right: activation protocol 1 modified with synchronous activation.

6.4   Cubic rule-based fiber field interpolated in the ventricles

In this section, we use cubic rule-based fiber vectors interpolated in the geometry to perform new simulations. All the activation protocols are tested. Results are compared to simulations presented above, obtained with the linear interpolation of the fibers.

At the early state of t=45 ms, there are no remarkable differences between the simulations using linear (ST1) or cubic (ST3) distributions. However, at time of maximal contraction, linear and cubic cases present a different behavior, see Table 6.5. In almost all cubic cases, the maximal contraction is reached earlier than the linear result. Only activation protocols 13 and 14 reach the maximal contraction first in the linear case. Notice that all protocols present an important variation of the maximal contraction time when changing the fiber field model. Specially activations 13 and 14, which have the largest response.

Regarding the total activation of the ventricles, we observe that the cubic interpolation of the cardiac fibers leads to larger times in protocols 1 to 8 and 13 to 14. Only protocols 9 to 12, which are not initially activated in the LV, reach the total activation earlier than the linear case. Notice that discrepancies in total activation times between the fiber field models are remarkable in almost all cases.
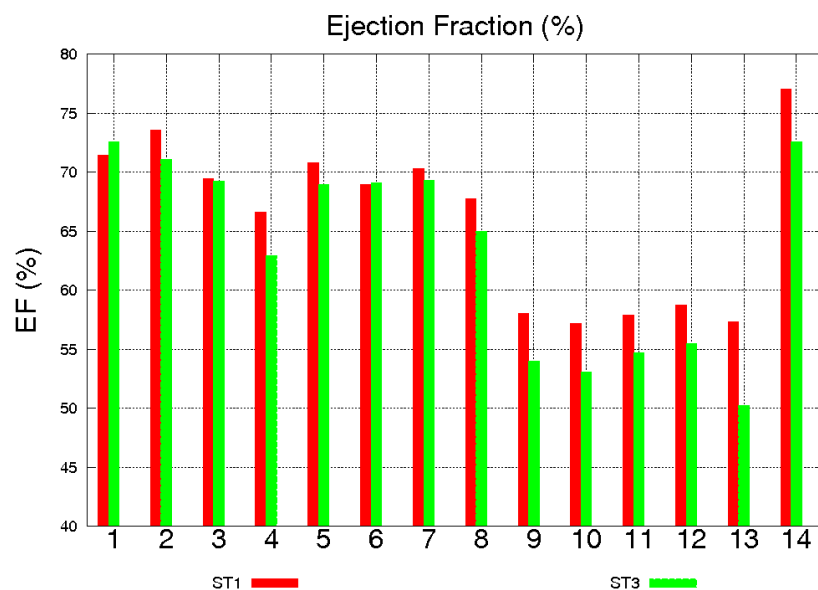
Figure 6.8: Ejection fraction results using two different fiber field models in the EM simulation. ST1 corresponds to a linear interpolation of the cardiac fibers and ST3 a cubic interpolation of the fibers.

Finally, ejection fraction values are presented in Table 6.5. In general, the cubic rule-based model predicts a lower ejection rate than the linear, with a variability lower that 1.5 %. The maximum difference rises up to 7 % in activation protocols 13 and 14. Figure 6.8 shows the comparison of all the results.

	Maximal Contraction													
Protocol	1	2	3	4	5	6	7	8	9	10	11	12	13	14
ST1	3	3.26	3	3.58	3.5	3	2.85	3.38	4.96	5.08	4.85	5.12	8.81	6.85
ST3	2.85	3.27	2.81	3.35	3.31	2.85	2.73	3.23	4.69	4.85	4.58	4.88	9.31	7.27
	Total Activation													
Protocol	1	2	3	4	5	6	7	8	9	10	11	12	13	14
ST1	4.31	4.5	4.15	4.54	4.54	4.19	4.08	4.31	5.12	5.19	5	5.31	7.62	8.23
ST3	4.54	4.77	4.31	4.62	4.62	4.35	4.31	4.31	5.04	5.08	4.92	5.23	8.31	8.92

Table 6.5: Normalized times of maximal contraction and using linear (ST1) and cubic (ST3) rule-based fiber fields.

Quantification of the variability in the contraction of the tissue. At the time of maximal contraction, the cardiac tissue presents areas of mismatch at the base and also at the apex when varying the fiber field. To quantify the variability, we divide the

geometry in 7 zones and we calculate the difference between the deformation of the tissue obtained with linear and cubic fiber field models. For each region, we normalize the resultant value to the number of nodes of the zone.

Figure 6.9 (left) shows the normalized difference versus the time. Zone 1 corresponds to the apex and zone 7 corresponds to the base of the ventricles. As can be observed in the figure, zones 2 to 6 are distributed between these two sections. On the right side of the figure, the normalized difference of the deformation of the tissue is plotted. We observe that the major differences in contraction between the fiber field models are produced in zones 6 and 7, which are close to the base. It is apparent that the rule-based linear model and the cubic one predict a different movement in the myocardium, specially in this area.

6.5   Computational Remark: Parallel efficiency for the coupled EM model

The simulations of the present work are performed in the Spanish supercomputer Marenostrum III. A total of 52 EM simulations have been needed to test all the input parameters in the geometry. Each cardiac simulation of 600 ms requires about 30 min of computation in 512 MPI processors. The typical wall clock figures in Marenostrum is a few minutes. As the scalability is very linear, we usually use the average value of FEM elements per MPI task to have a rough estimate of the wall clock time.

Figure 6.10 shows Alya strong scalability solving a coupled electromechanical problem in a distributed memory cluster. The code was compiled using the Intel Fortran Compiler in Marenostrum. The tests were carried out up to 8000 cores for a special mesh of 27.6 millions non-structured tetrahedra (4.8 millions nodes), which comes from a refinement of the rabbit ventricular geometry from the University of Oxford. After 10000 elements-per-core, it is noticeable a progressive degradation of linear scalability due to communication. To simulate 1 second of real time, the wall clock time in Marenostrum is approximately 10-15 minutes. Depending on the electrophysiology model used (FHN or TT) this time could vary around 20 - 30 %.
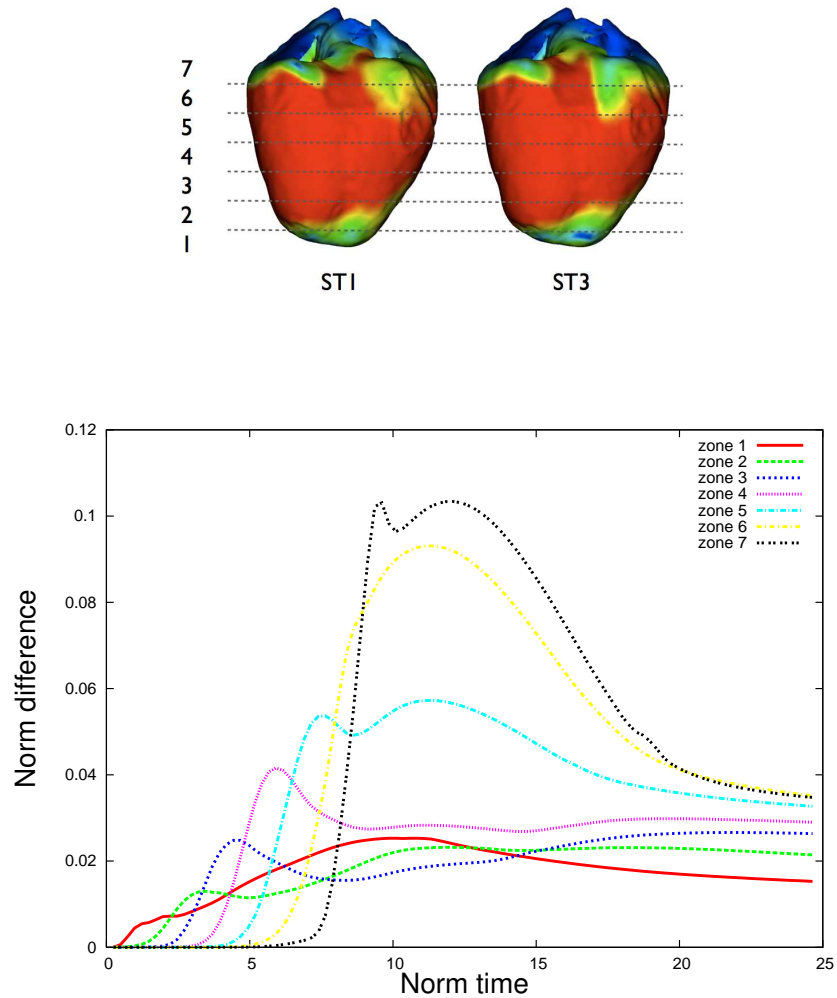
Figure 6.9: Displacement of the cardiac geometry using linear (ST1) or cubic (ST3) interpolation of the fiber field and activation protocol 1. For each zone, the graphic shows the normalized difference versus time.
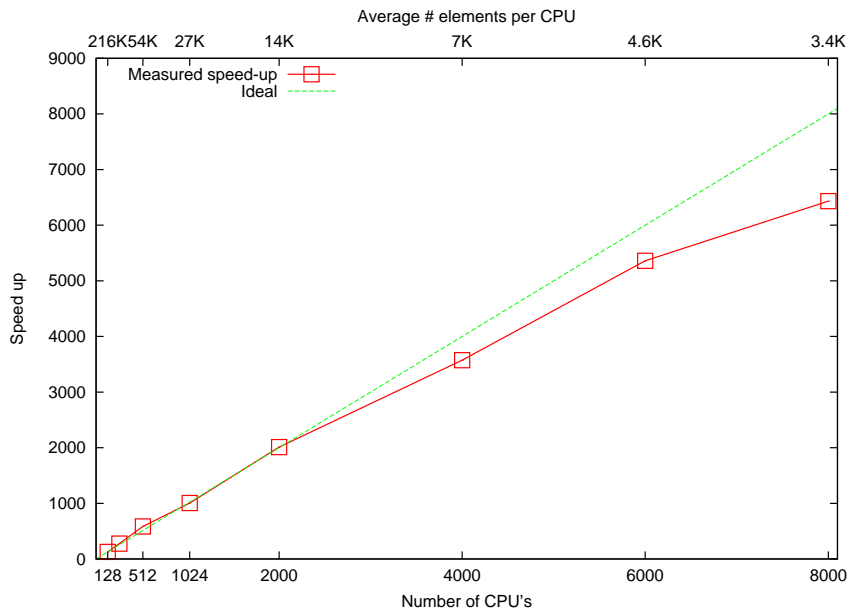
Figure 6.10: Strong scalability for the coupled electro-mechanical problem, compared with the ideal linear scalability. The vertical axis shows the speedup, the lower horizontal axis is the number of cores and the upper horizontal axis is the elements-per-core average. Tests were carried out in Marenostrum III supercomputer.

6.6   Discussion

Results presented in this chapter show that the proposed cardiac computational model of the heart is capable of capturing variations to small input parameter changes. We focus on the EM propagation in the cardiac tissue. The activation of the system is performed using 14 activation protocols that stimulates the electromechanical wave. Also, linear and cubic rule-based models have been tested in the computational problem. We study the propagation dynamics throughout the volume of the ventricles giving measures like ejection fraction and times of contraction.

Despite the propagation of the EM wave has a different activation sequence, at early stage (t=64 ms) the simulations performed using 14 activation protocols present a close match in almost all cases. Only activation protocols 13 and 14, which are activated in one or two nodes, show different results. At the time of maximal contraction, we observe that low density of nodes in the activation of the LV leads to similar electrical and mechanical patterns. However, times are extended in these cases, compared to other activation sequences. The same behavior can be observed in the total activation. Times are larger when the initial activation of the LV is produced with low or zero density of nodes. Moreover, ejection fraction rate presents up to 4 % of variability between

activation protocols. The value is reduced in activation protocols which have no initial stimuli on the LV, achieving differences up to 18 %.

To study the influence of the time-sequence in the EM activation, some of the protocols have been stimulated at the same time and a synchronous activation of the models has been established. Results show that the time-sequence does not seem to affect the morphology of the activation. Despite we observe that activation protocols activated synchronously reach the maximal contraction slightly earlier than non-synchronous cases, differences are low. We can assume that time-sequence does not affect the maximal contraction and total activation times. Regarding the ejection fraction rate, we observe that it increases in the synchronous cases, but the variability is less than 1.5 %. Furthermore, if we reduce homogeneously the density of nodes in both ventricles, results are practically not affected.

Depending on the model, the fiber orientation makes a difference in the simulations. As prompted by some authors, the fiber model has a great influence in contraction Gil et al. (2013); Carreras et al. (2006); Poveda et al. (2012). In this work, the relation observed in the linear case between the activation protocols is maintained in the cubic case. Besides differences between activating protocols, the new fiber model presents discrepancies up to 6% compared to the linear case in times of maximal contraction. Regarding the ejection fraction, the cubic rule-based model predicts rates 3% lower in average than the linear model. Finally, through a quantification of the variability in the contraction of the tissue, we observe that linear and cubic rule-based models predict a different movement in the myocardium, specially in the base.

In conclusion, results presented in this work show that the result of a simulation of the cardiac contraction depends on two factors: the geometrical location of the initial stimuli and the travel of the EM wave through the cardiac fibers. Probably, the fiber field orientation interpolated in the cardiac model, plays the most significant role in the simulations. Differences in the density of the stimulated nodes that first excite must be very large to really account for changes in the ventricles contractile action. Moreover, time sequence have low influence in the simulations. If the non-synchronous sequence is unavailable, a synchronous activation is sufficient and leads to acceptable results.

Considering the complexity of cardiac models, the sensitivity analysis presented here emphasises the possibility to optimise the cardiac activation protocols by use of the present method. It is worth mentioning that these results are highly dependent on boundary conditions. Fluid action inside the cavity has been replaced by a constant pressure in the endocardium during the ejection, and no isovolumetric pressure has

been imposed in relaxation. Probably, the absence of fluid motion inside the cardiac muscle is one of the main causes for the lack of realistic movement. In addition, the geometry has been fixed by the apex in z direction. Thus, the influence of these initial conditions is considerably important in the resultant motion. In a future work, the blood dynamics will be taken into account. The ideal simulation scenario would be recreating with the highest possible detail the heart, in line with the dramatic improvement of data acquisition techniques. To be comprehensive enough, it should include electrical activation, mechanical deformation, blood flow, perfusion, systemic contributions, cell models, etc., in a well defined geometry with the best anatomical information available.

Chapter 7

Conclusions and future work

Cardiac computational models are a relevant tool that can give biomedical researchers additional source of information to understand how the heart works. In this thesis HPC techniques have been applied to build the CCM tool, which is capable of running in parallel in thousands of processors, allowing high fidelity simulations in fine meshes. A key issue is the almost ideal scalability, not only for large and complex problems but also for medium-size meshes. The model is very appealing for direct validation against experimental measurements on real cases obtained from medical images, such as ejection rate, torsion, wall thickening, deformation or time sequence. Coupled with advanced image processing and analysis techniques, it could constitute a framework that could help to understand the function of the myocardium. Additionally, it could help surgery planning and cardiac modeling of pathological situations.

7.1 Contributions

The framework presented in this thesis simulates a pumping heart, providing complementary knowledge of the EM propagation in 3D ventricular geometries. The CCM tool has been built following four steps:

1. HPC Electrophysiological model. FHN and FK formulations have been implemented to be solved efficiently in large-scale parallel facilities. The electrophysiological equations have been used to perform the following studies:

- Numerical treatment of the ODE-like terms in the model. Important differences in the diffusion have been shown using open and closed integration rules in

the solution of the governing equations. By proposing the use of a close nodal integration rule for the mass matrix, a consistent local-spatial scheme has been obtained. We have shown that if the ODE-like local terms are 'spacialized', the solution present spurious numerical effects that can lead to plainly wrong results (notably, the case with zero diffusion).

- Sensitivity to the fiber field errors. Background noise affects the determination of the fiber tract direction calculated from the DT-MRI. We have run some tests adding noise to the fiber field and shown how this noise influences the final results. Controlled perturbations have been applied to a synthetic fiber field, concluding that less than 10% of random noise does not affect the electrophysiological simulations.

- Analysis of the relation between conductivity and conduction velocity. The computational framework has shown that the relation between them is not linear. We have seen that if the conduction velocity is three times faster in the long axis than in the perpendicular direction of myocardial fibers, the velocity does not behave in the same manner. To maintain the same proportionality, the crosswise diffusion and the axial diffusion have to be determined experimentally. In addition, we have proposed a method to determine conductivity values in any computational code.

- Mesh convergence of the CCM tool. Electrophysiological simulations have been performed to determine the conduction velocities at coarse and fine spatial resolution meshes. Results have been substantially close, demonstrating that velocities become stable in the spatial range we are working.

2. HPC Mechanical model. Non-linear solid mechanics of complex materials is computationally expensive, with a large amount of inner nodal or Gauss point loops, requiring HPC techniques in the solution. In this work, a large strain total Lagrangian formulation has been implemented. The material model computed has been an Ogden type specially designed for the heart, including modifications published by Holzapfel and Ogden (2009). Compressibility has been taken into account, and a transversally isometric version has been created with a new set of parameters. Although the critical lack of clinical data in compression to validate the constitutive models, the uni-dimensional traction/compression numerical test performed has underlined the fact the constitutive models not always behave symmetrically if used in tension or compression.

3. Fully coupled EM model. Both, electrical and mechanical models have been integrated in Alya. Commonly, to perform EM simulations of the heart, electrical and mechanical governing equations are solved in different meshes. The resolution of the electrical governing equations usually needs a fine mesh to properly capture the action potential wave front and the mechanical system may permit a lower level of discretization. In this work, the electrical and mechanical meshes operate together in a way that the information can be passed easily between the two systems in the coupling process. The electrical and mechanical models have been solved in the same code using the same computational mesh, avoiding computational errors and instabilities in the coupling process, and keeping intact the good scalability properties. Due to the small physical time scales and the high non-linearities of both problems, the explicit formulation has been used for solving highly transient problems, with very short time-scales.

As an application problem, the tool has demonstrated to be useful in measuring sensitivities of the cardiac tissue. Focusing on large scale computational resources with parallel efficiency, it has been applied to investigate the influence of certain inputs in the resultant simulation and to test properties of the heart. For the coupled EM case, the following results have been shown:

- Evidence of the complex design of the tissue structure. To reflect the change of volume inside the cavity reported in the literature, the active force has been adjusted. The study has led to demonstrate the stability an efficiency of the cardiac system, that compensates a wrong functioning of the tissue because of the microstructure disposition, saving the global behavior. Decreasing the active force 30% we have seen that the EF value only have decreased 8%. Due to the helical structure of the cardiac fibers, important variations in the properties of the material can be compensated by the system, allowing the heart to behave normally.

- Sensitivity to the electrical activation. The CCM tool has demonstrated to be capable of capturing variations to small input parameter changes. The time evolution of the action potential has been triggered by initial localized impulses in some predefined locations (synthetically created Purkinje systems). It has been demonstrated that variations in the electrical activation must be very large to really account for changes in the ventricles contractile action.

- Sensitivity to different fiber field orientations. Simulations in a biventricular geometry have been performed using two rule-based models. The propagation

dynamics has been studied throughout the volume of the ventricles, giving measures like ejection fraction. The fiber model has shown an important influence in contraction, greater than the initial activation through the Purkinje system. Linear and cubic rule-based models have predicted different displacement, specially in areas such as the base or the apex. As state in Gil et al. (2013), the description of the fiber field is relevant to get realistic simulations of cardiac mechanics.

- Parallel efficiency. The EM problem has run in NCSA Blue Waters supercomputer, showing that high parallel efficient codes like Alya will allow solving complex engineers and scientists problems in exascale supercomputers. In Marenostrum, we have established the wall clock time of coupled EM problems. With 10000-5000 elements per core, a coupled problem for 1 second of real time has run in approximately 10-15 minutes wall clock time, compiling the code with the Intel Fortran Compiler.

4. Data assimilation. Studies have been performed to find parameters of the constitutive equations. Two different methods have been presented to calibrate electrical and mechanical properties in the cardiac model. We have solved Kalman filters for the assimilation of the electrophysiological parameters and a 'brute force' inverse problem for the mechanics.

7.2   Future lines

Computer models provide an efficient way of research, prior to clinical trials which are expensive and can be a risk to the patients. Simulations can be performed on a patient's data and the results can be delivered to the doctor in an ad-hoc visualization manner (virtual lab). The results can help researchers and cardiologists to get a deeper insight of the problem.

This thesis has shown the potential of the HPC cardiac simulation. In particular, its ability to measure the sensitivity of outputs to different inputs. To achieve the cardiac virtual lab, the complete model should include electrical activation, mechanical deformation, blood flow, perfusion, systemic contributions, cell models, etc., in a well defined geometry with the best anatomical information available. The main future lines of research are the following:

- New physical models will be implemented and integrated in the framework. Particularly, blood inside the cavities. Currently, no wall force is imposed in the endocardium, neither pressure nor viscous strains. The mechanical influence of the blood will be taken into account. We believe that the absence of fluid motion inside the cardiac muscle is one of the main causes for the lack of realistic movement in the CCM.

- Systemic contributions will be included in the model, specially those required when blood flow is solved. Alya is being coupled to 1D models of both the arterial and venous circulatory systems.

- Data assimilation and parameter fitting in 3D will be included.

- New electrophysiological models will be programmed and tested to study the effect of drugs in the action potential behavior and the contraction of the muscle.

- The processes of obtaining high-resolution images will potentially lead to a revolutionary paradigm. As medical imaging progresses, the highest simulation fidelity will be required. The simulation code should recreate with the highest detail the heart. To better face future research lines, Alya performance will be improved through code cleaning and optimization.

This thesis represents a step towards the virtual lab. The combined flexibility and parallel performance of Alya will give to the proposed approach a great advantage when extending the model towards data assimilation, multi-scales and multi-physics. Electrophysiology, mechanical deformation and fluid flow will be coupled, retaining the parallel efficiency.

Bibliography

Ambrosi, D., G. Arioli, F. Nobile, and A. Quarteroni (2011). Electromechanical coupling in cardiac dynamics: The active strain approach. *SIAM Journal on Applied Mathematics 71*(2), 605–621.

Armour, J. A. and W. C. Randall (1970). Structural basis for cardiac function. *American Journal of Physiology 218*, 1517–1523.

Ballester-Rodes, M., A. Flotats, F. Torrent-Guasp, I. Carrio-Gasset, M. Ballester-Alomar, F. Carreras, A. Ferreira, and J. Narula (2006). The sequence of regional ventricular motion. *Eur J Cardiothorac Surg 29*, S139–144.

Basser, P. J., J. Mattiello, and D. LeBihan (1994). Estimation of the effective self-diffusion tensor from the NMR spin echo. *J Magn Reson B 103*, 247–254.

Bayer, J. D., R. C. Blake, G. Plank, and N. A. Trayanova (2012). A novel rule-based algorithm for assigning myocardial fiber orientation to computational heart models. *Annals of Biomedical Engineering 40*, 2243–2254.

Beeler, G. W. and H. Reuter (1977). Reconstruction of the action potential of ventricular myocardial fibres. *J. Physiol. (Lond.) 268*, 177–210.

Belytschko, T., W. Liu, B. Moran, and K. Elkhodary (2000). Nonlinear finite elements for continua and structures. John Wiley and Sons.

Bishop, M., P. Hales, G. Plank, D. Gavaghank, J. Scheider, and V. Grau (2009). Comparison of rule-based and dtmri-derived fibre architecture in a whole rat ventricular computational model. In *Functional Imaging and Modeling of the Heart*, pp. 87–96.

Bishop, M., G. Plank, R. A. Burton, J. E. Schneider, D. J. Gavaghan, V. Grau, and P. Kohl (2010). Development of an anatomically detailed mri-derived rabbit ventricular model and assessment of its impact on simulations of electrophysiological

function. *American Journal of Physiology - Heart and Circulatory Physiology*, 699–718.

Campbell, S. G., E. Howard, J. Aguado-Sierra, B. A. Coppola, J. H. Omens, L. J. Mulligan, A. D. McCulloch, and R. C. Kerckhoffs (2009). Effect of transmurally heterogeneous myocyte excitation-contraction coupling on canine left ventricular Electromechanics. *Exp. Physiol. 94*, 541–552.

Carapella, V., R. Bordas, P. Pathmanathan, M. Lohezic, J. Schneider, P. Kohl, K. Burrage, and V. Grau (2014). Quantitative study of the effect of tissue microstructure on contraction in a computational model of rat left ventricle. *PLoS ONE*.

Carreras, F., M. Ballester, S. Pujadas, R. Leta, and G. Pons-Llado (2006). Morphological and functional evidences of the helical heart from non-invasive cardiac imaging. *Eur J Cardiothorac Surg 29 Suppl 1*, S50–55.

Caruel, M., R. Chabiniok, P. Moireau, Y. Lecarpentier, and D. Chapelle (2014). Dimensional reductions of a cardiac model for effective validation and calibration. *Biomech Model Mechanobiol 13*(4), 897–914.

Chabiniok, R., P. Moireau, P. Lesault, A. Rahmouni, J. Deux, and D. Chapelle (2012). Estimation of tissue contractility from cardiac cine-mri using a biomechanical heart model. *Biomechanics and Modeling in Mechanobiology 11*(5), 609–630.

Chapelle, D., P. Le Tallec, P. Moireau, and M. Sorine (2012). An energy-preserving muscle tissue model: formulation and compatible discretizations. *International Journal for Multiscale Computational Engineering 10*(2), 189–211.

Cherubini, C., S. Filippi, P. Nardinocchi, and L. Teresi (2008). An electromechanical model of cardiac tissue: constitutive issues and electrophysiological effects. *Progress in biophysics and molecular biology 97*, 562–573.

Clerc, L. (1976). Directional differences of impulse spread in trabecular muscle from mammalian heart. *J. Physiol. (Lond.) 255*, 335–346.

Coghlan, H. C., A. R. Coghlan, G. D. Buckberg, and J. L. Cox (2006). 'The electrical spiral of the heart: its role in the helical continuum. The hypothesis of the anisotropic conducting matrix. *Eur J Cardiothorac Surg 29 Suppl 1*, S178–187.

Constantino, J., J. Hu, and N. Trayanova (2012). A computational approach to understanding the cardiac electromechanical activation sequence in the normal and failing heart, with translation to the clinical practice of crt. *Progress in Biophysics and Molecular Biology 110*, 372–379.

Costa, K. D., J. W. Holmes, and A. D. Mcculloch (2001). Modelling cardiac mechanical properties in three dimensions. *Philosophical Transactions of the Royal Society of London. Series A:Mathematical, Physical and Engineering Sciences 359*, 1233–1250.

Costa, K. D., P. J. Hunter, J. S. Wayne, L. K. Waldman, J. M. Guccione, and A. D. McCulloch (1996). A three-dimensional finite element method for large elastic deformations of ventricular myocardium. *Journal of Biomechanics Engineering 118*, 464–472.

Demiray, H. (1976). Stresses in ventricular wall. *Journal of Applied Mechanics 43*, 194–197.

DiFrancesco, D. and D. Noble (1985). A model of cardiac electrical activity incorporating ionic pumps and concentration changes. *Philos. Trans. R. Soc. Lond., B, Biol. Sci. 307*, 353–398.

Dokos, S., B. Smaill, A. Young, and I. LeGrice (2002). Shear properties of passive ventricular myocardium. *American Journal of Physiology - Heart and Circulatory Physiology 283*, H2650–2659.

Donea, J., A. Huerta, J. Ponthot, and A. Rodríguez-Ferran (2004). *Arbitrary Lagrangian-Eulerian Methods*.

Dorri, F., P. F. Niederer, and P. P. Lunkenheimer (2006). A finite element model of the human left ventricular systole. *Comput Methods Biomech Biomed Engin 9*, 319–341.

Durrer, D., R. T. van Dam, G. E. Freud, M. J. Janse, F. L. Meijler, and R. C. Arzbaecher (1970). Total excitation of the isolated human heart. *Circulation 41*, 899–912.

Eriksson, K., E. Estep, P. Hansbo, and C. Johnson (1996). Computational differential equations.

Fenton, F., E. Cherry, A. Karma, and W. Rappel (2005). Modeling wave propagation in realistic heart geometries using the phase-field method. *Chaos 15*, 13502.

Fenton, F. and A. Karma (1998). Vortex dynamics in three-dimensional continuous myocardium with fiber rotation: Filament instability and fibrillation. *Chaos 8*, 20–47.

FitzHugh, R. (1961). Impulses and Physiological States in Theoretical Models of Nerve Membrane. *Biophys. J. 1*, 445–466.

Fung, Y. C. (1993). Mechanical Properties of Living Tissues. *Springer*.

Gamper, U., P. Boesiger, and S. Kozerke (2007). Diffusion imaging of the in vivo heart using spin echoes–considerations on bulk motion sensitivity. *Magn Reson Med 57*, 331–337.

Gil, D., A. Borràs, R. Arís, M. Vázquez, P. Lafortune, G. Houzeaux, J. Aguado, M. Ballester, C. Li, and F. Carreras (2013). What a difference in biomechanics cardiac fiber makes. *7746*, 253–260.

Goktepe, S. and E. Kuhl (2010). Electromechanics of the heart: a unified approach to the strongly coupled excitation-contraction problem. *Computational Mechanics 45*, 227–243.

Greenbaum, R. A., S. Y. Ho, D. G. Gibson, A. E. Becker, and R. H. Anderson (1981). Left ventricular fibre architecture in man. *Br Heart J 45*, 331–337.

Guccione, J. M., A. D. McCulloch, and L. K. Waldman (1991). Passive material properties of intact ventricular myocardium determined from a cylindrical model. *Journal of Biomechanics Engineering 113*, 42–55.

Harmer, J., K. Pushparajah, N. Toussaint, C. Stoeck, R. Chan, D. Atkinson, R. Razavi, and S. Kozerke (2013). In vivo myofibre architecture in the systemic right ventricle. *European Heart Journal*.

Helm, P., M. F. Beg, M. I. Miller, and R. L. Winslow (2005). Measuring and mapping cardiac fiber and laminar architecture using diffusion tensor MR imaging. *Ann. N. Y. Acad. Sci. 1047*, 296–307.

Hodgkin, A. L. and A. F. Huxley (1952). A quantitative description of membrane current and its application to conduction and excitation in nerve. *J. Physiol. (Lond.) 117*, 500–544.

Holzapfel, G. (2000). *Nonlinear Solid Mechanics: A Continuum Approach for Engineering*. John Wiley and Sons.

Holzapfel, G. A. (2004). *Computational Biomechanics of Soft Biological Tissue.* John Wiley and Sons.

Holzapfel, G. A. and R. W. Ogden (2009). Constitutive modelling of passive myocardium: a structurally based framework for material characterization. *Philosophical Transactions of the Royal Society A: Mathematical, Physical and Engineering Sciences 367.*

Houzeaux, G., R. de la Cruz, H. Owen, and M. Vázquez (2013). Parallel uniform mesh multiplication applied to a navier-stokes solver. *Computers and Fluids 80*, 142–151.

Houzeaux, G., M. Vázquez, R. Aubry, and J. Cela (2009). A massively parallel fractional step solver for incompressible flows. *JCP 228*(17), 6316–6332.

Houzeaux, G., M. Vázquez, R. Aubry, and J. Cela. (2009). A massively parallel fractional step solverfor incompressible flows. *Journal of Computational Physics 228.*

Houzeaux, G., M. Vázquez, X. Sáez, and J. Cela (2011). Hybrid mpi-openmp performance in massively parallel computational fluid dynamics. *Parallel Computational Fluid Dynamics 74.*

Humphrey, J. (2001). Cardiovascular solid mechanics. cells, tissues, and organs. *Springer.*

Humphrey, J., R. Strumpf, and F. Yin (1990). Determination of a constitutive relation for passive myocardium. *Journal of Biomechanics Engineering 112*, 333–346.

Hunter, P., M. Nash, and G. Sands (1997). Computational electromechanics of the heart. *Computational biology of the heart*, 345–407.

Hunter, P. and B. Smaill (1988). The analysis of cardiac function: a continuum approach. *Prog. Biophys. Mol. Biol. 52*(2), 101–164.

Hunter, P. J., A. D. McCulloch, and H. E. ter Keurs (1998). Modelling the mechanical properties of cardiac muscle. *Prog. Biophys. Mol. Biol. 69*, 289–331.

Hunter, S. C. (1983). *Mechanics of Continuous Media.*

Johnson, C. (1987). *Numerical solutions of partial differential equations by the Finite Element Method.*

Jung, B., K. E. Odening, E. Dall'Armellina, D. Foll, M. Menza, M. Markl, and J. E. Schneider (2012). A quantitative comparison of regional myocardial motion in mice, rabbits and humans using in-vivo phase contrast CMR. *J Cardiovasc Magn Reson 14*, 87.

Kalman, R. E. (1960). A new approach to linear filtering and prediction problems. *Transactions of the ASME Journal of Basic Engineering* (82 (Series D)), 35–45.

Keldermann, R., M. Nash, H. Gelderblom, V. Wang, and A. Panfilov (2010). Electromechanical wavebreak in a model of the human left ventricle. *American Journal of Physiology - Heart and Circulatory Physiology 299*, 134–143.

Kerckhoffs, R., S. Healy, T. Usyk, and D. McCulloch (2006). Computational methods for cardiac electromechanics. *Med Image Anal 94*, 769–783.

Kerckhoffs, R., D. McCulloch, J. Omens, and J. Mulligan (2009). Effects of biventricular pacing and scar size in a computational model of the failing heart with left bundle branch block. *Med Image Anal 13*, 362–369.

Kerckhoffs, R., J. Omens, and A. McCulloch (2012). A single strain-based growth law predicts concentric and eccentric cardiac growth during pressure and volume overload. *Mechanics Research Communications 42*, 40–50.

Krishnamurthy, A., C. Villongco, J. Chuang, R. Frank, V. Nigam, E. Belezzuoli, P. Stark, E. Krummen, S. Narayan, J. Omens, D. McCulloch, and R. Kerckhoffs (2013). Patient-Specific Models of Cardiac Biomechanics. *Journal of Computational Physics 244*, 4–21.

Lafortune, P., R. Arís, M. Vázquez, and G. Houzeaux (2012). Coupled electromechanical model of the heart: Parallel finite element formulation. *International Journal for Numerical Methods in Biomedical Engineering 28*, 72–86.

Lamata, P., S. Niederer, D. Nordsletten, D. Barber, I. Roy, R. Hose, and N. Smith (2011). An accurate, fast and robust method to generate patient-specific cubic hermite meshes. *Medical Image Analysis 15*, 801–813.

Land, S., S. Niederer, and N. Smith (2012). Efficient computational methods for strongly coupled cardiac electromechanics. *IEEE Trans Biomed Engineering 59*, 1219–1228.

Legrice, I., P. Hunter, A. Young, and B. Smaill (2001). The architecture of the heart: a data-based model. *Philosophical Transactions of the Royal Society of London. Series A: Mathematical, Physical and Engineering Sciences 359*, 1217–1232.

Luo, C. and Y. Rudy (1991). A model of the ventricular cardiac action potential. Depolarization, repolarization, and their interaction. *Circ. Res. 68*, H571–582.

Mao, H., L. Wang, L. Wong, H. Liu, and P. Shi (2012). Towards integrated noninvasive personalization of cardiac electromechanics. In *Biomedical Imaging (ISBI), 2012 9th IEEE International Symposium on*, pp. 1430–1433.

Marin, G., F. Cucchietti, M. Vázquez, C. Tripiana, G. Houzeaux, R. Arís, P. Lafortune, and J. Aguado-Sierra (2013). Alya red: A computational heart. *Science, Special Feature: International Science and Engineering Visualization Challenge 339*, 518–519.

Marras, S., M. Moragues, M. Vázquez, O. Jorba, and G. Houzeaux (2013). Simulations of moist convection by a variational multiscale stabilized finite element method. *Journal of Computational Physics 252*, 195–218.

McCormick, M., D. Nordsletten, D. Kay, and N. Smith (2013). Simulating left ventricular fluid-solid mechanics through the cardiac cycle under {Lvad} support. *Journal of Computational Physics 244*, 80–96.

McCulloch, A. and G. Huber (2002). Integrative biological modelling in silico. *Novartis Foundation Symposium 247*, 4–19.

Mirsky, I. (1973). Ventricular and arterial wall stresses based on large deformation analyses. *Biophys. J. 13*, 1141–1159.

Murillo, M. and X. Cai (2004). A fully implicit parallel algorithm for simulating the non-linear electrical activity of the heart. *Numerical Linear Algebra with Applications 11*, 261–277.

Nagler, A., C. Bertoglio, M. Gee, and W. Wall (2013). Personalization of cardiac fiber orientations from image data using the unscented kalman filter. In *Functional Imaging and Modeling of the Heart*, Volume 7945, pp. 132–140.

Nickerson, D., S. Niederer, C. Stevens, M. Nash, and P. Hunter (2006). A computational model of cardiac electromechanics. *Conf Proc IEEE Engineering Med Biol Soc 1*, 5311–5314.

Niederer, S., E. Kerfoot, A. Benson, M. Bernabeu, O. Bernus, C. Bradley, E. Cherry, R. Clayton, F. Fenton, A. Garny, E. Heidenreich, S. Land, M. Maleckar, P. Pathmanathan, G. Plank, J. Rodríguez, I. Roy, F. Sachse, G. Seemann, O. Skavhaug, and N. Smith (2011). Verification of cardiac tissue electrophysiology simulators using an n-version benchmark. *Philosophical Transactions of the Royal Society A: Mathematical, Physical and Engineering Sciences 369*, 4331–4351.

Niederer, S., P. Lamata, G. Plank, P. Chinchapatnam, and M. Ginks (2012). Analyses of the redistribution of work following cardiac resynchronisation therapy in a patient specific model. *PLoS ONE*.

Niederer, S. and N. Smith (2008). An improved numerical method for strong coupling of excitation and contraction models in the heart. *Prog. Biophys. Mol. Biol. 96*, 90–111.

Nielsen, P. M., I. J. Le Grice, B. H. Smaill, and P. J. Hunter (1991). Mathematical model of geometry and fibrous structure of the heart. *American Journal of Physiology 260*, H1365–1378.

Noble, D. (2007). From the Hodgkin-Huxley axon to the virtual heart. *J. Physiol. (Lond.) 580*, 15–22.

Noble. D, R. Y. (2001). Models of cardiac ventricular action potentials: iterative interaction between experiment and simulation. *359*, 1127–1142.

Nordsletten, D., D. Kay, and N. Smith (2010). A non-conforming monolithic finite element method for problems of coupled mechanics. *Journal of Computational Physics 229*, 7571–7593.

Nordsletten, D., M. McCormick, P. J. Kilner, P. Hunter, D. Kay, and N. Smith (2011). Fluid-solid coupling for the investigation of diastolic and systolic human left ventricular function. *International Journal for Numerical Methods in Biomedical Engineering 27*, 1017–1039.

Novak, V., F. Yin, and J. Humphrey (1994). Regional mechanical properties of passive myocardium. *Journal of Biomechanics 27*, 403–412.

Novartis. http://www.novartis.com/innovation/getting-drugs-to-patient/index.shtml.

Penland, R., D. Harrild, and C. Henriquez (2002). Modeling impulse propagation and extracellular potential distributions in anisotropic cardiac tissue using a finite volume element discretization. *Computing and Visualization in Science 4*, 215–226.

Peyrat, J. M., M. Sermesant, X. Pennec, H. Delingette, C. Xu, E. McVeigh, and N. Ayache (2006). Towards a statistical atlas of cardiac fiber structure. *Med Image Comput Comput Assist Interv 9*, 297–304.

Potse, M., B. Dube, J. Richer, A. Vinet, and R. Gulrajani (2006). A comparison of monodomain and bidomain reaction-diffusion models for action potential propagation in the human heart. *IEEE Trans Biomed Engineering 53*, 2425–2435.

Poveda, F., E. Marti, D. Gil, F. Carreras, and M. Ballester (2012). Helical structure of ventricular anatomy by diffusion tensor cardiac MR tractography. *JACC Cardiovasc Imaging 5*(7), 754–755.

Puzyrev, V., J. Koldan, J. de la Puente, G. Houzeaux, M. Vázquez, and J. M. Cela (2013). A parallel finite-element method for three-dimensional controlled-source electromagnetic forward modelling. *Geophysical Journal International 193*, 678–693.

Rice, J. and P. de Tombe (2004). Approaches to modeling crossbridges and calcium-dependent activation in cardiac muscle. *Prog. Biophys. Mol. Biol. 85*, 179–195.

Roberts, D., L. Hersh, and A. Scher (1979). Influence of cardiac fiber orientation on wavefront voltage, conduction velocity, and tissue resistivity in the dog. *Circ. Res. 44*, 701–712.

Rossi, S., R. Ruiz-Baier, L. Pavarino, and A. Quarteroni (2012). Orthotropic active strain models for the numerical simulation of cardiac biomechanics. *International Journal for Numerical Methods in Biomedical Engineering 28*(6-7), 761–788.

Roth, B. (1997). Electrical conductivity values used with the bidomain model of cardiac tissue. *IEEE Trans Biomed Engineering 44*, 326–328.

Rubart, M. and D. Zipes (2001). Genesis of cardiac arrhythmias: electrophysiologic considerations. In *Braunwald's Heart Disease. A Textbook of Cardiovascular Medicine*, Volume 1.

Sainte-Marie, J., D. Chapelle, R. Cimrman, and M. Sorine (2006). Modeling and estimation of the cardiac electromechanical activity. *Computers and Structures 84*(28), 1743 – 1759.

Scollan, D., A. Holmes, R. Winslow, and J. Forder (1998). Histological validation of myocardial microstructure obtained from diffusion tensor magnetic resonance imaging. *American Journal of Physiology 275*, H2308–2318.

Sebastian, R., V. Zimmerman, D. Romero, D. Sanchez-Quintana, and A. F. Frangi (2013). Characterization and modeling of the peripheral cardiac conduction system. *IEEE Trans Med Imaging 32*, 45–55.

Seemann, G., F. Sachse, D. Weiss, and O. Dossel (2003). Quantitative reconstruction of cardiac electromechanics in human myocardium: regional heterogeneity. *J. Cardiovasc. Electrophysiol. 14*, S219–228.

Sermesant, M., R. Chabiniok, P. Chinchapatnam, T. Mansi, F. Billet, P. Moireau, J. Peyrat, K. Wong, J. Relan, K. Rhode, M. Ginks, P. Lambiase, H. Delingette, M. Sorine, C. Rinaldi, D. Chapelle, R. Razavi, and N. Ayache (2012). Patient-specific electromechanical models of the heart for the prediction of pacing acute effects in crt: A preliminary clinical validation. *Medical Image Analysis 16*, 201–215.

Sermesant, M., P. Moireau, O. Camara, J. Sainte-Marie, R. Andriantsimiavona, R. Cimrman, D. L. Hill, D. Chapelle, and R. Razavi (2006). Cardiac function estimation from MRI using a heart model and data assimilation: advances and difficulties. Volume 10, pp. 642–656.

Simelius, K., J. Nenonen, and M. Horacek (2001). Simulation of anisotropic propagation in the myocardium with a hybrid bidomain model. In *Functional Imaging and Modeling of the Heart*, Volume 2230 of *Lecture Notes in Computer Science*, pp. 140–147.

Smith, N., A. de Vecchi, M. McCormick, D. Nordsletten, O. Camara, A. Frangi, H. Delingette, M. Sermesant, J. Relan, N. Ayache, M. Krueger, W. Schulze, R. Hose, I. Valverde, P. Beerbaum, C. Staicu, M. Siebes, J. Spaan, P. Hunter, J. Weese, H. Lehmann, D. Chapelle, and R. Rezavi (2011). euheart: personalized and integrated cardiac care using patient-specific cardiovascular modelling. *Interface Focus 1*, 349–364.

Staab, A., E. Rook, M. Maliepaard, L. Aarons, and C. Benson (2013). Modeling and simulation in clinical pharmacology and dose finding. *CPT Pharmacometrics Syst Pharmacol 2*, e29.

Stinstra, J., B. Hopenfeld, and R. Macleod (2005). On the passive cardiac conductivity. *Annals of Biomedical Engineering 33*, 1743–1751.

Streeter, D., H. Spotnitz, D. Patel, J. Ross, and E. Sonnenblick (1969). Fiber orientation in the canine left ventricle during diastole and systole. *Circulation Research 24*, 339–347.

Sugiura, S., T. Washio, A. Hatano, J. Okada, H. Watanabe, and T. Hisada (2012). Multi-scale simulations of cardiac electrophysiology and mechanics using the University of Tokyo heart simulator. *Prog. Biophys. Mol. Biol. 110*, 380–389.

Sundnes, J., F. Nielsen, K. Mardal, X. Cai, G. Lines, and A. Tveito (2006). On the computational complexity of the bidomain and the monodomain models of electrophysiology. *Annals of Biomedical Engineering 34*, 1088–1097.

Sundnes, J., S. Wall, H. Osnes, T. Thorvaldsen, and A. D. McCulloch (2014). Improved discretisation and linearisation of active tension in strongly coupled cardiac electromechanics simulations. *Comput Methods Biomech Biomed Engin 17*, 604–615.

Ten-Tusscher, K. and A. Panfilov (2006). Cell model for efficient simulation of wave propagation in human ventricular tissue under normal and pathological conditions. *Physics in Medicine and Biology 51*, 6141–6156.

Torrent-Guasp, F., M. Kocica, A. Corno, M. Komeda, F. Carreras-Costa, and H. W. A. Flotats, J. Cosin-Aguillar (2005). Towards new understanding of the heart structure and function. *European Journal of Cardio-Thoracic Surgery*, 191–201.

Toussaint, N., M. Sermesant, C. Stoeck, S. Kozerke, and P. Batchelor (2010). In vivo human 3d cardiac fibre architecture: Reconstruction using curvilinear interpolation of diffusion tensor images. In *Medical Image Computing and Computer-Assisted Intervention, MICCAI 2010*, Volume 13, pp. 418–425.

Toussaint, N., C. Stoeck, T. Schaeffter, S. Kozerke, M. Sermesant, and P. Batchelor (2013). In vivo human cardiac fibre architecture estimation using shape-based diffusion tensor processing. *Medical Image Analysis 17*, 1243–1255.

Trayanova, N. (2011). Whole-heart modeling: applications to cardiac electrophysiology and electromechanics. *Circ. Res. 108*, 43.

Trayanova, N., G. Plank, and B. Rodriguez (2006). What have we learned from mathematical models of defibrillation and postshock arrhythmogenesis? Application of bidomain simulations. *Heart Rhythm 3*, 1232–1235.

Trayanova, N. and J. Rice (2011). Cardiac electromechanical models: From cell to organ. *Frontiers in Physiology 2*, 43.

Usyk, P. and D. McCulloch (2003). Relationship between regional shortening and asynchronous electrical activation in a three-dimensional model of ventricular electromechanics. *J. Cardiovasc. Electrophysiol. 14*, S196–202.

Vázquez, M., R. Arís, G. Houzeaux, R. Aubry, P. Villar, J. Garcia-Barnós, D. Gil, and F. Carreras (2011). A massively parallel computational electrophysiology model of the heart. *International Journal for Numerical Methods in Biomedical Engineering 27*, 1911–1929.

Vigmond, J., M. Hughes, G. Plank, and J. Leon (2003). Computational tools for modeling electrical activity in cardiac tissue. *J Electrocardiol 36 Suppl*, 69–74.

Wang, V., C. Hoogendoorn, A. Frangi, B. Cowan, P. Hunter, A. Young, and M. Nash (2013). Automated personalised human left ventricular fe models to investigate heart failure mechanics. In *Statistical Atlases and Computational Models of the Heart. Imaging and Modelling Challenges*, Volume 7746, pp. 307–316.

Watanabe, H., S. Sugiura, H. Kafuku, and T. Hisada (2004). Multiphysics simulation of left ventricular filling dynamics using fluid-structure interaction finite element method. *Biophys. J. 87*, 2074–2085.

Wong, L., L. Wang, H. Zhang, H. Liu, and P. Shi (2008). Simulation of active cardiac electromechanical dynamics. In *Medical Imaging and Augmented Reality*, Volume 5128, pp. 60–69. Springer Berlin Heidelberg.

Xi, J., P. Lamata, J. Lee, P. Moireau, D. Chapelle, and N. Smith (2011). Myocardial transversely isotropic material parameter estimation from in-silico measurements based on a reduced-order unscented kalman filter. *Journal of the Mechanical Behavior of Biomedical Materials 4*(7), 1090–1102.

Xi, J., P. Lamata, S. Niederer, S. Land, W. Shi, X. Zhuang, S. Ourselin, S. Duckett, A. Shetty, C. Rinald, D. Rueckert, R. Razavi, and N. Smith (2012). The estimation of patient-specific cardiac diastolic functions from clinical measurements. *Medical Image Analysis 17*, 133–146.

Xia, L., M. Huo, Q. Wei, F. Liu, and S. Crozier (2006). Electrodynamic heart model construction and ECG simulation. *Methods Inf Med 45*(5), 564–573.

Yin, F., C. Chan, and R. Judd (1996). Compressibility of perfused passive myocardium. *American Journal of Physiology - Heart and Circulatory Physiology 271*, H1864–1870.

Yin, F., R. Strumpf, P. Chew, and S. Zeger (1987). Quantification of the mechanical properties of noncontracting canine myocardium under simultaneous biaxial loading. *Journal of Biomechanics 20*, 577–589.

Zou, C., Z. Liu, F. Qu, B. Jiang, J. Song, J. Hui, X. Cheng, and W. Han, L. Jiang
(2009). Valsartan prevents the development of rabbit's heart failure by restoring
calcium uptake of sarcoplasmic reticulum. *Journal of Geriatric Cardiology 6*, 173–
177.

Publications related to the thesis

International Journals

- R. Arís, J. Aguado-Sierra, G. Houzeaux, D. Gil, Agnés Borràs, R. Sebastian and M. Vázquez. *(Submitted).* Sensitivity Analysis to Initial Stimuli and Fiber Orientation of a Biventricular Electromechanical Computational Model of the Heart. *International Journal for Numerical Methods in Biomedical Engineering.*

- M. Vázquez, R. Arís, J. Aguado-Sierra, G. Houzeaux, A. Santiago, M. López, P. Córdoba, M. Rivero and J.C. Cajas. *(In press).* Alya Red CCM: HPC-based Cardiac Computational Modeling. *Selected Topics of Computational and Experimental Fluid Mechanics.*

- G. Marin, F. Cucchietti, M. Vázquez; C. Tripiana, G. Houzeaux, R. Arís, P. Lafortune and J. Aguado-Sierra (2013). Alya Red: A Computational Heart. *Science, Special Feature: International Science and Engineering Visualization Challenge 339, 518-519.*

- P. Lafortune, R. Arís, M. Vázquez and G. Houzeaux (2012). Coupled electromechanical model of the heart: Parallel finite element formulation. *International Journal for Numerical Methods in Biomedical Engineering 28, 72-86.*

- M. Vázquez, R. Arís, G. Houzeaux, R. Aubry, P. Villar J. Garcia-Barnés, D. Gil and F. Carreras (2011). A massively parallel computational electrophysiology model of the heart. *International Journal for Numerical Methods in Biomedical Engineering 27, 1911-1929.*

Congress Contributions

- M. Vázquez, G. Houzeaux, S. Koric, A. Artigues, J. Aguado-Sierra, R. Aris, D. Mira, H. Calmet, F. Cucchietti, H. Owen, A. Taha, J. M. Cela (2014). Alya: Towards Exascale for Engineering Simulation Codes. *International Supercomputing Conference.*

- M. Vázquez, G. Houzeaux, R. Arís, J. Aguado-Sierra and P. Lafortune (2013). Parallel coupled fluid-electro-mechanical cardiac model. *Computational Methods for Coupled Problems in Science and Engineering V*, Ibiza.

- R. Arís, P. Lafortune, J. Aguado-Sierra and M. Vázquez (2012). Sensitivity analysis of DTI and Streeter-based fibre models on electro-mechanics using a bi-ventricular heart geometry. *Bioengineering 2012*, Oxford.

- F. Rubio, M. Hanzich, R. Arís, M. Vázquez and G. Houzeaux (2011). Parallel Computational Electrophysiology in NVIDIA GPUs. *Conference on Computational and Mathematical Biomedical Engineering*, Washington.

- P. Lafortune, R. Arís, M. Vázquez, G. Houzeaux and A. Jérusalem (2011). Large Scale Electromechanical Cardiac Simulations. *Conference on Computational and Mathematical Biomedical Engineering*, Washington.

- D. Gil, A. Borras, M. Ballester, F. Carreras, R. Arís, M. Vazquez, E. Marti, F. Poveda (2011). MIOCARDIA: Integrating cardiac function and muscular architecture for a better diagnosis. Barcelona. *International Symposium on Applied Sciences in Biomedical and Communication Technologies*

- R.Arís, M. Vázquez, P. Lafortune, P. Villar, G. Houzeaux, D. Gil, J. Garcia-Barnés, M. Ballester, F. Carreras (2010). Massively parallel electromechanical model of the heart. *IV European Conference on Computational Mechanics*, Paris.

- M. Vázquez, R. Arís, G. Houzeaux, P. Villar, P. Lafortune, C. Labarta, D. Gil, J. Garcia-Barnés, M. Ballester, F. Carreras (2010). A massively parallel electro-mechanical model of the heart for large-scale simulations. *Computer Methods in Biomechanics and Biomedical Engineering*, Valencia.

- R. Arís, G.Houzeaux, M. Vázquez, D.Gil, J.Garcia-Barnés (2009). Massively parallel cardiac computational electrophysiology in anisotropic media. *Conference on Computational and Mathematical Biomedical Engineering*, Swansea.

- M. Vázquez, R. Arís, A. Rosolen and G. Houzeaux (2008). A high performance computational electrophysiology model, *8th. World Congress on Computational Mechanics ECCOMAS*, Venice.

- D. Gil, J. Garcia-Barnés, F. Carreras, M. Vázquez, R. Arís and G. Houzeaux (2008). Patient-Sensitive Anatomic and Functional 3D Model of the Left Ventricle. *8th. World Congress on Computational Mechanics ECCOMAS*, Venice.

- D.Gil, J.Garcia-Barnés, F. Carreras, M. Ballester, M.Vázquez, R.Arís, G.Houzeaux (2008). Un model 3D del ventricle esquerre integrant anatomia i funcionalitat. *Congrés Societat Catalana de Cardiologia*, Barcelona.

- M. Vázquez, R. Arís, G. Houzeaux, J. M. Cela, D. Gil, J. Garcia-Barnés and F. Carreras (2008). Anatomical and Functional High Performance Computational Electrophysiology model of the Left Ventricle. *Grand Challenges in Computational Biology*, Barcelona.

Workshop Contributions

- R. Arís, M. Vázquez, J. Aguado-Sierra, M. Rivero and G. Houzeaux (2013). HPC techniques in Cardiac Modeling. *1st International Workshop on Latest Advances in Cardiac Modeling*, Munich.

- R. Arís, J. Aguado-Sierra, G. Houzeaux and M. Vázquez (2012). Alya Red: A computational simulation of the heart coupling electrophysiology and cardiac mechanics. *Workshop on Modeling and Simulation of Physiological Systems*, Lisboa.

Funded Projects

List of Figures

List of Tables